UNIVERSITY OF THESSALY

SCHOOL OF HEALTH SCIENCES

FACULTY OF MEDICINE

LABORATORY OF MEDICAL PHYSICS

Director Professor Kyriaki Theodorou

Doctoral Thesis

«Quantification and Machine Learning classification of imaging biomarkers towards the optimization of MRI differential diagnosis»

by

ALEXANDROS – CHRYSOVALANTIS VAMVAKAS

Medical Physicist

Submitted for the fulfilment

of part of requirements for acquisition of the

Doctoral Degree

Larissa, 2023

this page intentionally left blank

The approval of the Doctoral Thesis by the Faculty of Medicine of the School of Health Sciences of the University of Thessaly does not imply acceptance of the views of the author (in accordance with the provisions of article 202, paragraph 2 of Law 5343/1932).

this page intentionally left blank

Approved by the members of the Seven-member Examining Committee (6th/18-01-2023 General Assembly):

1st Examinator (Supervisor)	**CHRYSOVALANTIS – IOANNIS TSOUGOS** Professor of Medical Physics, Faculty of Medicine, University of Thessaly
2nd Examinator	**CONSTANTINE KAPPAS** Professor Emeritus of Medical Physics, Faculty of Medicine, University of Thessaly
3rd Examinator	**IOANNIS FEZOULIDIS** Professor Emeritus of Diagnostic Radiology, Faculty of Medicine, University of Thessaly
4th Examinator	**KYRIAKI THEODOROU** Professor of Medical Physics and Informatics, Faculty of Medicine, University of Thessaly
5th Examinator	**AIKATERINI VASSIOU** Professor of Anatomy, Faculty of Medicine, University of Thessaly
6th Examinator	**MARIANNA VLYCHOU** Professor of Radiology, Faculty of Medicine, University of Thessaly
7th Examinator	**PANAGIOTIS GEORGOULIAS** Professor of Nuclear Medicine, Faculty of Medicine, University of Thessaly

this page intentionally left blank

Acknowledgements

My doctoral studies were a great opportunity in terms of further deepening into the scientific field of Biomedical Imaging Analytics, while it allowed me to extend my academic qualifications and acquire multifaceted supplies, useful for my overall scientific and personal development. The realization of the present doctoral research was essentially supported by many people in academia and beyond, whose contribution should be acknowledged.

First and foremost, I would like to express my sincere gratitude to my Supervisor Professor of Medical Physics Ioannis Tsougos, for his trust and the undivided moral, scientific and organizational support that he offered me throughout my doctoral research.

I would like to extend my sincerest thanks to the other members of the Three-Member Advisory Committee, Emeritus Professors, Constantine Kappas and Ioannis Fezoulidis, whose academic career was for me a lasting example of scientific excellence and ethics.

In addition, I would like to warmly thank Professors Kyriaki Theodorou, Aikaterini Vassiou, Marianna Vlychou and Eftychia Kapsalaki, as well as the academic and clinical staff of the Medical Physics and the Diagnostic Radiology Laboratories of the Department of Medicine who contributed to the realization of the present doctoral research.

I am deeply thankful to Professors Steven Williams and Matthew Howard, and Associate Professor Mattia Veronese, as well as all members of the Centre for Neuroimaging Sciences at King's College London, who warmly welcomed me, and introduced me in the exciting field of functional neuroimaging, during my traineeship.

I would like to express my sincere gratitude and indebtedness to Professor Christos Davatzikos, as well as all members of the Center for Biomedical Imaging Computing and Analytics of the University of Pennsylvania, who accepted me into their esteemed scientific

community, and gave me the opportunity to participate in cutting-edge medical imaging research.

Special thanks to my colleagues at the Medical Physics lab of University of Thessaly, and especially PhD Candidate Dimitra Tsivaka who has been an excellent collaborator and had an active participation towards the fulfilment of the scopes of my doctorate research.

I would also like to thank the Foundation for Research and Innovation (HFRI) for funding my doctoral research, as well as the European Commission and the Fulbright Foundation, for providing financial support for my visits to foreign collaborating academic institutes in the UK and USA. In this context, I would also like to thank the competent administrative staff of the University of Thessaly who handled all the relevant procedures excellently.

Finally, I am eternally grateful to my family for all kinds of support they offered me during my studies.

Alexandros – Chrysovalantis Vamvakas

Alexandros Chrysovalantis Vamvakas received his B.Sc. in Physics and M.Sc. in Medical Physics from University of Patras. His PhD research was conducted at the Laboratory of Medical Physics of the University of Thessaly and was funded from the Hellenic Foundation for Research and Innovation (HFRI). His research interests mainly focus on the emerging analytics technologies applied in neuroimaging as well as the non-invasive imaging cancer diagnosis and risk stratification. Alexandros has participated in research projects, at the University of Thessaly and the Center for Research and Technology Hellas (CERTH). Also, he gained international research experience, as a Visiting Research Student at the Centre for Neuroimaging Sciences of Institute of Psychiatry, Psychology & Neuroscience of King's College London, UK, under an Erasmus+ Traineeship, as well as at the Center for Biomedical Image Computing and Analytics of University of Pennsylvania, USA, under a Fulbright Foundation Scholarship. The main outcomes of his research studies have been published in international peer-review scientific journals and presented at international conferences. Additionally, he is a member of scientific/ professional societies, while he serves as a reviewer editor for international scientific journals.

this page intentionally left blank

«Quantification and Machine Learning classification of imaging biomarkers towards the optimization of MRI differential diagnosis»

ALEXANDROS – CHRYSOVALANTIS VAMVAKAS

University of Thessaly, Faculty of Medicine, 2023

THREE-MEMBER ADVISORY COMMITTE

1. **Chrysovalantis – Ioannis Tsougos,** Professor of Medical Physics, Faculty of Medicine, University of Thessaly (**Supervisor**)
2. **Constantine Kappas,** Professor Emeritus of Medical Physics, Faculty of Medicine, University of Thessaly
3. **Ioannis Fezoulidis,** Professor Emeritus of Diagnostic Radiology, Faculty of Medicine, University of Thessaly

this page intentionally left blank

Abstract

The role of biomedical imaging has expanded remarkably since the advent of digital technology, demonstrated from a wide range of powerful, versatile, and precise diagnostic imaging protocols that constitute integral part of most clinical procedures. Modern clinical imaging has brought forth new levels of pathophysiology assessment non-invasively, by exploiting various macroscopic quantitative imaging parameters that sensitively correlate with biological endpoints. However, the digital transformation of medical imaging technology poses new challenges in the rational interpretation of the dense quantitative imaging information, creating the need for development and usage of novel inferential approaches, to overcome the limitations of current qualitative evaluation and exploit its full potential.

The present doctoral research aims to address challenges in the interpretation of multiparametric Magnetic Resonance Imaging (MRI) in neurologic and oncologic applications, and focuses on the incorporation and extension of the emerging data-driven inferential approaches that are based on advanced image analysis and statistical learning methodologies.

The first study investigated the molecular substrates of the brain functional responses to clinically relevant ongoing pain stimuli, as observed through the Arterial Spin Labelling (ASL) perfusion technique. More specifically, the study examined the spatial correlation of hemodynamic responses of two ASL datasets of acute and chronic ongoing pain patients, with neurotransmitter receptor distributions, as informed from Positron Emission Tomography data of independent studies, and from transcriptomic data of the human Allen Brain Atlas. The linear regression models have revealed moderate to strong associations of the hemodynamic responses with the distributions of opioid and dopamine receptor subtypes (R^2 values ranging from 0.14 to 0.35), which play a key role in the cerebral processing of pain signals, and especially the endogenous pain modulation mechanism. Differential associations were found for the serotonin

receptors examined. Additionally, the results highlight the utility of the adopted methodology as an easily applicable tool for enhancing the molecular specificity of functional MRI signals.

The second study aimed to develop a data-driven diagnostic model, based on an advanced multiparametric MRI dataset, for supporting the clinical task of differentiation between low- and high-grade gliomas. The multiparametric MRI data was analysed with a robust radiomic analysis workflow, including semi-supervised image segmentation, texture feature quantification, and machine learning - based feature selection and classification. The most discriminative features identified, were those obtained from the advanced MRI techniques, i.e., MR Spectroscopy (MRS), Diffusion Tensor Imaging (DTI) and Dynamic Susceptibility Contrast (DSC). The diagnostic model was based on a Support Vector Machine (SVM) classifier, evaluated with cross-validation, demonstrating a classification accuracy of 95.5%. Overall, the study demonstrates the value of utilizing multiparametric signal from advanced MRI and quantitative image analysis in the evaluation of brain tumor aggressiveness.

The third study presents a radiomic analysis application of multiparametric MRI data for differentiating benign from malignant breast lesions. The specific objective was to evaluate the potential of Ensemble Learning techniques in feature selection and classification steps of the analysis workflow, to increase the relatively moderate diagnostic accuracy of the previously reported models that were based on individual classifiers. The key findings of the study were the superiority of Diffusion Weighted Imaging (DWI) derived features that completely outperformed and substituted the T2-weighted (T2-w) MRI derived features, as well as the superiority of Boosting Ensemble Learning compared to SVM classification models (Area under Receiver Operating Characteristic curve (AUC)= 0.95 vs. 0.88).

Overall, the doctoral research demonstrates the enhanced perception regarding the underlying biological processes, gained from the combination of advanced imaging protocols, while further exploitation of advanced computational tools facilitates the development of powerful diagnostic models for supporting personalized interventions in the clinical setting.

Contents

Introduction

The role of biomedical imaging has expanded considerably since the advent of digital technology in the 1970s and 1980s, highlighted by the major achievements in the field of Computed Tomography (CT), which have enabled the generation of images of high quality and clinical utility with low radiation dose. Afterwards the addition of Magnetic Resonance Imaging (MRI) and Positron Emission Tomography (PET) in the clinical setting brought forth a new level of soft-tissue representation which further improved the understanding of molecular physiology (1).

Particularly MRI has emerged as the spearhead in various medical imaging applications because it can provide enriched anatomical and functional information, and more importantly with the use of harmless static magnetic fields and non-ionizing radiation. Over the last two decades MRI has brought a significant advancement in the field of neuroimaging where it has given the opportunity to access the brain non-invasively and measure a wide range of highly informative brain tissue properties (gross anatomy, neuronal activity, vascularity, connectivity, pathology etc) (2). So far, MRI has a pioneering and well-established role in functional neuroimaging, highlighted by the numerous accomplished studies focussing on cognitive/behavioural, aging, neurodegenerative disorders, etc paradigms (3). Furthermore, MRI has a profound impact in oncologic imaging establishing a central role in the detection and diagnosis of soft-tissue cancerous lesions, by means of assessing various spatiotemporal phenotypic features (e.g., tumor density, pattern of enhancement, cellular composition, regularity of tumor margins, and affection of the surrounding or distant tissues) (4). As such, MRI has emerged as a powerful tool for complementing the current standard methods of invasive biopsy, towards the comprehensive characterization of tumor heterogeneity, which is a critical component of tumor growth that also drives the selection of modern targeted therapies.

Overall, MR scanners have been transformed from simple imaging modalities into advanced computational systems producing a variety of numerical parameters related to tissue properties and have proven to be an important technology in medical research and clinical practice that holds great potential to improve our understanding regarding pathophysiological substrates and aid the clinical decision making.

Despite the advances in medical imaging technologies, there remains a gap between the macroscopic pathophysiological-related phenomena captured by the advanced imaging scanners and the underlying molecular and genetic mechanisms of the disease, that give rise to them (5). This gap is further enhanced when considering the current standard methods of qualitative assessment, due to the endogenous complexity of the physical principles exploited by such sophisticated imaging protocols, as well as the complexity of the biological correlations that they reflect. It is evident that straightforward clinical interpretations are not always feasible, and this poses additional challenges in terms of rationalizing the abundant of the outcome quantitative metrics, especially on the basis of the current subjective visual evaluation of imaging features, that leads to high inter-reader variability in clinical interpretation and adherence to qualitative reporting paradigms (6).

The need to understand these complex mechanisms has long urged scientists to develop new methods in medical imaging research, focusing on the integration and computer assisted evaluation of radiological images and patient specific pathophysiologic characteristics. The initial research initiatives have been focused on expanding the existing computer vision practices, tracing their roots to the early 1960s, towards the systematic evaluation of imaging biomarkers with potential to support the overall clinical assessment, demonstrating fair efficiency (7). Recently, however, the transition to enterprise digital imaging and re-emergence of statistical learning algorithms (i.e., Machine Learning, ML) have led to the development of many high-throughput quantitative imaging models aiming at disentangling complex imaging and biological correlations with data-driven approaches, to assist and augment physicians'

decision-making, featuring further automation and reliability (1) (Figure 1). Today, in the era of Big Data and Artificial Intelligence (AI) innovations, several promising streams of research work towards integrating the quantitative information from the different clinical sources, including the advanced imaging modalities, and exploiting advanced analytical methods for making clinically meaningful conclusions towards a personalized and more preventive healthcare (1).

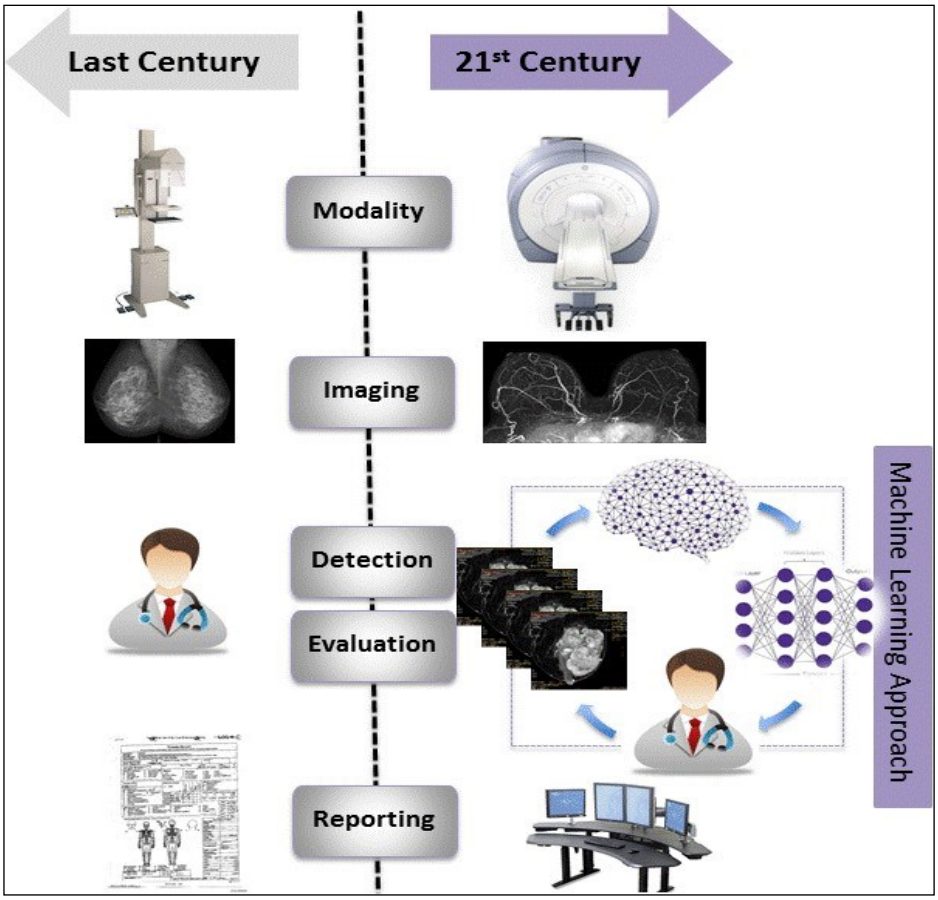

Figure 1: The evolution of medical imaging taking advantage of the new powerful modalities and advanced techniques such as MRI, as well as the promising era of a machine learning approach towards the individualization of medical care and precision oncology. (Adopted without changes from (8) Tsougos et al. Application of Radiomics and Decision Support Systems for Breast MR Differential Diagnosis. Computational and Mathematical Methods in Medicine, Volume 2018, DOI: 10.1155/2018/7417126, under the terms of the Creative Commons Attribution 4.0 International License http://creativecommons.org/licenses/by/4.0/)

this page intentionally left blank

Thesis Objectives, Outline, and Innovation

Following the recent advances in the field of biomedical imaging, the present thesis deals with MRI applications in neurologic and oncologic imaging with a special focus on the emerging analytical methods in the integration and data-driven interpretation of multimodal/ multiparametric imaging information. More specifically, the present thesis aims:

a) to address current challenges of specific clinical MRI applications and showcase the benefits of exploiting multimodal/multiparametric imaging information,

b) to identify and validate robust clinically relevant imaging biomarkers, and

c) to validate and expand ML-based quantitative imaging models for supporting multiparametric MRI diagnosis.

The thesis is structured into three parts that include the theoretic background and original research studies within the fields of MR functional neuroimaging (Part A) and oncological imaging (Part B), followed by a general discussion of the findings (Part C).

Part A intends to address the inherent inability of functional MRI to provide the molecular correlates of the observed hemodynamic changes, relevant to clinical questions, and increase its molecular specificity by means of utilizing PET and transcriptomics data. More specifically, after setting the background in Chapter 1, the study presented in Chapter 2 examines the spatial concordance of Cerebral Blood Flow (CBF) increase in two cohorts of clinically relevant on-going pain and neurotransmitter receptor cerebral distributions derived from PET templates of healthy participants studies and corresponding receptors' messenger Ribonucleic Acid (mRNA) expressions from the Allen Brain Atlas (ABA). Overall, the results have shown a strong spatial matching of CBF changes with opioidergic and dopaminergic receptors distributions, that highlight the association of the observed hemodynamic changes with the function of the well-

known endogenous pain modulation mechanism. Additionally, the biologically validated findings highlight the significant utility of the spatial correlation approach as a low-risk/low-cost hypothesis generating tool that benefits from existing multimodal datasets to bridge the translational gap between the advancing knowledge gained from functional MRI and the neurotransmitters systems that underly painful experiences.

Part B is dedicated to the innovative data-driven inferential approaches, termed Radiomics, aiming in the comprehensive non-invasive characterization of tumor pathophysiological profile, with potential to complement the current standard biopsy-based methods of assessment and support the personalized clinical decision making. The detailed background is described in Chapter 3. The study in Chapter 4 evaluates an ML diagnostic model for differentiation between Low- and High-Grade Gliomas. The study has applied a robust radiomic analysis model on an advanced multiparametric MRI protocol of glioma patients. The diagnostic model has demonstrated an accuracy of 95.5% in the diagnosis of glioma grade status, while it was the first study exploiting and reporting biomarkers from a complete advanced multiparametric MRI protocol, including Diffusion Tensor Imaging (DTI), Dynamic Susceptibility Contrast Enhanced (DSCE) MRI and MR Spectroscopy (1H-MRS). Chapter 5 presents an application of radiomic analysis evaluation of multiparametric MRI for differentiating benign from malignant breast cancer. The specific objectives of the study were the validation of robust breast MRI imaging biomarkers, as well as to demonstrate the added value of utilizing Boosting Ensemble Learning classification techniques, compared to the more conventional classification algorithms utilized by previous studies. The key finding of the specific study were the superiority of Diffusion Weighted Imaging (DWI) biomarkers compared to T2-weighted (T2-w) MRI, as well as the superiority of the specific Ensemble Learning classification model compared to the previously reported ML models.

Part C, Chapter 6 discusses the objectives and results of the reported studies, as well as open challenges and future considerations in the field of biomedical imaging analytics.

The key findings of the individual studies of the present Doctorate Thesis have been disseminated through the following conference presentations and peer-reviewed publications:

List of Publications in Peer-reviewed Scientific Journals

1. **Alexandros Vamvakas**, Timothy Lawn, Mattia Veronese, Steven Williams, Ioannis Tsougos, Matthew Howard, Neurotransmitter Receptor Densities are Associated with Changes in Regional Cerebral Blood Flow During Clinical Ongoing Pain, Human Brain Mapping, 2022, https://doi.org/10.1002/hbm.25999

2. **Alexandros Vamvakas**, Dimitra Tsivaka, Andreas Logothetis, Katerina Vassiou, Ioannis Tsougos, Breast Cancer Classification on Multiparametric MRI – Increased Performance of Boosting Ensemble Methods, Technology in Cancer Research & Treatment 21 (2022): 15330338221087828.

3. Timothy Lawn, Ottavia Dipasquale, **Alexandros Vamvakas**, Ioannis Tsougos, Mitul Mehta, Matthew Howard, Differential Contributions of Serotonergic and Dopaminergic Functional Connectivity to the Phenomenology of LSD, Psychopharmacology 239, 1797-1808 (2022), https://doi.org/10.1007/s00213-022-06117-5

4. **A. Vamvakas**, S. Williams, K. Theodorou, E. Kapsalaki, K. Fountas, C. Kappas, K. Vassiou, I. Tsougos, Imaging Biomarker Analysis of Advanced Multiparametric MRI for Glioma Grading, Physica Medica: European Journal of Medical Physics, 2019, Volume 60, Pages 188-198, DOI: 10.1016/j.ejmp.2019.03.014

5. Ioannis Tsougos, **Alexandros Vamvakas**, Constantin Kappas, Ioannis Fezoulidis, and Katherine Vassiou, Application of Radiomics and Decision Support Systems for Breast MR differential diagnosis, Computational and Mathematical Methods in Medicine, Volume 2018, 8 pages, DOI: 10.1155/2018/7417126

List of Publications in Book Chapters

1. **Alexandros Vamvakas**, Katerina Vassiou, Dimitra Tsivaka, Ioannis Tsougos., Chapter 31: Decision Support Systems in Breast Cancer, in "Precision Medicine for Investigators, Practitioners and Providers", Editors Joel Faintuch, Salomao Faintuch, Elsevier Inc., Nov 2019, ISBN: 9780128191781#

List of Publications in National (Greek) and International Conference Proceedings

1. **Alexandros Vamvakas**, Eftychia Kapsalaki, Constantin Kappas, Ioannis Fezoulidis, Ioannis Tsougos, Imaging Biomarker Analysis of Structural MR Images for Glioma Grading, 2nd European Congress of Medical Physics (ECMP), Copenhagen, Denmark, August 2018
2. **A. Vamvakas**, S. Williams, K. Theodorou, E. Kapsalaki, K. Fountas, C. Kappas, K. Vassiou, I. Tsougos, A Radiomic Analysis Approach of Multiparametric MRI for Glioma Grading, 25th European Congress of Radiology (ECR), Vienna, Austria, February-March 2019
3. **A. Vamvakas**, E. Kapsalaki, K. Fountas, S. Williams, K. Theodorou, K. Vassiou, I. Tsougos, Multiparametric MRI Radiomics towards Differentiating Low- and High-Grade Gliomas, Intracranial Glioma Workshop: From A to Z, Athens, Greece, May 2019
4. **Alexandros Vamvakas**, Dimitra Tsivaka, Andreas Logothetis, Katerina Vassiou, Ioannis Tsougos, Evaluation of 3T multiparametric MRI with radiomic analysis for differentiating benign and malignant breast lesions, 27th European Congress of Radiology (ECR 2021), Vienna, Austria, February-March 2021
5. **A Vamvakas**, K Vassiou, G Tzovaras, G Fezoulidi, M Vlychou, I Tsougos, Feasibility of bi-parametric MRI delta-radiomic features for assessing pathological complete response in locally advanced rectal cancer neoadjuvant chemoradiotherapy, 3rd European Congress of Medical Physics (ECMP), Torino, Italy, June 2021

6. **A Vamvakas**, T Lawn, M Veronese, S Williams, I Tsougos, M Howard, Investigating molecular indices of CBF in ongoing pain through spatial correlation of ASL and PET, Brain & Brain PET 2022, Glasgow, United Kingdom, May-June 2022

7. **A Vamvakas**, T Lawn, M Veronese, S Williams, I Tsougos, M Howard, Correlation of ASL-MRI with PET and mRNA expressions can reveal molecular substrates of Cerebral Blood Flow in clinical ongoing pain, 1st Panhellenic Congress of Medical Physics (PCMP), Athens, Greece, September 2022

this page intentionally left blank

PART A

Functional Neuroimaging Applications

this page intentionally left blank

Chapter 1

1.1 Background

The advent of whole-brain neuroimaging techniques has shown great promise in the development of novel measurements of regional changes in brain function that have shed light on the cerebral underpinnings of either the ‘natural state’ of brain activity, e.g., resting-state connectivity, baseline receptor availability, etc., or various physiological, pharmacological, or task-based/behavioural (sensory, cognitive, stimuli, etc.), interventions (2). In particular, functional MRI (fMRI) has emerged as an important tool to map mental processes to their neurobiological substates, characterize dysfunction of the brain in a variety of clinical conditions, and study the brain's response to pharmacological challenges (5).

fMRI captures hemodynamic responses which are secondary to the underlying neuronal activation. In principle, neurotransmitter release and binding at the synapses convert chemical signals to electrical activity in the neurons. The sodium-potassium (K^+-Na^+) pumping and the various metabolic processes related to the synaptic and neuronal activation increase the energy consumption of local neurons and astrocytes which is produced locally from glucose and oxygen supplied through small vessels (9). In response nearby vessels dilate, both directly via signalling molecules such as nitric oxide and adenosine and indirectly via astrocytes, ensuing a substantial increase of local blood flow which is accompanied by a change in blood oxygenation and glucose metabolism (10). These changes in vascular parameters described by the ‘’neurovascular’’ and ‘’neurometabolic’’ couplings are detected by fMRI and lead to different image contrasts respective to the fMRI sequence utilized (Figure 2).

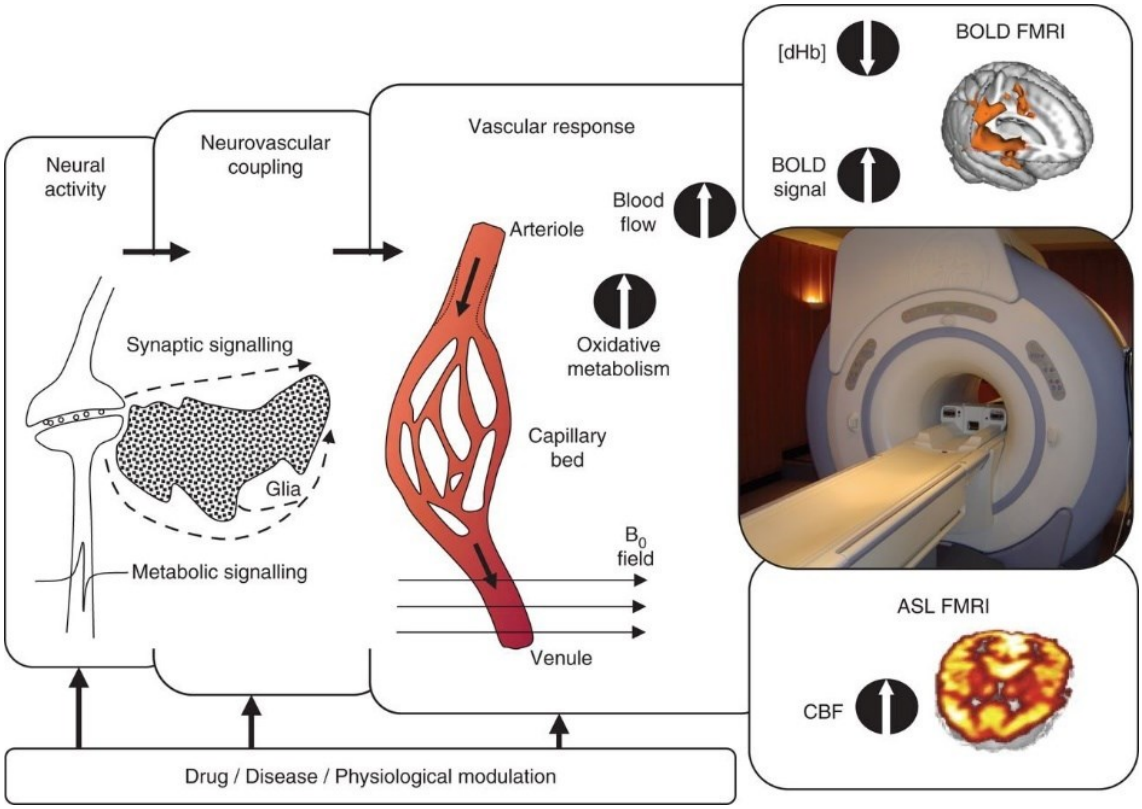

Figure 2: The Neurovascular coupling notion illustrated by the pathway from neural activity to the haemodynamic response that is the basis of the different fMRI image contrasts. (Adopted without changes from (11) Pattinson KT. Functional magnetic resonance imaging in anaesthesia research. Br J Anaesth. 2013;111(6):872-876. doi:10.1093/bja/aet288, under permissions obtained from RightsLink Digital Licensing and Rights Management Service)

The Blood Oxygen Level Dependent (BOLD) contrast summarizes the combined effects of vascular response, oxygen metabolism and cerebral perfusion (3). Together with advances in our understanding of brain anatomy, BOLD provides the ability to record changes in brain activity with a spatial resolution at the submillimeter level and a temporal resolution of seconds or less, and has expanded our understanding of the location, propagation, and connections of brain activity (12).

Arterial Spin Labelling (ASL) is another fMRI technique which uses magnetically labelled water in arterial blood as an endogenous diffusible tracer to measure perfusion noninvasively (13). ASL allows for the quantification of regional cerebral blood flow (rCBF) in absolute physiological units, as a surrogate marker of 'natural state' of neural activity. Whilst the BOLD

signal reflects a composite effect of changes in blood flow, vascular volume, and oxygen metabolism (14), partially prone to substantial inter-subject/session variabilities, ASL is considered to have better characteristics than BOLD in terms of localization of the activation and reproducibility (15), however to a reduced spatiotemporal resolution and Signal-to-Noise-ratio (SNR) compared to BOLD signal.

As it was mentioned before, signal transduction in the brain is accomplished by the release and binding of neurotransmitters at the synapses, which leads to the activation or inhibition of specific neuronal pathways. Neurotransmitters thus play an important role in modulating the brain's activity at the molecular level (12). fMRI has been previously used as an indirect marker to image the functional response of neuroreceptors to drugs or stimuli that target specific receptor sites, also termed pharmacological MRI (phMRI) (16,17). However, the main limitation of phMRI is its inability to provide a molecular insight into the main effect of how excitatory and inhibitory neural activity adds up to influence the fMRI signal and support the neurovascular coupling chain (12,14). This is because fMRI is no selective to receptors, therefore the degree to which the observed responses reflect the action at specific target sites, remains elusive (18). Consequently, the utility of fMRI signal in addressing core neuroscientific questions in the cellular and molecular level is constrained by its indirect nature and inherent inability to provide information as to the microscopic processes that give rise to it (5).

Direct evaluation of human brain chemistry in vivo has been made possible with PET examining the dynamics of the regional uptake of selective radiotracers that present high biochemical specificity (3). PET has served as evidence of the local neurochemical modulation of brain activity, induced by pharmacologic and behavioral challenges, that can be inferred through their effects on changes in receptor binding and related outcome measures (3,12). Such settings include but are not limited to, direct binding of exogenous drugs, endogenous release of neurotransmitters triggered by exogenous drugs or behavior/stimuli, etc. More specifically, a radiolabelled compound that targets specific receptor system is administered to obtain the

baseline receptor occupancy. Subsequently, the release of endogenous neurotransmitters, triggered by drugs or stimuli, or the action of exogenous compounds with relevant receptor (ant)agonist action can be monitored by means of the observed loss in the radiotracer concentration, as less receptors become available for binding, leading the excess radiotracer molecules to be washed out through local vascularity.

Despite the low spatiotemporal sensitivity, PET has high specificity for the molecular correlates of brain activities. Recently, combination of fMRI and PET data have shown unique opportunities in associating specific neurochemical events to functional hemodynamic activation and investigating the impacts of neurotransmission on neurovascular coupling of the human brain (2). Figure 3 presents co-occurrent/co-localized effects in receptor binding and cerebral blood volume induced by dopamine D2 antagonist raclopride injection in primate brains, as measured by PET and fMRI, respectively.

However, on-site standalone PET or hybrid PET/fMRI provides only relatively inflexible paradigm designs, mainly constrained by the PET-related prohibitive costs, hardware demands, and invasiveness (3,15). Moreover, depending on the radiotracer, a PET scan can be only selective for one neurotransmitter at the time and, due to radioactivity exposure and tracer availability, therefore only a few chemicals can be measured in a subject at a given time. A possible way of addressing the limitations posed by on-site PET acquisition for probing neurotransmitters dynamics, comes from the Receptor Theory (19). Specifically, according to Receptor Theory it can be assumed that relationships between drug kinetics and observed pharmacodynamic effects depend on both the drug (i.e., receptor affinity) and the biological system (i.e., receptor density). Based on this concept compounds with high affinity for specific receptor systems should lead to higher neuro-vascular/metabolic changes in regions with higher respective receptor densities. In this context, exploitation of normative templates from individual PET studies that quantify whole brain receptors' densities,

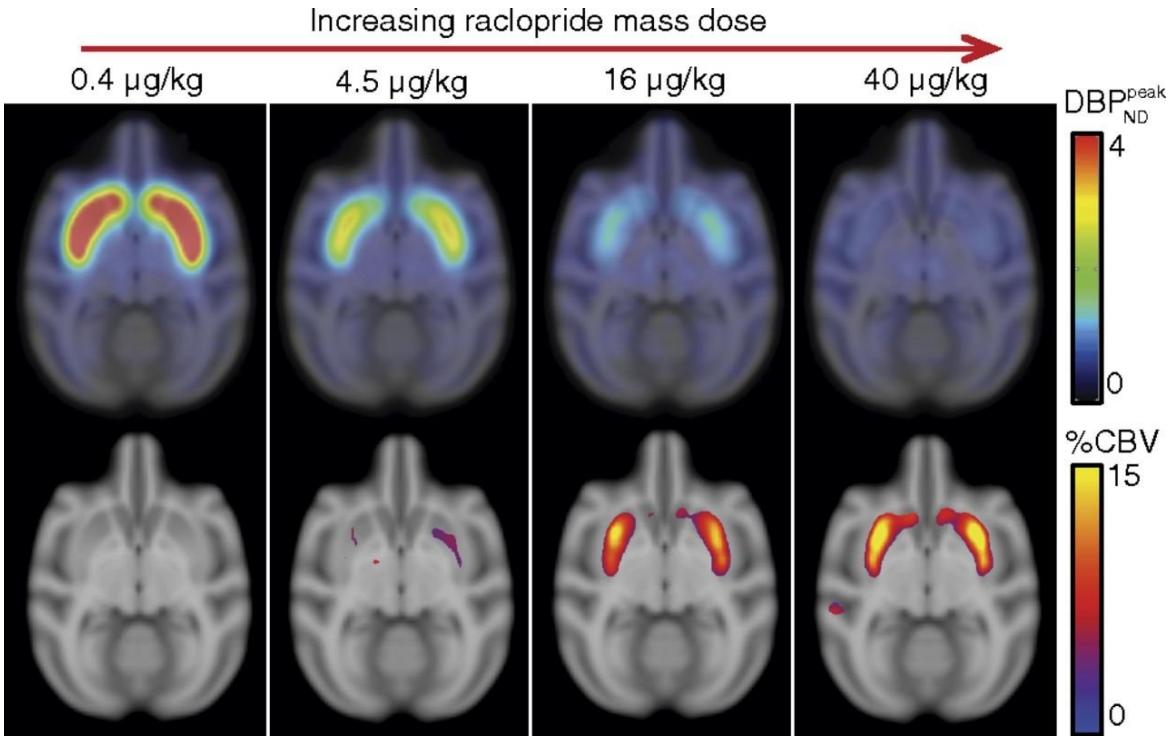

Figure 3: Effects on BPnd (upper) and CBV (lower) induced by D2 antagonist administration, illustrating the similarities in the spatial distribution of PET/fMRI signals. All maps are created from data from two animals with a mixed-effects model. (Adopted without changes from (20) Sander, C. Y., Hooker, J. M., Catana, C., Normandin, M. D., Alpert, N. M., Knudsen, G. M., Vanduffel, W., Rosen, B. R., & Mandeville, J. B. (2013). Neurovascular coupling to D2/D3 dopamine receptor occupancy using simultaneous PET/functional MRI. Proceedings of the National Academy of Sciences of the United States of America, 110(27), 11169–11174, under permissions provided by Proceedings of the National Academy of Sciences of the United States of America (PNAS)).

assuming its magnitude to be a linear function of receptor spatial distribution and availability across brain regions (2). To date, this approach has been efficiently used by several studies, mainly to map functional haemodynamic activation induced by different compounds onto distributions of their relevant target receptors (18,19,21,22,23).

In a recent study, Dipasquale et al. have proposed the Receptor-Enriched Analysis of functional Connectivity by Targets (REACT), that is a dual regression statistical framework for examining spatial covariations of BOLD fMRI with normative PET receptor templates. In the original study, REACT has identified serotonergic patterns of brain activation after MDMA administration (18). Lawn et al., have used REACT in an exploratory analysis to examine

neurochemically distinct components of Lysergic Acid Diethylamide (LSD) – induced functional connectivity, and have found significant correlations with the serotonergic and dopaminergic receptor systems (22).

Similarly, combined ASL/PET imaging studies have been applied to address the molecular basis of regional changes in cerebral blood flow induced by pharmacological action (19,21). Selvaggi et al. tested the association of the main effects of three different antipsychotic drugs (D2 receptor antagonists) on rCBF by correlating rCBF maps with normative BPnd maps of D2R protein density using voxel-wise regression analysis (21). Their results indicated that the functional effects of antipsychotics as measured with rCBF are tightly correlated with the distribution of their target receptors in striatal and extra-striatal regions, demonstrating the link between neurotransmitter targets and haemodynamic changes and reinforcing rCBF as a robust in-vivo marker of drug effects. Of note, the JuSpace (https://github.com/juryxy/JuSpace) is a useful toolbox providing a range of receptor PET templates and statistical tools for performing spatial correlation analysis with resting-state fMRI and ASL imaging data (24).

Despite the important contribution of in-vivo PET imaging for probing neurotransmitter systems, as described above, currently these applications have limited capacity mainly because appropriate radioligands exist only for a small number of target receptors. As a result, lately there is an increasing interest for alternative sources of informing the neurotransmitter receptor cerebral distributions. Dukart et. al. have previously utilized publicly available Autoradiography data (25) to inform receptor distribution. Autoradiography refers to the ex-vivo quantification of receptor distributions by high resolution PET of post-mortem samples. Although numerous radioligands exist for autoradiography that may be used to quantify a wide range of neuroreceptors, however the coverage of the whole brain of the current published data is still low.

To account for the missing proteomic information biology studies have used corresponding gene expression as a surrogate to inform receptor distribution (26). Towards this direction, the

contribution of the multimodal Human Allen Brain Atlas (27), that integrates anatomic and genomic information covering the whole brain, has been significant. The atlas features mRNA expression measures for >20,000 genes, profiled by about 60,000 microarray probes in different brain regions, obtained from six healthy adult human donors. More importantly, with the prior use of structural MRI, the locations of the tissue samples have been mapped into the standard MNI coordinates system, thus ABA may serve as a reference standard to explore relationships between gene expressions and in vivo functional imaging data (Figure 4). Selvaggi et al. study, has also investigated the same relationship at the gene expression level using post-mortem brain mRNA expression measures of the DRD2 gene.

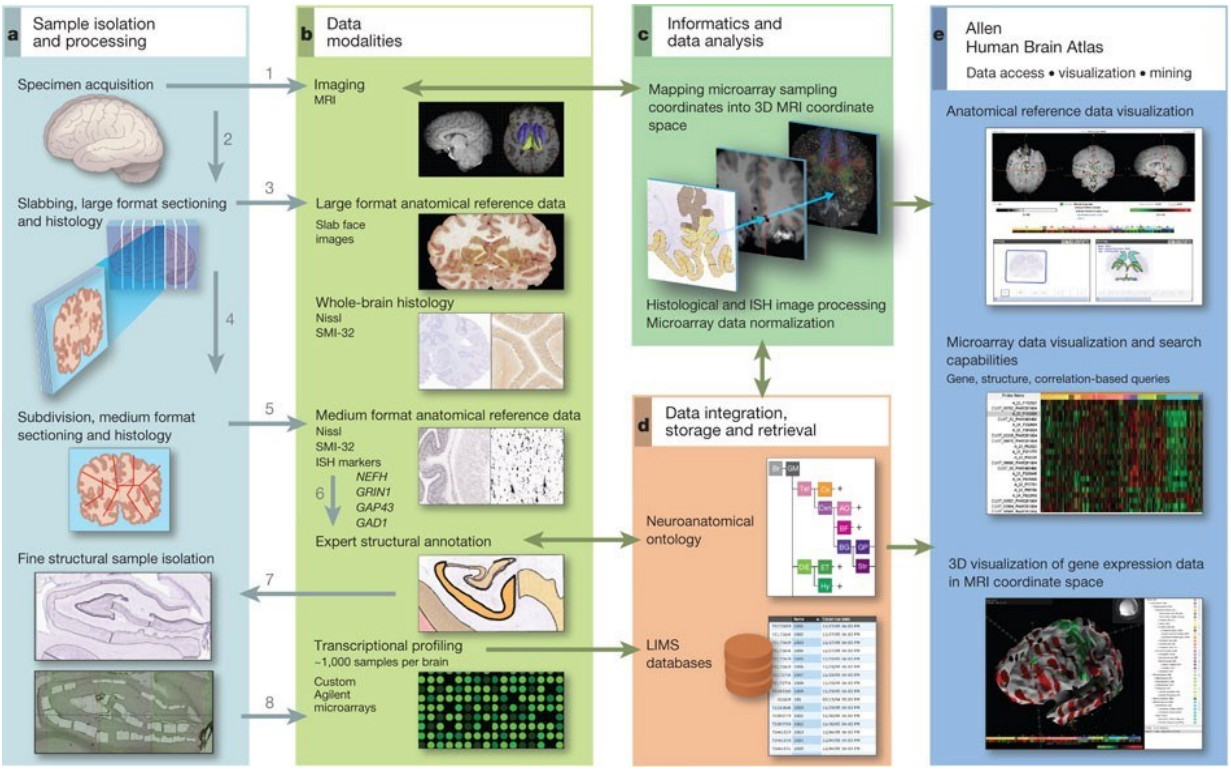

Figure 4: Overall procedure followed by Hawrylycz MJ et. al for microarray data generation (a,b), mapping microarray sampling coordinates into 3D MRI coordinate space (c) and data visualization and mining tools contained in the ABA online public data resource. (Adopted without changes from (27) Hawrylycz MJ, Lein ES, Guillozet-Bongaarts AL, et al. An anatomically comprehensive atlas of the adult human brain transcriptome. Nature. 2012;489(7416):391-399. doi:10.1038/nature11405, under permissions obtained from RightsLink Digital Licensing and Rights Management Service).

In general, the average distribution of receptor density and gene expression seems to offer useful approximations for the influence of a given receptor or gene over the fMRI signal in each region. This is primarily evidenced by the fact that molecular-enriched analyses to date have found hypothesis-driven pharmacodynamic effects in line with the known receptor affinity and (ant)agonist activity of different drugs. However, the utility of such methods in non-pharmacological interventions and pathophysiological neural correlates remains unknown. Based on the reported findings the below study aims to assess the usage of the technique and address its efficacy, advantages, and limitations in the clinical ongoing pain paradigm.

Chapter 2

2.1 Investigating molecular indices of CBF in ongoing pain through spatial correlation of ASL-MRI, PET, and anatomical mapping of in-vivo mRNA expressions

2.1.1 Aims and Objectives

Persistent pain is a major health problem, affecting the quality of millions of lives globally and imposing a burden on healthcare systems. Despite recent advances in our mechanistic understanding of pain, there remains a need for novel, efficacious treatments for persistent pain (28). Major limitations of existing therapies include high Number-Needed-to-Treat rates (NNT) and the short-term sustainability of treatment effects (28,29). Moreover, many analgesic pharmacotherapies are associated with a variety of side effects resulting in a narrow therapeutic window. For example, while Nonsteroidal Anti-Inflammatory Drugs (NSAIDs) offer some benefit, they increase risks of ischemic cardiovascular events and can impair renal function (29). Opiates, the prototypical analgesic, show little sustained benefit for chronic pain and are associated with serious gastrointestinal and cognitive side effects as well as risk of abuse and addiction (29).

Historically, pharmacological studies have relied entirely upon participants' self-reports to quantify their pain experiences, but interindividual differences in pain responses have hampered patient stratification and development of novel treatments (30). Chronic pain had been viewed

as ‘acute pain that is lasting too long’, with prolonged nociceptive input from sensitized nociceptors or damaged nerve fibres (14). However, activation of nociceptors is neither sufficient nor necessary to produce a pain experience (31). For example, severity of joint damage in osteoarthritis correlates only weakly with the experienced pain (32) and a given intensity of noxious stimulation can produce vastly diverging levels of reported pain (33). Additionally, chronic pain patients often suffer psychiatric comorbidities including depression and anxiety (14), while emotional state, context and prior experiences can profoundly alter the pain experience (31). Collectively, these highlight the importance of the Central Nervous System (CNS) in not only the conversion of nociceptive input into conscious pain perception, but also its complex modulation (14). Therefore, methods to unravel complex supraspinal mechanisms that occur to amplify and maintain pain are critical to both our understanding of, and ability to treat, chronic pain conditions (34).

Whole-brain neuroimaging techniques, such as BOLD and fMRI, have provided insight into how the coordinated activity across multiple brain regions, referred to as “functional connectivity,” contribute to pain perception and its modulation (35). Beyond evoked pain paradigms, resting-state BOLD has been also used to collect information about the ‘natural state’ of brain activity in order to identify differences in functional connectivity of medium-term brain activity in chronic pain individuals (13,34). Additionally, ASL is gaining interest in pain research (13), as this approach allows for the quantification of rCBF in absolute physiological units, as a surrogate marker of neural activity. More importantly, ASL is more sensitive in capturing low-frequency signal fluctuations compared to evoked-response BOLD fMRI, making it well suited to characterise brain activity associated with ongoing or spontaneous pain observed in numerous pain phenotypes including postsurgical, orofacial neuropathic and musculoskeletal pain (13,15,30,36,37).

Despite the utility of these techniques for understanding the neural correlates of both acute and chronic pain conditions, they are inherently unable to delineate the neurochemical

substrates underlying the fMRI signal (12,14). An important aspect of understanding interindividual variations in pain experience is the study of neurochemical substrates of the brain function involved in both nociception but also neuroplastic phenomena increasingly accepted to occur in patients with chronic pain. It is evident that the development of chronic pain interventions and monitoring of clinical outcomes requires indices to address pain modulation processes at a molecular level, as neurotransmitter concentrations and receptor binding are the main targets of pain-relieving drugs. Analgesic drugs mediate their effects through modulating neurotransmitter systems at the molecular level. As such, there remains a gap between the significant advances in understanding pain processing indexed by neurovascular coupling and the targeting or development of existing or novel treatments to these molecular systems. Integration of PET offers an opportunity to probe these molecular systems using selective radiotracers, and highlight the neurochemical signatures involved in the functional networks indexed by fMRI (2,3,15). For example, it has confirmed in humans the existence of an "opioid-sensitive" Descending Pain Modulatory System (DPMS) that is relevant to human experience in many settings, including its involvement in pharmacological and nonpharmacological analgesia (15,31,38). In a previous study, Wey et al. utilized simultaneous PET/fMRI to directly correlate neuroreceptor occupancy with regional haemodynamic changes in pressure pain and showed that pain induced changes in opioidergic neurotransmission contribute a significant component of the fMRI signal (39). Karjalainen et al. have collected PET/fMRI data from healthy participants to illustrate the role of opioid and dopamine systems in nociceptive processing of vicarious pain stimulation (40). However, integration of either standalone PET or hybrid PET/fMRI have relatively inflexible paradigm design opportunities, constrained by dose-radiation limits and the half-life of both the drug and the tracer isotope, as described in the previous chapter. To overcome limitations posed by on-site PET acquisition, exploitation of normative Binding Potential (BPnd) templates from individual PET studies has become increasingly popular to inform neurotransmitter related activity, assuming its

magnitude to be a linear function of receptor spatial distribution and availability across brain regions (2).

Despite the utility of ASL in characterising ongoing pain, to date no study has attempted to explore its underlying neurochemical basis. In line with the previous reports, here we hypothesise that the spatial distribution of neurotransmitter receptor densities quantified by PET can inform the pain related ASL signal change to gain insight into the molecular substrates of ongoing pain. To test this, we explored associations of rCBF differences of pain versus non-pain conditions with available normative BPnd templates of the μ-opioid, dopamine D2 and 5-hydroxytryptamine (5-HT) receptor subtypes. These were selected given their important, yet diverse, roles in pain processing and endogenous pain modulation. We also incorporate receptors' mRNA expression profiles, extracted from the ABA, to inform the underlying receptor distribution by means of transcriptomics. The methodology is applied to two individual datasets of well-established pain models, which were previously utilized in the respective studies of Howard et al. (30,41), in order to extent these reports, by exploring the neurochemical basis of the specific pain-related rCBF changes identified: i) acute post-operative ongoing pain following lower jaw Third Molar Extraction (TME) (41) and ii) chronic pain secondary to hand Osteoarthritis (OA) (30). To our knowledge, this is the first study examining the relationship of ASL-derived CBF changes with neurotransmitter receptors profiles and mRNA expression distributions in spontaneous and persistent, clinically relevant pain.

2.1.2 Material and Methods

TME participants and study design

The study was approved by King's College Hospital NHS Research ethics committee (Ref 07/H0808/115). Sixteen right-handed, healthy, male volunteers aged 20–41 (mean age=26.4 years) provided written informed consent to participate. All participants were examined by oral

surgeons at the King's College London Dental Institute and diagnosed with bilateral recurrent pericoronitis.

Participants were invited to participate in the study in response to a university circular email requesting patients requiring wisdom tooth removal or following referral from their primary care dentist to the dental institute for third molar extraction. All participants fulfilled NICE (2000) guidelines for recommended extraction of lower jaw left and right third molars (41). Female participants were excluded due to possible variability induced by the phase of the menstrual cycle on cerebral haemodynamics and postsurgical pain responses (42). Other exclusion criteria were: Prescribed oral nitrates, usage of tramadol, codeine, NSAIDs or paracetamol within 12h before each session, consumption of alcohol for 24 hours prior to each session, caffeine-containing products for 6 hours prior to each session, tobacco- or nicotine-containing products for 4 hours prior to admission, history of psychosis or psychological disease, known history of other disorder which is strongly associated with polyneuropathy, including alcohol, existing problems (e.g., uncontrolled hypertension, renal failure, cancer, liver disease, severe spinal trauma, active thyroid disease, congestive heart failure, etc.), smoking of more than 5 cigarettes per day or consumption of more than 6 cups of caffeinated drinks per day, any evidence of a history or current use of drugs of abuse, a non-Caucasian ethnicity, any person unable to lie still within the environment of the fMRI scanner for the required period to perform the study and those where MRI scanning were contraindicated (metal, pacemaker, etc), any person unable to understand and follow the instructions of the investigators.

Participants were scanned on five separate occasions (S1–S5); screening/familiarisation (S1), pre-surgical (S2) and post-surgical sessions (S3) for the first extraction and pre-surgical (S4) and postsurgical (S5) sessions for the second extraction. An interval of at least two weeks separated S3 and S4, to ensure that participants had completely recovered from their first surgery and were not experiencing any residual pain. MR examinations during sessions S2–S5 were identical, while the order of left and right tooth extraction was balanced and pseudo-

randomised across the group. Post-surgical pain scanning sessions were commenced following recordings of three consecutive VAS scores greater than or equal to 30/100 on a 100mm pen-and paper VAS, each spaced ten minutes apart. During all scanning sessions, estimates of ongoing pain intensity were obtained using a computerized Visual Analogue Scale (VAS), anchored with 'no pain' and 'worst pain imaginable', displayed on a screen visible to participants at the foot of the scanner bed. Computerised VAS scores had a range of 0-100, with identical anchors (41).

OA participants and study design

The study was approved by the local NHS research ethics committee (Ref 07/H0807/69) and sixteen right-handed postmenopausal female subjects 18-80 years of age (mean age = 60.8 years) who fulfilled the American College of Rheumatology criteria for carpometacarpal (CMC) OA in their dominant (right) hand provided written informed consent to participate in the study (30). Importantly, OA patients were included only if they suffered from pain around one of the first carpometacarpal joints due to the osteoarthritis, and the pain duration was greater than 6 months, and they did not have severe pain elsewhere in the body. Additionally, seventeen age- and sex-matched controls (with a mean age of 64.7 years) provided written informed consent to participate in the study (30).

Exclusion criteria for the study were: Acute joint trauma of the hand within 12 months of commencing the study, history of psychosis or psychological disease requiring ongoing psychoactive drugs (excluding anti-depressants stable in dose for at least 3 months and not anticipated to change), use of prohibited medications, in the absence of appropriate washout periods, such as oral or intramuscular corticosteroids within 4 weeks prior to screening, monoamine oxidase inhibitors within 2 weeks of screening, analgesic agents, other than NSAIDs, Cox-2 inhibitors, or acetaminophen within 1 week prior to screening [Note: Aspirin

use of less than 325 mg per day for cardiovascular prophylaxis was permitted. The use of NSAIDs, Cox-2 inhibitors and compound analgesic medications (containing low-dose opioid components) was permitted provided the patient was on a stable regimen for at least 4 weeks prior to screening and for the duration of the study. Acetaminophen up to 4 g/day was permitted, provided it was not used in the 24 hours prior to each session], intra-articular steroids into the study joint within 12 weeks, and to any other joint within 4 weeks prior to screening, clinically significant or unstable medical or psychological conditions that, in the opinion of the investigator, would compromise participation in the study, smoking of more than 5 cigarettes per day or consumption of more than 6 cups of caffeinated drinks per day, any evidence of a history or current use of drugs of abuse, consumption of alcohol for 24 hours prior to each session, caffeine-containing products for 6 hours prior to each session, tobacco- or nicotine-containing products for 4 hours prior to admission, any person unable to lie still within the environment of the fMRI scanner for the required period to perform the study and those where MRI scanning were contraindicated (metal, pacemaker, etc), any person unable to understand and follow the instructions of the investigators.

The study consisted of 2 identical sessions, separated by a minimum of 7 days and a maximum of 21 days. Each session involved a screening and familiarization stage prior to MRI. OA pain intensity estimates where acquired prior to and following each MRI session using a Numerical Rating Scale (NRS) ranging from 0 (no pain) to 10 (worst pain imaginable) (30).

MRI acquisition and pre-processing

Imaging was performed on a 3 Tesla Signa HDx whole-body MR imaging system (General Electric, (GE), USA) fitted with an 8-channel, phased-array receive-only head coil. High-resolution T1-weighted (T1-w) and T2-w MR structural sequences were acquired for radiological assessment and image registration, using 3D spoiled gradient recalled (resolution = 1 x 1 x 1 mm) and fast spin echo sequences, respectively. Resting-state rCBF measurements

were made using Pseudo-Continuous ASL (pCASL), using an irradiation time of 1.5 s and post-labelling delay of 1.5 s. pCASL images were acquired using a single-shot, 3D Fast Spin Echo (FSE) readout resulting in whole-brain blood flow maps, with scanning parameters as follows: time to echo 32 ms, repetition time 5,500 ms; echo train length 64, matrix size 48x64x60, Field Of View (FOV) 18x24x18 cm, and number of excitations 3 and spatial resolution of 1x1x3 mm.

Each TME participant was involved in four sessions: two pain-free and two during post-surgical pain. Each OA and control participant was scanned twice. Each MRI session comprised of six consecutive pCASL scans for TME and two consecutive pCASL scans for OA and control participants, respectively. The multiple scans were acquired because ASL is an inherently low SNR technique, thus averaging between scans and relevant sessions is expected to improve data quality (43). TME pain data were averaged across lateralised teeth, as previous investigations (41,43) had demonstrated no effects of stimulus laterality on rCBF.

Pre-processing was performed using FSL software version 4.1.5 (http://www.fmrib.ox.ac.uk/fsl) and Statistical Parametric Mapping software (SPM) version 12 (http://www.fil.ion.ucl.ac.uk/spm). For each subject, all collected ASL images within and across relevant pain sessions were co-registered with each other and a mean image generated [SPM]. The T2-w image was skull stripped using a brain extraction tool [FSL-BET] and the resulting brain-only image was co-registered with the average ASL image and used as a mask to exclude extra-cerebral signal [SPM-CO-REGISTER]. A nonlinear transformation was calculated between the mean ASL image and a custom ASL template in the standardized, stereotaxic co-ordinates of the MNI [SPM-NORMALISE]. The raw images were then transformed to MNI space in one interpolation step. The resulting images were smoothed with an 8 mm full width at half maximum isotropic Gaussian kernel [SPM] and masked to include gray matter voxels only. Probabilistic gray matter images in MNI space, derived from the FSL voxel-based morphometry toolbox, were thresholded to produce a mask which included all voxels from all subjects with a 20% likelihood of being gray matter. To account for the inter-

subject variability of global blood perfusion values, all normalized, smoothed images were scaled to have a median value of 1,000. This scaling was performed to increase reproducibility and to ensure that global inter-subject differences in CBF values did not confound later analysis (3).

ΔCBF profiles

Group level analyses to quantify CBF changes between pain vs non-pain states was performed in SPM, using paired and independent-group t-tests for TME and OA/controls datasets, respectively. Specifically, for each dataset a voxel-wise PAIN>NON-PAIN t-contrast map (ΔCBF) was calculated. Subsequently, the t-contrast maps of both datasets reflecting ΔCBF were segmented into the 85 Volumes of Interest (VOIs) provided by the Desikan-Killiany (DK) atlas (44). ΔCBF profile vectors for TME and OA-Controls were obtained by averaging the ΔCBF values of all voxels in each VOI.

Additionally, voxel-wise PAIN>NON-PAIN z-contrast maps were calculated, considering cluster-level Familywise Error rate (FWE) correction (p=0.05, cluster defining threshold= 0.001) according to the random field theory (45), to demonstrate areas of statistically significant pain-related increases CBF. The specific maps were not utilized in the subsequent analysis, however a sample of them is presented in Figure 9, along with corresponding DK atlas VOIs, as this might be valuable to the reader. Please also refer to the previous studies of Howard et al. (30,41) where a more extended analysis and discussion of the ASL findings in the specific cohorts is provided.

As it was mentioned before, in the current study we have considered uncorrected whole-brain t-contrast maps and all 85 cortical and subcortical VOIs as defined in the DK atlas to test the association of ΔCBF and receptor density profiles. The rationale for including the whole brain in the analysis, rather than focus only on the regions previously known to be implicated

in pain or those demonstrating a significant increase in CBF, is based on the fundamental assumption of the current study; namely, that if a neurotransmitter's activity is related to the pain stimulus, then the observed distribution of CBF change should spatially match the concentration of the respective neurotransmitter receptor within the whole brain. Thus, it is necessary to utilize all the available parcellations into the model in order to account the CBF variability across the whole brain, to perform an unbiased correlation for testing this hypothesis and confirming the validity of the technique. We anticipated that a whole-brain analysis might lead to weaker associations of ΔCBF with the neurotransmitter receptors distributions, due to the inclusion of receptor-rich regions that are not conventionally associated with pain processing. Nevertheless, beyond avoiding the statistical bias in the correlation models, there is also evidence that ongoing pain may be associated with increased blood flow in brain regions both within and outside those commonly associated with experiencing pain, for example, the somatosensory, prefrontal, and insular cortices, but also the superior parietal lobule, which is part of the dorsal attention network (14). Additionally, from a clinical perspective, the inclusion of all VOIs is important for comparing results between the different pain pathologies in which there may be subtly different patterns of rCBF alterations that relate to the phenotypic and demographic aspects of the cohorts in question.

Receptor BPnd profiles

Receptor BPnd profiles were obtained from previously published PET templates quantified from healthy subjects. Density of μ-opioid receptor expression as revealed by [11C]carfentanil PET scans from 89 healthy volunteers (46) was acquired from the Neurovault collection [https://identifiers.org/neurovault.image:115126]. Dopamine receptor D2/D3 expression was extracted from an independent [18F] Fallypride PET template obtained by averaging six BPnd

maps of healthy young volunteers (47). The publicly available high-resolution in vivo atlas of four serotonin receptors, i.e., 5-HT1A, 5-HT1B, 5-HT2A, and 5-HT4 (https://xtra.nru.dk/FS5ht-atlas/), created from molecular high-resolution PET scans acquired in 210 healthy individuals with different selective PET-radioligands was also utilized (48). Similar to the process followed for ΔCBF profile vectors, all the available PET templates were segmented into 85 VOIs with the DK atlas (44) and region-wise average BPnd values were calculated. A sample of PET axial slices used in the study is presented in Figure 5.

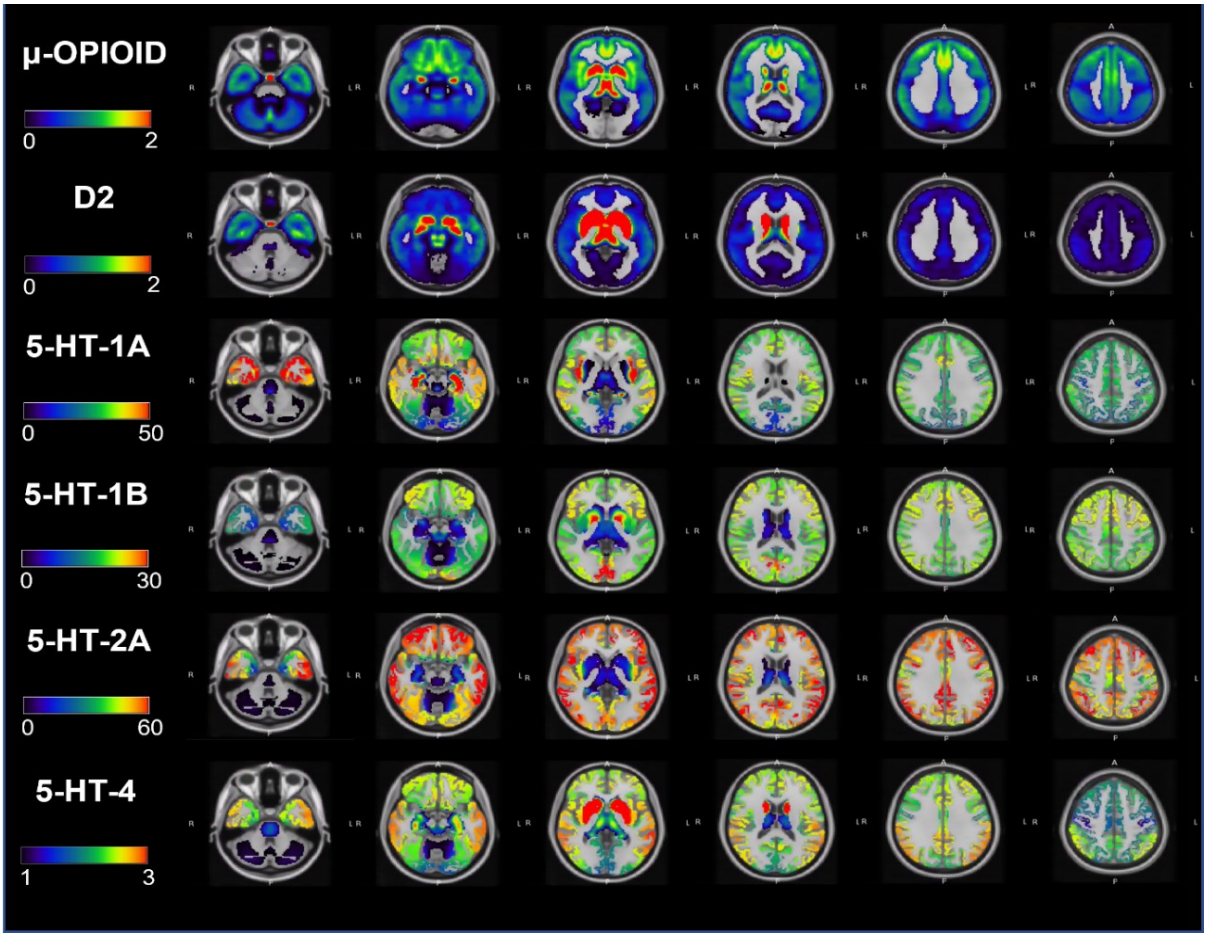

Figure 5: A sample of axial slices presenting receptor BPnd PET maps (bottom six rows) that were used in the linear correlation analysis. All maps are presented after White Matter masking out, and prior to applying any normalization or log-transformation.

mRNA expression profiles

Brain transcriptome profiles were obtained from the Allen Brain Atlas (https://human.brain-map.org/), an open access, multimodal atlas integrating anatomic and genomic information of the human brain (27) that can serve as a reference standard to explore relationships between gene expressions and in vivo functional imaging data (49). ABA comprises microarray-based mRNA expression values sampled over post-mortem brain tissue from 5 males and 1 female donors between 18 and 68 years of age, with no known neuropsychiatric or neuropathological history. The anatomical sites of tissue sample acquisition are projected on a high-resolution brain template in MNI coordinates that facilitates integration with the imaging data.

Current analysis has focused on the mRNA expressions of thirty-four neurotransmitter receptor subtypes for investigating the potential relationship with ΔCBF changes in a data-driven approach, i.e. μ-, κ-, δ- opioids; dopamine D1-D5; adrenaline α1 -A, -B, -D; adrenaline α2 -A, -B, -C; adrenaline β1, β2, β3; serotonin 5-HT -1A, -1B, -1D, -1E, -1F, -2A, -2B, -2C, -3A, -3B, -3C, -3D, -3E, -4, -5A, -6, -7. For this task the MATLAB toolbox: Multimodal Environment for Neuroimaging and Genomic Analysis (MENGA) (http://www.nitrc.org/projects/menga/), which allows integration of ABA and imaging data, was utilized (50).

Since the between-donors gene expression values are highly heterogeneous and tissue sampling generates variability, with the potential to compromise spatial correlations, we have focused our analysis on the left hemisphere only, for which there were more specimens available in ABA. In addition, the imaging and genomic data may present substantial spatial heterogeneity within anatomical regions of interest. While for MRI and PET data a continuous set of voxels is available, that enables averaging among a sufficient number of voxels values to obtain a representative mean per region, in case of ABA the tissue samples are provided in discrete locations within brain tissue. Similarly, the MENGA software utilized here for the imaging-transcriptomic correlation analysis, performs a discrete resampling of CBF to match

the exact anatomical locations of tissue sampling. Accordingly, efficient quantification of CBF and mRNA expressions is required to perform the correlation analysis; larger VOIs are needed, particularly for cortical regions, to obtain sufficient data per region to compensate for this inherent spatial heterogeneity. Thus, both ΔCBF contrast maps and ABA mRNA samples have been grouped over fifteen coarse ABA regions. These include a combination of cortical and subcortical VOIs, comprised of whole volume delineations of frontal, temporal, parietal and occipital lobes, as well as the brainstem, amygdala, thalamus, hippocampus, cerebellum, cingulate gyrus, insula, striatum, globus pallidus, claustrum, and basal forebrain.

Statistical analysis

Paired-samples t-tests and one-sample t-tests were used to assess statistically significant differences of the pain intensity ratings across pain and pain vs pain-free sessions, respectively, for both TME and OA-Controls datasets.

Linear regression models (Pearson correlation) were built in MATLAB 2019b (https://www.mathworks.com/), to correlate ΔCBF responses of TME Pain vs No-Pain and OA vs Pain-free control datasets with regional receptor BPnd distributions (explanatory variables). Initially, the normality of regression residuals' distribution was assessed with Shapiro-Wilk test for normality. In cases of highly skewed distributions, a log-linear transformation was applied. A cut-off value of 10 times the mean Cook's distance was used to exclude extreme observations. Non-parametric Spearman's correlations between ΔCBF profiles and receptor BPnd profiles were also performed. Additionally, a stepwise regression function was used to build multiple linear regression models, while Variance Inflation Factor (VIF), and Variance Decomposition Proportion (VDP), were used as additional diagnostic tools to correct for multicollinearity between BPnd variables, considering thresholds of VIF<3 and VDP<0.9 for Condition Index>30 (51). Bonferroni correction was considered to assess statistical significance (Figure 6).

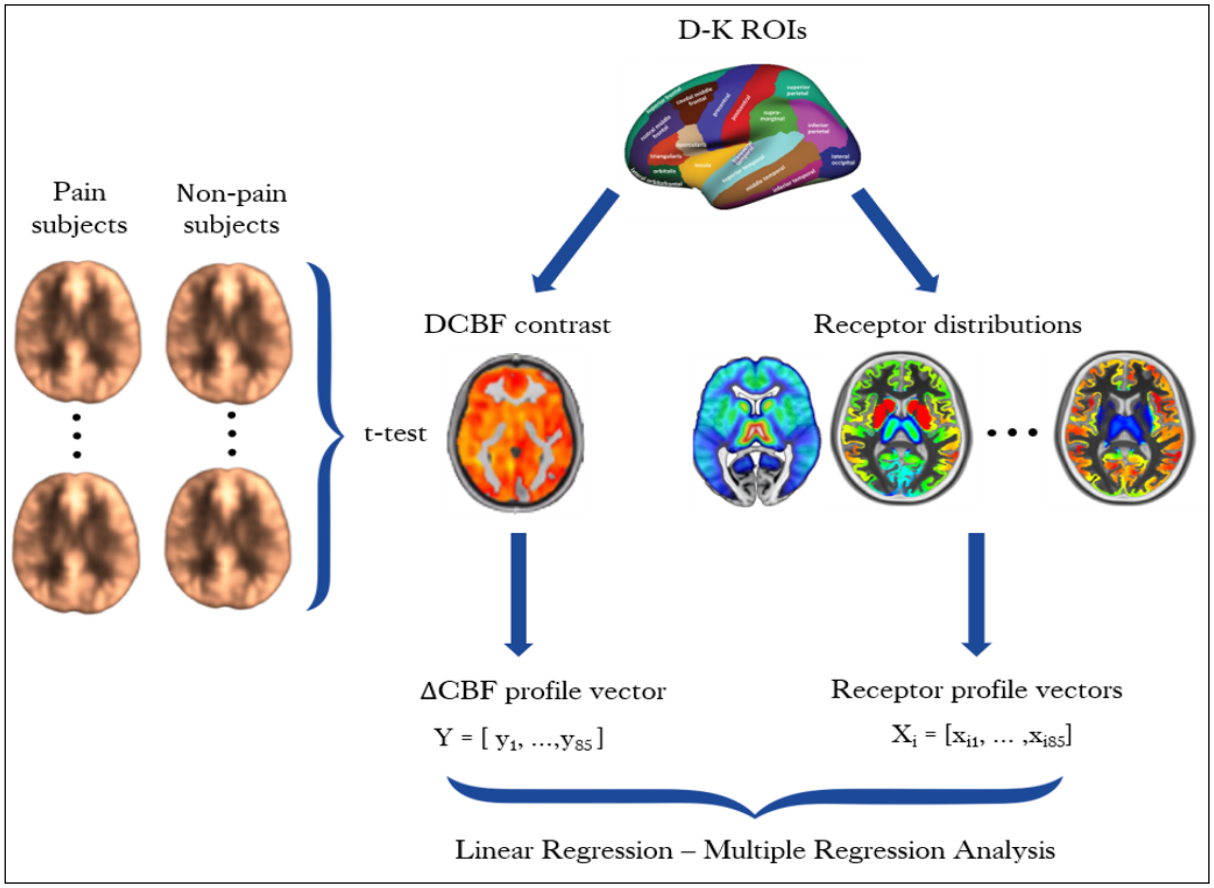

Figure 6: Statistical framework for ΔCBF calculation and correlation with PET templates. PET, positron emission tomography.

The univariate analysis utility in the MENGA toolbox was used for correlating ΔCBF with receptor gene expressions (Figure 7). The univariate cross-correlation analysis consists of the weighted regression of CBF contrast images and mRNA data for each donor. The weights are defined as the ratio of the number of samples in each region over the variability of the image data in that region for each subject. Specifically, the higher the number of samples, the smaller is the expected variability in a VOI. The linear regression results are expressed in terms of squared Pearson's correlation coefficients (R^2), directionality of the correlation (+1 or -1), and the number of times (out of 6 matches) for which MENGA finds a positive or negative correlation (50). The between-donors autocorrelation for both imaging and genomic data is also returned as a metric to assess the consistency of mRNA expressions among donors.

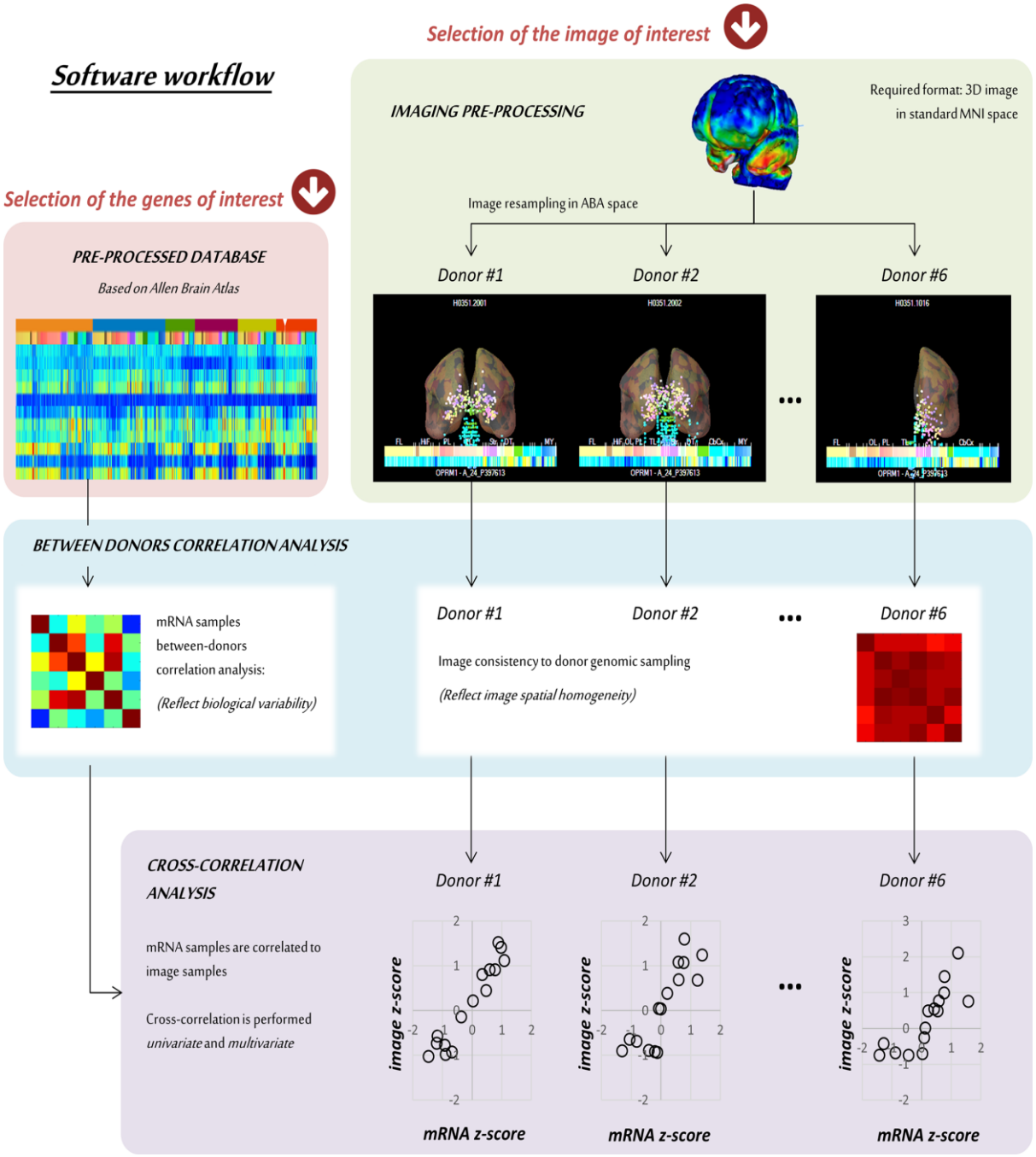

Figure 7: The complete workflow of ΔCBF and transcriptomics correlation analysis. (adopted without changes from (50) Rizzo et al. MENGA: A New Comprehensive Tool for the Integration of Neuroimaging Data and the Allen Human Brain Transcriptome Atlas, PLOS ONE 11(2): 2016, under the terms of the Creative Commons Attribution 4.0 International License http://creativecommons.org/licenses/by/4.0/)

2.1.3 Results

Pain intensity ratings analysis

TME Participants reported significant increases in VAS-derived subjectively reported pain following TME, compared to pain-free pre-surgical sessions (0-100 VAS scores averaged across all pCASL scans: Pre-surgery mean ± SD = 1.67 ± 2.02, Post-surgery = 55.56 ± 15.77, $p<0.001$). Pain intensity VAS scores following extraction of left, compared to right, third molars did not differ ($p = 0.97$) (Figure 8). OA NRS estimates of ongoing pain (mean ± SD = 3.65 ± 2.21) differed significantly compared from controls, that presented zero mean NRS measurement in all scans ($p < 0.001$). We observed NRS scores in the OA group to be significantly higher in session 2 (mean ± SD = 4.15 ± 2.37) than in session 1 (mean ± SD = 3.15 ± 1.92, $p < 0.001$) (Figure 8).

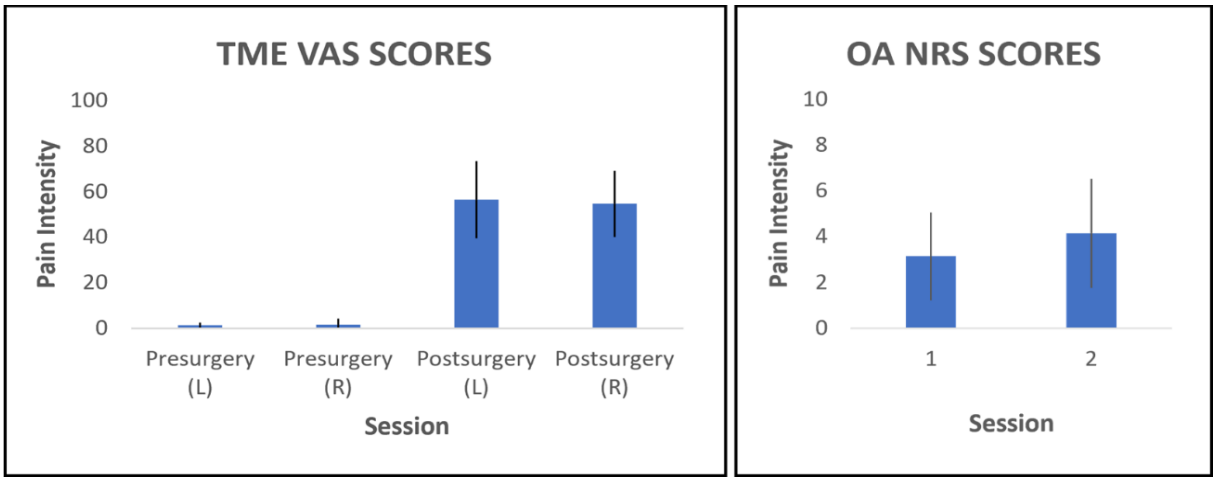

Figure 8: Bar plots showing the mean ± SD pain intensity ratings of all subjects pCASL scans within each session, as indexed by VAS for TME participants (left chart) and NRS for OA patients (right chart). NRS, numerical rating scale; OA, osteoarthritis; TME, third molar extraction; VAS, visual analogue scale

rCBF group level analysis

TME: Group level analysis revealed a distributed network of brain regions with significant increases in rCBF following the extraction of left and right third molars, compared to pain-free pre-surgical scans in the same participants. Regions showing rCBF increases included, but were not limited to thalamus, primary and secondary somatosensory cortices, anterior and posterior insula, anterior cingulate cortex and midbrain. Post-surgical decreases in CBF were not observed, and there were no significant differences of rCBF between cerebral hemispheres, in either pre-surgical or post-surgical scanning sessions following either left or right TME.

OA: A distributed network of brain regions demonstrated local increases in CBF in participants with OA compared to matched controls, largely lateralised to the left hemisphere contralateral to the painful joint. There were no increases in rCBF identified in the control group compared to the OA group.

A sample of cluster-corrected z-score maps showing the abovementioned significant increases in regional CBF along with corresponding DK VOIs are provided in Figure 9. Additionally, the ΔCBF profiles, in terms of average t-scores of all DK VOIs, that were utilized for the spatial correlation with receptor BPnd profiles, are presented Table 1. A sample of axial slices of such ΔCBF maps generated is presented in Figure 10.

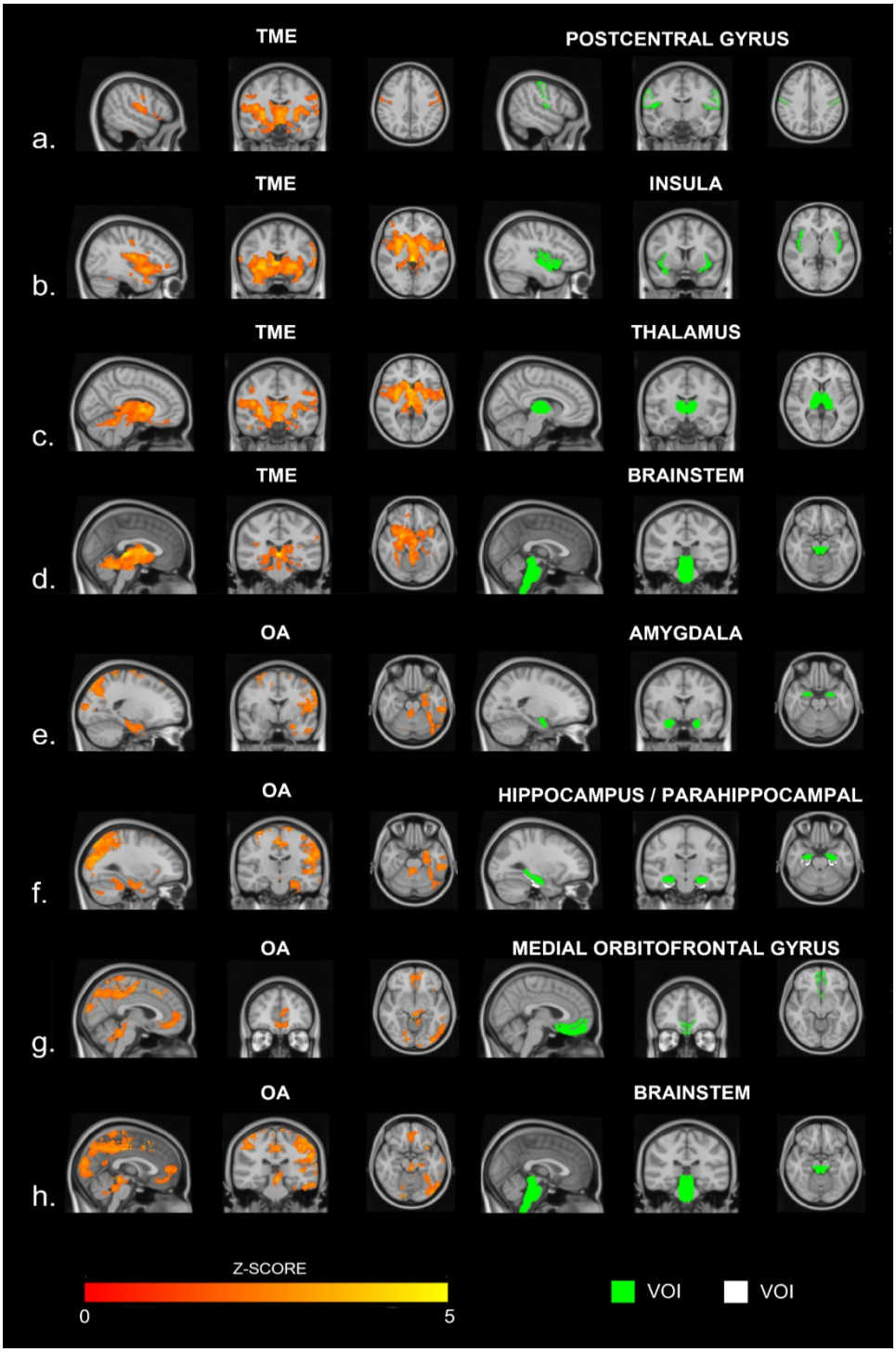

Figure 9: A sample of brain slices in the three planes showing statistically significant increases in CBF of pain compared to non-pain TME, and OA compared to Controls groups, in terms of cluster-corrected Z-score maps (left), along with the corresponding Desikan-Killiany atlas VOIs (green/white) with which they present a significant overlap (right). ΔCBF significant increases of **TME** pain are shown for: (**a.**) Postcentral Gyrus (featuring overlap with primary and secondary Somatosensory cortices); (**b.**) Insula; (**c.**) Thalamus and (**d.**) Brainstem (featuring overlap with Midbrain/Periaqueductal Gray). ΔCBF significant increases of **OA** are shown for: (**e.**) Amygdala; (**f.**) Hippocampus (green) and Parahippocampal Gyrus (white); (**g.**) Medial Orbitofrontal Gyrus and (**h.**) Brainstem (featuring overlap with Midbrain/Periaqueductal Gray).

Table 1: DK VOIs along with corresponding ΔCBF measurements.

No	VOI NAME	POSITION	TME ΔCBF Average T-score	OA ΔCBF Average T-score
1	lh_caudalanteriorcingulate	frontal lobe	3.48	2.73
2	lh_caudalmiddlefrontal	frontal lobe	2.34	1.92
3	lh_cuneus	occipital lobe	2.09	1.27
4	lh_entorhinal	temporal lobe	2.30	2.27
5	lh_fusiform	temporal lobe	1.54	2.17
6	lh_inferiorparietal	parietal lobe	2.07	1.75
7	lh_inferiortemporal	temporal lobe	1.49	2.53
8	lh_isthmuscingulate	frontal lobe	2.69	1.82
9	lh_lateraloccipital	occipital lobe	1.09	1.67
10	lh_lateralorbitofrontal	frontal lobe	1.56	2.74
11	lh_lingual	occipital lobe	1.99	2.02
12	lh_medialorbitofrontal	frontal lobe	3.16	1.76
13	lh_middletemporal	temporal lobe	1.65	2.70
14	lh_parahippocampal	temporal lobe	1.57	2.81
15	lh_paracentral	parietal lobe	2.84	1.43
16	lh_parsopercularis	frontal lobe	2.62	2.36
17	lh_parsorbitalis	frontal lobe	2.14	1.89
18	lh_parstriangularis	frontal lobe	2.09	2.09
19	lh_pericalcarine	occipital lobe	1.91	1.72
20	lh_postcentral	parietal lobe	3.10	1.75
21	lh_posteriorcingulate	parietal lobe	2.84	2.31
22	lh_precentral	frontal lobe	2.75	2.13
23	lh_precuneus	parietal lobe	1.92	0.72
24	lh_rostralanteriorcingulate	frontal lobe	3.89	1.92
25	lh_rostralmiddlefrontal	frontal lobe	2.27	1.60
26	lh_superiorfrontal	Frontal lobe	2.74	1.87
27	lh_superiorparietal	parietal lobe	3.17	0.56
28	lh_superiortemporal	temporal lobe	2.06	2.47
29	lh_supramarginal	parietal lobe	2.77	1.70
30	lh_frontalpole	frontal lobe	1.45	2.21
31	lh_temporalpole	temporal lobe	2.15	2.22
32	lh_transversetemporal	temporal lobe	1.36	2.41
33	lh_insula	frontal lobe	2.69	2.09

34	rh_caudalanteriorcingulate	frontal lobe	2.93	2.92
35	rh_caudalmiddlefrontal	frontal lobe	1.86	1.51
36	rh_cuneus	occipital lobe	1.93	0.64
37	rh_entorhinal	temporal lobe	2.56	0.60
38	rh_fusiform	temporal lobe	1.96	0.97
39	rh_inferiorparietal	parietal lobe	1.74	0.54
40	rh_inferiortemporal	temporal lobe	1.36	1.02
41	rh_isthmuscingulate	frontal lobe	2.17	1.43
42	rh_lateraloccipital	occipital lobe	1.21	0.50
43	rh_lateralorbitofrontal	frontal lobe	2.04	2.79
44	rh_lingual	occipital lobe	1.89	1.12
45	rh_medialorbitofrontal	frontal lobe	2.75	1.66
46	rh_middletemporal	temporal lobe	1.48	1.44
47	rh_parahippocampal	temporal lobe	2.69	1.14
48	rh_paracentral	parietal lobe	2.49	0.59
49	rh_parsopercularis	frontal lobe	2.57	1.27
50	rh_parsorbitalis	frontal lobe	2.18	1.84
51	rh_parstriangularis	frontal lobe	2.40	1.77
52	rh_pericalcarine	occipital lobe	1.91	0.70
53	rh_postcentral	parietal lobe	2.43	0.44
54	rh_posteriorcingulate	parietal lobe	2.22	2.05
55	rh_precentral	frontal lobe	2.25	1.00
56	rh_precuneus	parietal lobe	1.89	0.39
57	rh_rostralanteriorcingulate	frontal lobe	3.41	1.55
58	rh_rostralmiddlefrontal	frontal lobe	2.48	1.61
59	rh_superiorfrontal	frontal lobe	2.78	1.45
60	rh_superiorparietal	parietal lobe	2.86	0.31
61	rh_superiortemporal	temporal lobe	2.02	1.51
62	rh_supramarginal	parietal lobe	1.47	0.19
63	rh_frontalpole	frontal lobe	1.76	2.46
64	rh_temporalpole	temporal lobe	2.96	1.69
65	rh_transversetemporal	temporal lobe	2.25	0.93
66	rh_insula	frontal lobe	3.09	1.45
67	lh_cerebellum	cerebellum	1.64	1.94
68	lh_thalamus	thalamus	2.57	2.84
69	lh_caudate	caudate	3.49	2.70
70	lh_putamen	putamen	3.56	2.40

71	lh_pallidum	pallidum	3.61	2.14
72	brainstem	brainstem	2.44	1.12
73	lh_hippocampus	hippocampus	1.84	2.71
74	lh_amygdala	amygdala	2.40	2.55
75	lh_Accumbens	accumbens	3.42	2.82
76	lh_ventraldiencephalon	thalamus	2.67	2.39
77	rh_cerebellum	cerebellum	2.20	1.09
78	rh_thalamus	thalamus	2.14	1.79
79	rh_caudate	caudate	3.93	2.47
80	rh_putamen	putamen	3.14	2.27
81	rh_pallidum	pallidum	2.42	1.84
82	rh_hippocampus	hippocampus	2.17	1.09
83	rh_amygdala	amygdala	2.80	0.86
84	rh_Accumbens	accumbens	3.47	1.93
85	rh_ventraldiencephalon	thalamus	2.57	1.64

Abbreviations: lh: Left Hemisphere; rh: Right Hemisphere; VOI: Volume of Interest;

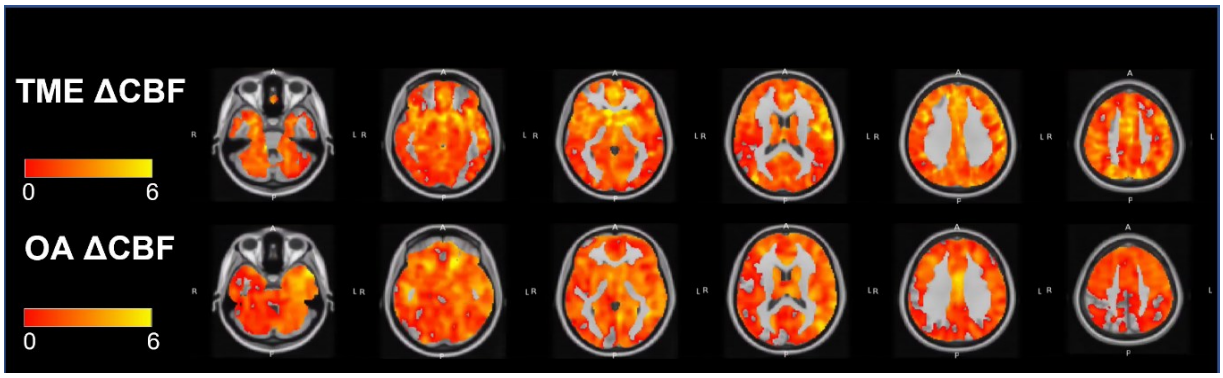

Figure 10: A sample of axial slices presenting the pain vs non-pain for TME, and OA vs Controls ΔCBFs in terms of T-score maps (top two rows). All maps are presented after White Matter masking out.

Linear Correlations

ΔCBF statistically significant correlations (t-test, $p<0.05$) were found with μ-opioid, D2, and 5-HT-2A receptor distributions in the TME dataset. μ-opioid demonstrated the strongest positive association [$R^2=0.35$, Pearson rho=+0.59, Spearman rho=+0.56] followed by D2 [$R^2=0.24$, Pearson rho=+0.49, Spearman rho=+0.33], while a strong negative association was observed for 5-HT-2A [$R^2=0.23$, Pearson rho=-0.48, Spearman rho=-0.51]. Weak negative associations were observed for 5-HT-1A [$R^2=0.05$, Pearson rho=-0.22, Spearman rho=-0.24] and 5-HT-1B [$R^2=0.01$, Pearson rho=-0,11, Spearman rho=-0.19] and a weak positive correlation for 5-HT-4 [$R^2=0.04$, Pearson rho=+0.20, Spearman rho=-0.05]. The results are summarized in Figure 11.

Statistically significant associations ($p<0.05$) were observed between OA vs control rCBF differences and μ-opioid [$R^2=0.20$, Pearson rho=+0.45, Spearman rho=+0.44], D2 [$R^2=0.14$, Pearson rho=+0.38, Spearman rho=+0.39]. R^2 and rho values, were consistently lower in the OA vs control dataset, compared to the TME data analysis. In contrast with TME data, no statistically significant associations with the serotonin maps were found. The results are summarized in Figure 12.

Multiple Linear Correlations

Multiple linear regression models for TME and OA datasets included all receptor templates except for 5-HT-4 that was found redundant. The adjusted R-squared values were $R^2=0.44$ and $R^2=0.16$, for TME and OA respectively. Statistical significance of the regressors was used to evaluate the contributions of each receptor to the multivariate model fits. In TME model the μ-opioid, D2 and 5-HT-2A survived Bonferroni correction ($p=0.05/5=0.01$), exactly replicating results of univariate analysis. In the OA-control model, only the μ-opioid receptor reached significance.

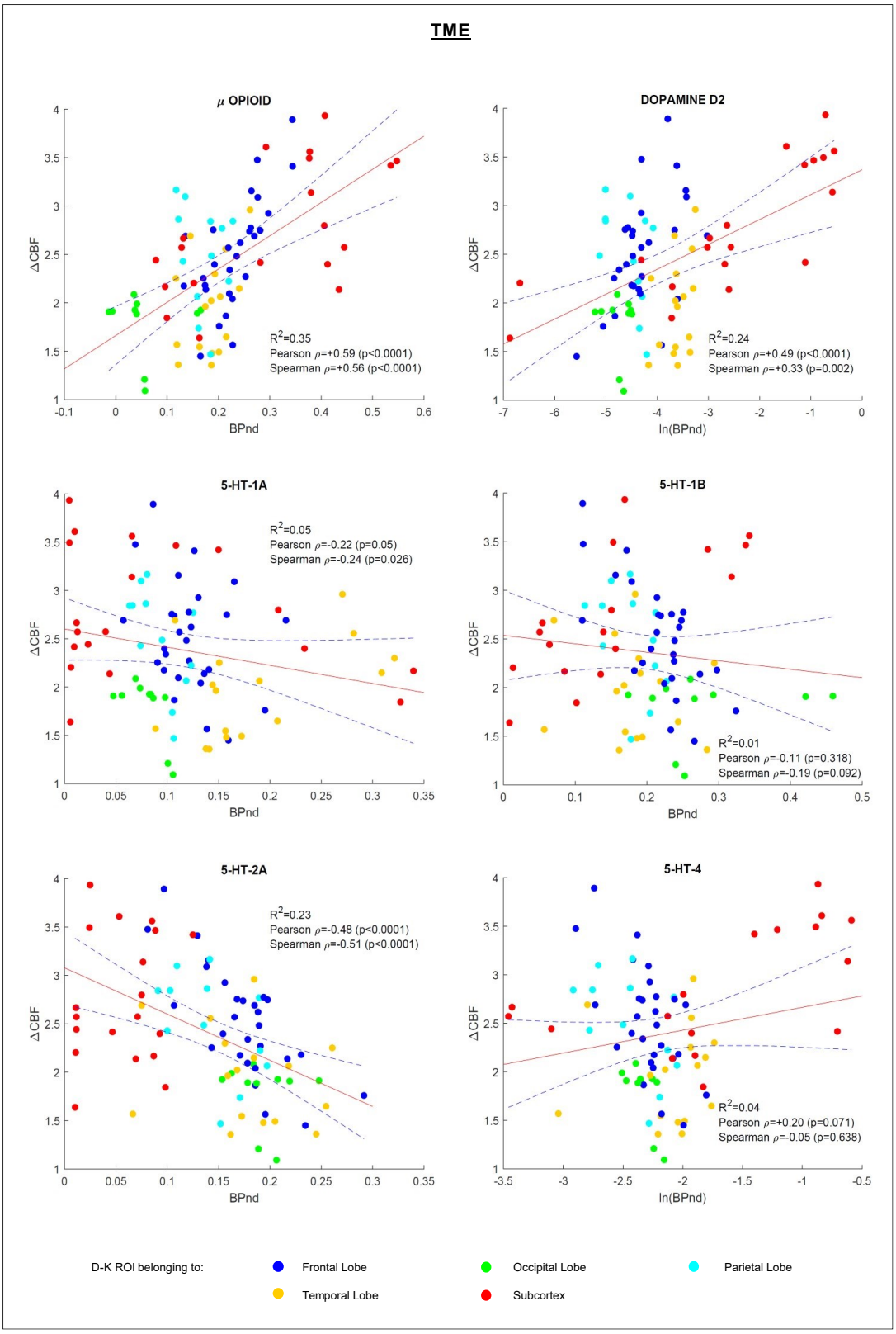

Figure 11: TME study regression plots: Scatterplots of the 85 VOIs (dots) displaying the relationship of the average regional CBF change (ΔCBF) between pain and non-pain states of TME dataset with average regional BPnd values of the six receptor templates utilised. The linear regression curve (red line) and 95% confidence bounds (dashed lines) are shown. The dots are presented color-coded as shown in the figure legend to provide a coarse positioning of the VOIs into the brain. BPnd, binding potential; CBF, cerebral blood flow; TME, third molar extraction; VOI, volumes of interest.

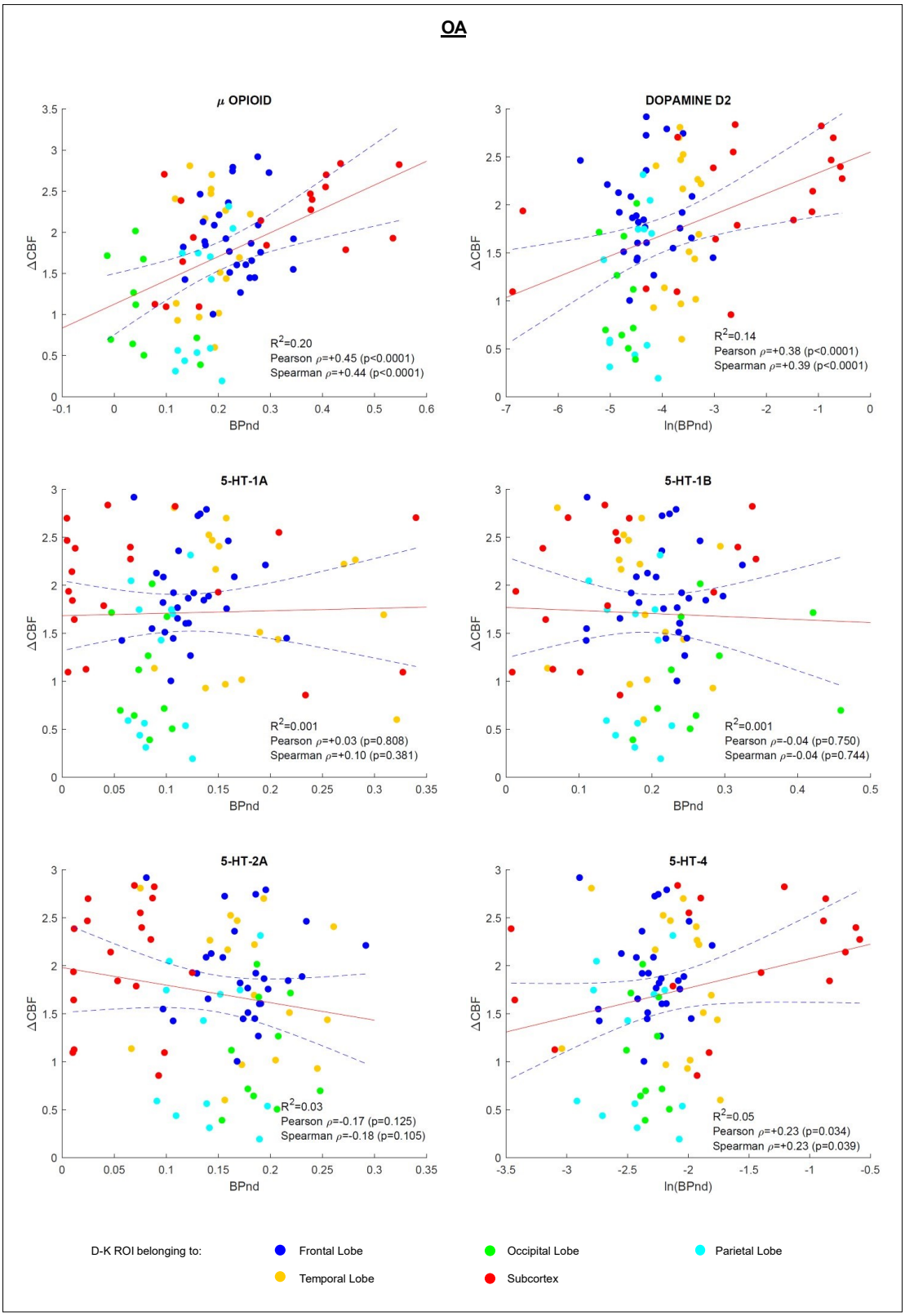

Figure 12: OA regression plots: Scatterplots of the 85 VOIs (dots) displaying the relationship of the average regional CBF change (ΔCBF) between pain and nonpain states of OA and controls datasets with average regional BPnd values of the six receptor templates utilised. The linear regression curve (red line) and 95% confidence bounds (dashed lines) are shown. The dots are presented color-coded as shown in the figure legend to provide a coarse positioning of the VOIs into the brain. BPnd, binding potential; CBF, cerebral blood flow; OA, osteoarthritis; VOI, volumes of interest.

mRNA correlations

Within the genomic-imaging correlation analysis performed in MENGA, only 18 out of 35 genes examined presented a sufficiently high between-donor mRNA expression consistency (auto-correlation values R^2>0.40) to be reported (detailed in Table 2). The directionality of the correlations was found to be consistent in both TME and OA datasets, respectively, however their cross-correlation values with rCBF presented great variability between the two datasets. Statistically significant correlations ($p<0.05$) were observed for OPR-K1 in TME, DR-D2 in OA, ADR-A-2A in OA and 5-HTR-5A in TME and OA.

Table 2: mRNA correlations results

Gene group	Gene	Gene auto-correlation	TME cross-correlation		OA cross-correlation		Direction of correlation
		(R^2)	(R^2)	(p-val)	(R^2)	(p-val)	
Opioid	OPR-M1	0.82	0.11	0.230	0.10	0.245	+1
	OPR-K1	0.72	0.30	0.034 *	0.23	0.070	+1
Dopamine	DR-D1	0.69	0.16	0.140	0.15	0.154	+1
	DR-D2	0.88	0.12	0.207	0.36	0.018 *	+1
	DR-D3	0.44	0.19	0.104	0.04	0.475	+1
	DR-D5	0.44	0.06	0.379	0.10	0.245	-1
Adrenaline	ADR-A-1A	0.45	0.16	0.140	0.05	0.431	+1
	ADR-A-1B	0.94	0.02	0.619	0.19	0.104	-1
	ADR-A-2A	0.78	0.13	0.188	0.31	0.029 *	+1
	ADR-A-2C	0.89	0.08	0.307	0.06	0.379	+1
	ADR-B-2	0.54	0.17	0.129	0.21	0.086	+1
Serotonin	5-HTR-1A	0.90	0.05	0.431	0.19	0.104	-1
	5-HTR-1E	0.82	0.06	0.379	0.08	0.307	-1
	5-HTR-2C	0.90	0.23	0.070	0.09	0.277	+1
	5-HTR-3B	0.48	0.19	0.104	0.19	0.104	-1
	5-HTR-5A	0.60	0.27	0.047 *	0.30	0.034 *	-1
	5-HT-4	0.73	0.07	0.340	0.09	0.277	+1
	5-HTR-7	0.80	0.26	0.058	0.13	0.188	+1

* *Statistically significant correlations*

2.1.4 Discussion

The present study demonstrates relationships between ASL-derived rCBF indices of ongoing pain and specific receptor spatial distribution profiles obtained from PET and mRNA data within neurotransmitter systems relevant to clinical pain. Moderate to strongly significant correlations were observed between ΔCBF and both mu-opioid and D2, while weak positive and negative correlations for the 5-HT receptors' BPnd distributions were identified in both spontaneous (TME) and persistent (OA) pain models. Only the 5-HT-2A receptor showed a significant negative correlation with ΔCBF in TME. We observed stronger μ-opioid and D2 receptor correlations with ΔCBF in the TME, compared to the OA dataset. Multiple linear regression models were found to largely replicate the univariate analysis results, but additional weaker effects of the receptors on ΔCBF were not observed in these models. The significant relationships found between receptor mRNA expressions and ΔCBF were relevant to the receptors' expected functions in pain processing, but correlation coefficient values varied between datasets and corresponding results of ΔCBF and PET templates analysis. This study provides important new evidence regarding the link between pain-related, ASL-derived rCBF signals with the opioidergic and dopaminergic systems, two crucial components of pain processing (38). Beyond acting as 'proof of concept', these findings help inform future investigation of the molecular mechanisms underlying painful experiences, namely neurotransmitter systems, which may show functionally relevant disruption in acute and chronic pain conditions, as well as modulation by treatment.

Several major differences were immediately apparent between the TME-pain and OA datasets. Mechanistic insights from each study have been described previously (see (30,41)) but are briefly summarised here. Perhaps most notably, in the TME data, a remarkably symmetric distribution of increases in rCBF following removal of both left and right teeth was observed. By contrast, rCBF increases in OA participants were markedly lateralised, predominantly located in the left hemisphere contralateral to the painful thumb. Laterality issues aside, there

were many similarities between the two datasets, namely, a distributed network of increases in rCBF only in brain regions commonly associated with the pain experience, including primary and secondary somatosensory, anterior and poster insula and anterior cingulate cortices, thalamus, and midbrain (including the Periaqueductal Gray (PAG)). rCBF increases in several of these regions have also been reported in other chronic pain cohorts, for example Chronic Low Back Pain (CLBP) (37). Quantitative comparisons between datasets were not performed here, given so many phenotypic differences between TME and OA datasets respectively, including pain phenotype (acute post-surgical vs persistent pain); body site (bilateral dentition vs unilateral hand); age (young vs older adults); sex (male vs female); experimental design (within vs between subject). Often it is considered more straightforward to study experimentally induced pain in healthy volunteer participants, compared to patients with chronic pain. The latter are a comparatively more heterogeneous cohort, with defining characteristics not only in terms of behaviour (inescapable, ongoing daily pain, psychological sequelae including anxiety and depression; medication use, etc), but also brain structure (52) and brain function (36). In view of producing transiently inescapable ongoing post-surgical pain, we and others have argued in favour of the TME model being an excellent 'half-way house' between acute and chronic pain states (53). The reader is referred to the recent review of (15) which provides a thorough summary of reports of rCBF changes relating to acute and chronic pain states. However, what is important in this proof-of-concept study is the demonstration of a relationship between the spatial distribution of neurotransmitter receptor densities, and changes in rCBF associated with individuals' pain experiences, both experimentally induced and chronic.

We acknowledge that the techniques employed here have some limitations. Spatial autocorrelation - i.e., statistical dependence between neighbouring voxels/regions - is inherent within brain maps that might increase the Type I error of common statistical inference frameworks. While some spatial permutation methods exist for generating spatially null models for brain maps (for a complete review see (54)), none of them are suitable for applying spatial

shuffling across both hemispheres and both cortical and subcortical areas in the same model. This intrinsic limitation is due to the requirement for different distance calculation methods between corresponding parcels, thus constraining the utility of current approaches for whole brain correlation analyses. Our consideration of transcriptomic data provides additional challenges to any approach to this problem. We consider that the development of appropriate methodologies to mitigate spatial autocorrelation issues as an important future challenge for the field.

Our method exploits the availability of normative receptor templates, but it should be acknowledged that these data do not account for potential pathologic or neuroplastic changes that may be induced by chronic pain conditions, or possible effects of long-term medication use on receptor expression profiles. In an ideal world, to maximise interpretability and validity of results, studies would make use of subject-specific PET scans to provide precise quantification of receptor binding and directly addressing the underlying neurochemical conditions. However, broad consideration of multiple neurotransmitter systems would be financially punitive, not least largely impossible to implement given both the cost and safety limitations on repeated administration of radiotracers. The benefit of the current technique is that it can leverage existing datasets and provide insights when more expensive and complex techniques have yet to, or cannot, be employed. As such, the current approach offers significant utility as a low-risk hypothesis generating tool at a relatively low cost.

The most important finding of our study was the significant correlation of ΔCBF with the μ-opioid receptor profile. Arguably, this validates the techniques employed here; the μ-opioid receptor plays a well-established pivotal role in pain processing (55). Increased neural activity in opioid-rich descending pain modulatory structures such as the rostral anterior cingulate cortex, amygdala, and PAG has been reported during placebo interventions (56). In a previous study, placebo responders that received the opiate antagonist naloxone under blinded conditions indicated pain levels similar to those of the non-responders, indicating that the mechanism of

placebo analgesia engaged required engagement of endogenous opioid-mediated systems (31). Moreover, opioid analgesics including morphine, methadone, fentanyl, and oxycodone are a cornerstone in the pharmacotherapy for pain and act primarily upon the μ-opioid receptors (MOR) (57). The strong association between ΔCBF and μ-opioid receptor particularly observed in the TME dataset is in accordance with previous preclinical (58) and clinical (39,40) PET/fMRI studies of acute pain conducted with the μ-opioid selective radiotracer [11C]carfentanil, further adding credence to the ability of the techniques employed here to capture meaningful molecular relationships. Given its sensitivity to detect low-frequency signal fluctuations, ASL has the potential characteristics to be developed as a biomarker to probe opioidergic systems, both in patient/control designs as well as 'within-subject' experimental conditions, for example, drug/placebo comparisons.

Associations between ΔCBF and μ-opioid in the OA group were weaker than those identified in the TME cohort. Although this may partially be attributed to the increased heterogeneity between OA and healthy control groups utilized in the specific model design, however the contradictory reports regarding the role of mu-opioid receptor in mediating analgesia within chronic pain conditions remains highly equivocal (59). For example, two previous studies found that administration of naloxone did not block placebo effects in patients with chronic pain, suggesting that the endogenous opioid system functions differently under conditions of chronic pain (56). Similarly, recent reports suggest that mechanisms in addition to the opioidergic system are also important in mediating placebo responses more generally (60). Chronic pain is associated with structural and functional changes in the central nervous system that affect multiple brain structures involved in pain perception and modulation. Recent MRI and PET studies have provided insights into the maladaptive neuroplasticity related to chronic pain, such as the reduced μ-opioid receptor availability in chronic pain disorders including rheumatoid arthritis and neuropathic pain (38). Furthermore, a previous study has shown increased levels of endogenous opioids in the cerebrospinal fluid of fibromyalgia

patients, an indirect index of reduced μ-opioid receptor availability, which may hold some explanatory value for the poor efficacy of opioids in fibromyalgia (61). Potentially, altered opioid neurotransmission in our OA patients might have affected the association of μ-opioid receptor density with ΔCBF, illustrating a limitation when using normative receptor templates, as previously described.

We also sought to investigate potential monoaminergic associations with rCBF. Monoamines regulate the endogenous pain system (62), and both peripheral and central monoaminergic dysfunction has been reported in various pain aetiologies (63). Currently monoaminergic pharmacotherapies do not constitute a first line choice for chronic pain (e.g., in osteoarthritis) (64). However, recently drugs like duloxetine have been repurposed from other neuropsychiatric conditions and are used for neuropathic pain and fibromyalgia. Such drugs are thought to impart analgesic efficacy through inhibiting the reuptake of monoamines in brain and spinal levels (63).

Dopamine's central circuitry has an important role in pain processing, while among the five subtypes of dopamine receptors (D1-D5) in the CNS, the D1 and D2 are those most strongly implicated in pain modulation within animal models (63). Activation of D2/D3 receptors at the spinal level induces an anti-nociceptive effect, whereas stimulation of D1/D5 receptors is pro-nociceptive (63). Early evidence from human PET imaging studies have shown a strong correlation of striatal D2 receptor availability with individual variations in subjective ratings of sensory and affective qualities of persistent pain (65) in fibromyalgia (66). In our study a statistically significant correlation was observed between ΔCBF and the D2 receptor in both datasets, while the D2 association follows a similar trend with μ-opioid. Although this finding is important, however a straightforward interpretation is difficult; strong co-localization of μ-opioid and D2 receptor distributions exists, and this kind of analysis has an intrinsic limitation in differentiating between co-founding effects. In other words, we cannot be sure of

the extent to which the result reflects a direct D2 receptor involvement, or a mixed effect of interactions between the opioid and dopamine systems.

We suggest that future studies should take into account these considerations and previous evidence, and particularly utilize PET/fMRI to shed further light on the opioid–dopamine system, which has been shown to play an important role in endogenous analgesia and placebo effects (58). Specifically, as most striatal neurons express both opioid and dopamine D2/D3 receptors, it is thought that dopamine produces analgesic effects via interactions with endogenous opioids in midbrain areas (62). A recent study exploiting 7T fMRI has shown evidence that placebo is likely mediated by the lateral PAG, an area that produces a non-opiate mediated analgesia upon stimulation (60). Generally, PAG that is an essential element of the descending pain modulatory system (38), has a dense concentration of mu-opioid receptors but also contains a subpopulation of dopaminergic neurons that, if ablated or antagonized, attenuates the antinociceptive effects of systemic morphine. On the other hand, dopamine receptor agonists and dopamine transport inhibitors enhance the antinociceptive effects of opioids (67). Other analgesics (e.g., gabapentinoids) that were used in combination with those having a direct effect on monoaminergic system, have been reported to alleviate certain types of chronic pain (28,63). Therefore, combined therapies that modulate multiple neurotransmitter systems may offer stronger therapeutic benefit than that of systemic analgesics.

Serotonin (5-hydroxytryptamine, 5-HT) is a monoamine widely distributed both at the periphery and in the central nervous system. Although the peripheral pronociceptive role of 5-HT is well established, its modulatory role at the spinal and supraspinal levels seems highly variable, depending on the type of receptor, the neural structure and pathophysiological condition, emphasizing the complexity of its implications for the neurobiological mechanisms underlying nociception (68).

In general, there are very few in vivo human PET studies quantifying 5-HT receptor subtypes due to the lack of selective radioligands or sparsity of receptors in the brain (69).

Among the few existing 5-HT receptor PET templates that were used in this study, only the 5-HT-2A showed a moderate, but inverse association with the ΔCBF profile, particularly in the TME dataset. In a previous PET study, the 5-HT-2A receptor availability in the brain, and specifically in regions involved in cognitive and affective functions, was found to co-vary strongly with the responses to long-lasting (tonic) heat pain stimulus (70). The authors suggested that 5-HT-2A has a role in pain processing but is more related with the cognitive and emotional assessment of painful stimuli rather than its implication in antinociception. We speculate that these pain excitatory effects of 5-HT-2A are illustrated here by the negative nature of the correlation in the TME post-surgical pain dataset.

A previous PET study that correlated responses to the cold pressor test with 5-HT-1A receptor binding in the brain found 5-HT-1A receptors to be involved in regulation of pain-related responses (71). However, the association between pain intensity and 5-HT-1A BPnd was also present in brain regions not conventionally associated with pain processing, possibly indicating an indirect serotoninergic effect on behavioural responses rather than a specific pain modulatory action (71). These findings were further validated by the same authors in a newer study (72) and could explain the insignificant relationship of ΔCBF and 5-HT-1A distributions observed in our whole-brain analysis.

A significant correlation of 5-HT-1B and 5-HT-4 with hemodynamic responses was not observed here and there are no reports from human imaging studies addressing the role of the specific 5-HT receptors in pain that could help us elucidate these findings. In general, the 5-HT-1B/D receptors are thought to have similar action in pain processing with the 5-HT-1A receptors, because of their homologous structure (73). Preclinical studies comparing agonists and antagonists for 5-HT receptor subtypes, found a significant antinociceptive role for supraspinal 5-HT-4 and 5-HT-7 receptors in visceral and neuropathic pain models (73). This highlights the potential importance of these receptors in pain inhibition, which requires further investigation.

We also exploited gene expression profiles from the ABA microarray data to obtain information about receptors' spatial distributions by means of mRNA availability. In general, the directionality of the relationships between receptor expression and ΔCBF, are consistent with our ASL/PET analyses, however direct comparisons of the magnitudes of the associations between methods would be arbitrary due to their different implementations. Of note, besides the small sample size underpinning ABA and interindividual differences between donors, mRNA expressions only approximate cellular protein levels due to post-transcriptional regulatory mechanisms (50). That said, the directionality of the ΔCBF associations with both PET and mRNA templates accords with the expected functions of supraspinal receptors in pain processing. This is perhaps best illustrated here by the positive correlation of the receptors that exert inhibitory effects (e.g., μ-opioid, D2/D3, ADR-A-2A/C, 5-HT-7) and the negative/weak correlation for receptors that are thought to facilitate pain signals or are more associated with behavioural and emotional aspects of the pain experience (e.g., D5, 5-HTR-1A/B, 5-HTR-2A, 5-HTR-3B) (12). More importantly, considerations regarding directionality relate to existing literature that has directly investigated receptor-specific PET and hemodynamic measures at a mechanistic level, further adding credence to the ability of the techniques employed here to capture meaningful molecular relationships (2). However, it should be noted that an inverse relationship between the signs of the observed inhibitory and excitatory functional responses should be expected when comparing the two methodologies. This is because the previous studies that have made use of simultaneous or sequential PET-MRI address the functional responses through the dynamic measurement of BPnd decrease, i.e., loss of receptors' availability, as an indicator of neuronal activation. In contrast, the method implemented here assumes the magnitude of neurotransmitter activity to be proportional with receptor's spatial distribution and availability across brain regions, as indexed by the static PET templates or the transcriptomic data utilized.

Further statistically significant correlations with ΔCBF were observed for mRNA indices of kappa-opioid and adra-A-2A receptors, implying a potential supplementary role in pain modulation. Though the MOR is the main target for opioid analgesics, the δ- (DOR) and κ- (KOR) opioid receptors have recently gained attention as potential targets for pain and analgesia regulation (74). The relative affinities of opioid analgesics for these receptors confer unique properties relating to mood and stress reactivity (74). Specifically, while MOR agonists produce euphoria and promote stress coping, KOR agonists produce dysphoria, stress-like responses and negative affect, whilst agonists at DOR reduce anxiety and promote positive affect. Our findings indicate functional significance of KORs in ongoing pain and adds credence to attempts to understand how best to pharmacologically modulate the multiplicity of opioid receptors to maximise clinical utility whilst minimising adverse effects (74). Recent evidence has also demonstrated adrenergic analgesic effects imposed by pharmacologic stimulation of cortical a2A adrenoceptors in animals (75). Overall, we consider this initial evidence important as several gene candidates could play an important role for understanding neuron structural and functional alterations apparent in persistent pain conditions and serve for the development of individualised pain therapies (76,77).

2.1.5 Conclusion

In conclusion, we provide a novel demonstration of the relationship between ongoing pain, as informed from ASL based rCBF, and a priori understanding of molecular receptor density profiles. Strong relationships were found for the μ-opioid receptor and dopamine D2 receptor, further supporting the primacy of these neurotransmitter systems in pain processing. The methodology deployed here is a useful tool to help bridge the translational gap between the advancing knowledge gained from MRI and the neurotransmitter systems that underlie these findings. Specifically, understanding the neurotransmitter systems engaged during pain,

perturbed in chronic pain, and modulated under analgesic intervention are crucial steps to producing evidence-based precision medicine and development of novel analgesic pharmacotherapeutics.

this page intentionally left blank

PART B

Oncologic Imaging Applications

this page intentionally left blank

Chapter 3

3.1 Background

Cancer is a highly heterogeneous disease, in terms of aetiology, prognosis, and response to therapy, while the (epi)genetic properties of the individual cancer cells are highly variable (4). Especially malignant tumors present biological complexity which appears across several tumor subtypes that exhibit substantial variation in gene expression, biochemistry, histopathology, and macroscopic structure (78). Beyond clonal evolution from single progenitors into more aggressive variants, cancerous cells also present branched evolution. This biologic heterogeneity, which is also constantly prone to various environmental stressors, leads to various temporal and regional differences (e.g., regarding stromal architecture oxygen consumption, glucose metabolism, protein, and growth factor expression). As a result, cancerous tumors' progression takes place over spatially distinct patterns of blood flow, vessel permeability, cell proliferation, cell death and other features (78). The spatial and temporal heterogeneity observed between individual patients (inter-tumor heterogeneity) and/or within each lesion (intratumor heterogeneity), as a consequence of the genetic diversity of the mutations-derived subpopulations (78), can lead to the failure of targeted therapies, even with validated targets and drugs, as resistant clones survive and multiply (79).

Nowadays, the personalized approach to medical care is based on the large-scale data synthesis from various sources, such as the new generation molecular biology "-omics" tools (e.g., Genomics (Deoxyribo-Nucleic Acid (DNA)), Proteomics (Proteins), Metabolomics (Metabolites), Transcriptomics (RNA), etc), as well as other factors (heredity, lifestyle), so that

a holistic description of the pathology of each patient is created. The ultimate goal of this process is to classify patients into subgroups with common biological characteristics (e.g., expression of specific genes or predicted response to treatment), as long as different population groups may present different susceptibility to disease, and require more specialized diagnostic, prognostic and therapeutic approaches. Especially in cancerous tumors, the very important contribution of the above technologies, which aim at characterizing the biological heterogeneity of the lesions, by identifying the molecular phenotypes of the mutations of the disease, is already evident (80). However, cancerous tumors' biological heterogeneity is prone to underestimation when based on the standard histopathology examination, as this considers sparce tissue samples, hence present limitations in mapping the biological variations within the whole tumor (81). Additionally, biopsy-based tissue sampling is an invasive procedure that is highly prone to appearance of adverse effects or might even be contraindicated for some patients and cancers. Consequently, these limitations narrow down further its utility for monitoring cancer progression over time.

Nevertheless, it must be noted that novel biopsy methods offering unique opportunities to address the afore-mentioned limitations are currently evaluated and gradually being adapted in the clinical practice. Whole-mount histology can examine greater volumes of tissue to assess tumor profile, however, this technique applies mostly after radical tumor excisions (e.g., prostatectomy), and it is not ideal for assessing tumors of intermediate risk (82). Liquid biopsy has brought significant advancement in monitoring dynamics of various types of primary and metastatic tumors, by detecting cancer cells or corresponding DNA fragments in blood circulation. Even though this method is non-invasive and thus can be applied repeatedly to facilitate early detection and monitor response to treatment, however it has a number of disadvantages; Liquid biopsy is generally fragile and requires extremely sensitive and specific methods that are presently in low availability and accompanied by several technical constraints, so it is still lacking clinical validation. Additionally, tumour heterogeneity may not be totally

captured when considering small quantities of related cells, thus it is highly prone to false-negative results, not to mention that it lacks any spatial information regarding tumor sites (83).

Medical imaging has become one of the most important factors in medical science that contributes to the assessment of a variety of pathological conditions. In terms of personalized cancer treatment modern clinical imaging can provide a more comprehensive characterization of tumor biological heterogeneity, by means of exploiting a variety of phenotypic features (e.g., tumor density, pattern of enhancement, cellular composition, regularity of tumor margins, and affection of the surrounding or distant tissues) (4) (Figure 13). More importantly, the exploitation of advance tomographic imaging together with the largely non-invasive nature and the widespread availability of the respective techniques, enables tumor profiling and progression monitoring in a continuous spatial and temporal basis. In turn, the well validated macroscopic imaging biomarkers outputs are utilized throughout the cancer management procedures, i.e., guidance of diagnosis, staging and planning interventions, monitoring of therapeutic approaches, prediction of treatment response, and outcomes determinations (84). The clinical management breast cancer constitutes a characteristic example of the substantial contribution of medical imaging, as the 5-year survival rates have improved tremendously since the 1980s, mainly because of the significant uptake of conventional and advanced mammographic screening, that have facilitated early detection and risk stratification, along with the improvements in targeted treatments (4).

Particularly MRI has emerged as the spearhead for screening soft tissue cancers presenting high suspicion for malignancy and has provided substantial improvements in tumor detection and characterization. MRI generates high-resolution/high-contrast images that can provide a definite differentiation of tumor margins and peripheral organs anatomy, while it is suitable for identifying tumor infiltrative components and associated edematogeneous regions in the surrounding tissues, as well as for the simultaneous assessment of nearby nodal status, and presence of local or distant metastasis. The addition of advanced MRI techniques to the

conventional structural MRI, such as DWI, DCE, and MR Spectroscopic imaging provide significant structural, functional, and metabolic information in the microscopic and cellular levels, highlighting multifaceted aspects of the underlying pathophysiology (Figure 13), and have increased the capabilities of the non-invasive evaluation of cancer pathology status, aggressiveness, and response to treatment.

Despite the indisputable contribution of MRI and other advanced imaging modalities in narrowing down the biopsy-based challenges in cancer management, existing limitations partially degrade their predominant role and clinical implementation. Traditional radiological evaluation relies largely upon qualitative features, while parts of detailed gray tones

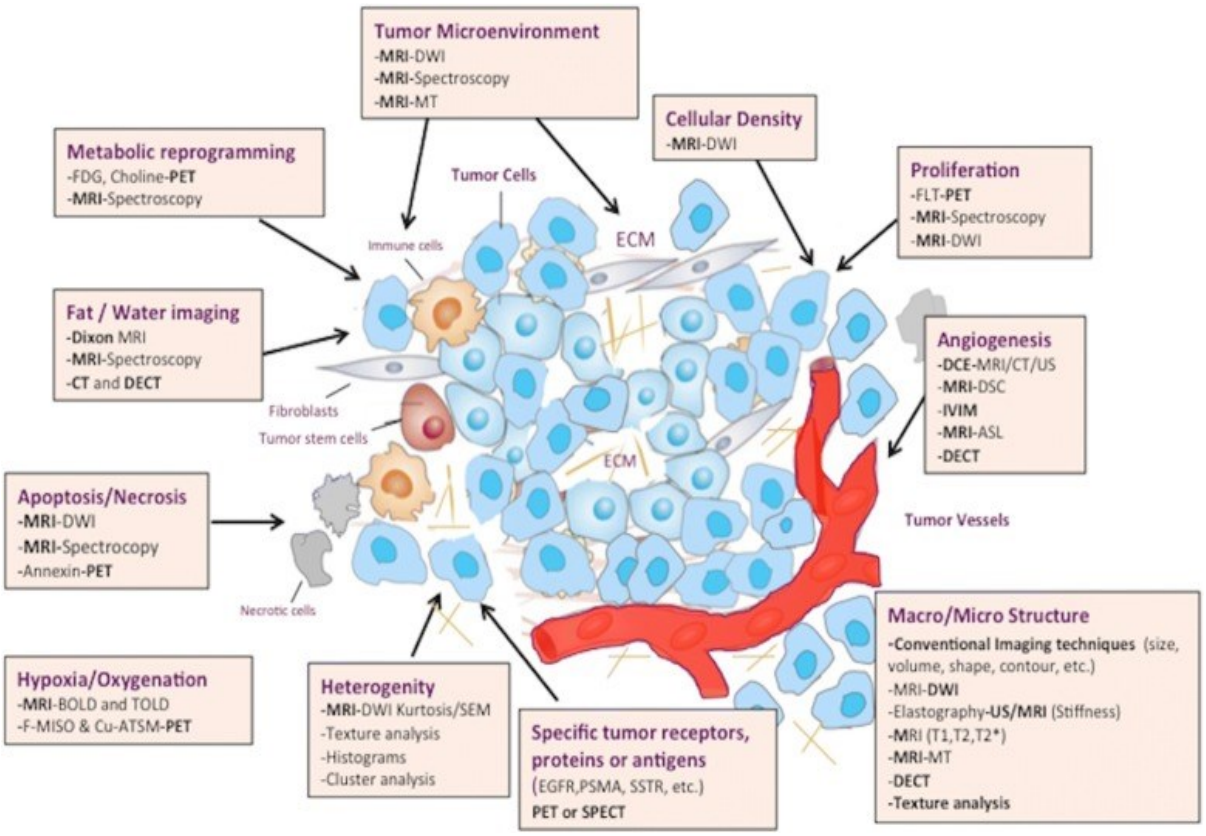

Figure 13: Main imaging techniques in the evaluation of tumor biology and microenvinroment (adopted without changes from (85) García-Figueiras, R., Baleato-González, S., Padhani, A. R., Luna-Alcalá, A., Vallejo-Casas, J. A., Sala, E., Vilanova, J. C., Koh, D. M., Herranz-Carnero, M., & Vargas, H. A. (2019), How clinical imaging can assess cancer biology, Insights into imaging, 10(1), 28, under the terms of the Creative Commons Attribution 4.0 International License http://creativecommons.org/licenses/by/4.0/)

patterns that may reflect important biological underlying information may not be easily perceived by the human eye. Additionally, tumor biological processes may be closely correlated, and their accurate interpretation is not always straightforward, especially when phenotypic similarities exist between pathologies, e.g., pathologies mimicking tumors, heterogeneous lesions presenting overlapping or even identical imaging characteristics, often coexisting with contradictory clinical evidence from other sources (6).

At this point it should be also mentioned that the endogenous complexity of the physical principles exploited by the sophisticated imaging protocols, that are largely extending beyond the traditional training of the radiologists, along with the vast amounts of numerical data produced may pose more of a problem rather than a solution to the many of the afore-mentioned differential diagnostic dilemmas. Consequently, the collection and rational exploitation of the abundance of these important quantitative metrics, often leads to high inter-reader variability in interpretation and adherence to qualitative reporting paradigms.

The adoption of Imaging Reporting and Data System lexicons in various cancers imaging protocols, e.g., breast cancer (BI-RADS), prostate cancer (PI-RADS), that were established to standardize the inter-institutional imaging data collection and assessment, have fairly improved the overall diagnostic benefit. However, these lexicons mainly rely upon subjective evaluation of imaging findings, with very few incorporated quantitative features, such as lesion size, volume, length and functional and/or metabolic measures that may hold a prognostic value or provide an estimated risk of malignancy. As a result, lots of numerical information which may hold diagnostic potential remains unexploited, not to mention that the reported inter-observer agreement has only been moderate to good according to several multi-reader studies (86).

Tracing their routes to the early 60s' and 70's and following that time advances in computational technology an ever-increasing interest from the research community the past decades has been focus on incorporating computers' power and image processing and analyses methodologies in the assessment of medical images. These approaches were motivated by the

fundamental principle that the macroscopic imaging phenotypic characteristics were evidently reflecting tumor biological processes present in the histological and molecular levels, while the initial efforts intended to aid the unravelling of the 'hidden' information into the images, that is difficult to be captured by the human eye (84). In this context various computational methodologies of significant utility, termed Texture Analysis, were developed.

The objective of texture analysis is to quantify the numeric and/or the spatial distribution of image intensities within defined regions of interest. Generally, texture features excel in providing more detailed structural and dimensional information of pixel intensity values distribution, which facilitates an upgraded quantitative perception of tissue imaging characteristics and the more effective inter-comparison between images (87).

Numerous studies have identified significant statistical correlations of texture features with tumors' biological properties, as informed from histopathological findings. Therefore, it is widely accepted that these parameters are more sensitively associated with various clinical endpoints compared with the qualitative radiologic and clinical data more commonly utilized today and may possibly serve as useful tools for the assessment of the severity, degree of change, or status of a cancer lesion, relative to normal (6,88). Of note, the afore-mentioned conclusions have led to the development of many different Computer Assisted Diagnostic (CAD) systems for standardizing and using the technology in the clinical setting (7).

CAD algorithms are mainly composed of two stages, i.e., detection and classification of suspicious regions, into cancerous and normal tissue (89). Initially, detection is performed using basic image enhancement methods, descriptors of statistical distribution of intensity values, and decomposition of the image through wavelet transforms, in order to investigate differences between tumorous areas and background. Subsequently, based on an initial hypothesis concerning possible connections between cancer progression and specific imaging data, CAD systems use a set of quantitative imaging features describing the geometrical structure, intensity

distribution and texture of a Region of Interest (ROI), automatically or manually contoured (89).

However, the advances in medical imaging systems, transforming scanners form single imaging modalities into advanced computational systems producing a variety of numerical parameters, as well as the exponential growth in computer technology of the past decade, including novel pattern recognition, have opened new horizons in the quantitative imaging biomarker analysis, introducing the rapidly evolving field of "Radiomics". Etymologically, radiomics comes from the union of the terms radio- (radiation or radiology), and -omics, a common suffix used to form nouns relating to the study of the totality of a field (e.g., genomics, proteomics, metabolomics, transcriptomics), and mainly focuses on the global non-invasive assessment of cancerous lesions biological profiles.

Generally, Radiomics can be considered as an extension of CAD systems. In contrast to CAD's simplicity and ability for answering only elementary clinical questions by using few data and evaluating pre-defined hypothesis regarding the specific clinical task of interest, Radiomics analysis aims to the integration and analysis of large-scale imaging and clinical information. The feasibility for implementing Radiomic analysis arises from the profound difficulty in having a-priori knowledge or making hypothesis when investigating the plethora of complex clinical quantitative information. Of note, the applicability of Radiomic analysis is based on the recent developments of high-throughput computational tools and statistical frameworks that facilitate exploitation of data-driven inference approaches. The latter enable the precise association of the extended libraries of voxel-based quantitative variables (e.g., relating to tumor size, shape, gray level intensity and texture, etc.) with biological and clinical endpoints, for enhancing the non-invasive biomarker discovery and overcoming the limitations of conventional evaluation methods.

Especially, the exploitation of AI techniques to extract clinically meaningful conclusions from the quantitative variables, has enabled both the identification of clinically significant

associations between imaging biomarkers and patient-specific pathophysiological characteristics, as well as the development of reliable and reproducible integrative decision support systems, that hold potential to augment diagnostic benefit, enhance patient risk stratification and prognostication buttressing the emerging targeted therapeutic approaches (90).

3.2 Radiomic Analysis workflow

Image segmentation is usually the first step, after data pre-processing (noise reduction, correction of artifacts, normalization, etc.), in the radiomic analysis workflow towards lesion evaluation for diagnosis and selection of appropriate treatment plan. The precise definition of breast lesion boundaries is a very important procedure, as it affects the subsequent qualitative analysis of the radiomic descriptors extracted from the corresponding regions or volumes of interest (ROI/VOI). In daily clinical routine ROIs are manually segmented by expert radiologists, but besides that it is a time-consuming process, this approach induces intra- / inter-observer variability and reproducibility errors, as many tumors present indistinct and blurring boundaries (91). The development and validation of novel semi-automated or automated segmentation algorithms is an open research field which presents interesting and sophisticated results. However, the semi-automated approaches are mandatory, so that the final choice remain user-depended, since fully automated methods are so far feasible only if there are strong signal differences between the lesion and the background (92). In addition, time-cost minimization for segmenting all tumor slices in tomographic imaging modalities, such as MRI, enables the reconstruction of three-dimensional (3D) tumor models, which further facilitate the global assessment of the pathology.

After tumor delineation, radiomic features are extracted from the information contained in the segmented ROIs, that can be used to qualitative assess tumor phenotype, aggressiveness,

treatment response, cancer genetics, and differentiate between benign and malignant tumor (84). Radiomic features may be divided into several categories depending on their characteristics, such as shape-size based, histogram-based, textural, and transform-based features (81,89). Shape and size-based features provide information about tumor location and different size parameters, like surface, volume, diameter, sphericity, and surface-to-volume ratio. First order histogram parameters, such as mean value, standard deviation, percentiles, skewness, kurtosis, entropy enable the rough assessment of pixel intensity global distribution without considering spatial variations. Second order histograms such as Gray level Co-occurrence matrices (GLCM) (93,94) and Gray Level Run Length Matrices (GLRLM) (95,96) characterize spatial relationships between pixel intensities in different 2D or 3D directions, and thus are robust in quantifying tumor structural properties and various patterns of heterogeneity.

Once radiomic features have been calculated and stored along with all other quantitative imaging and clinical data, a set of the few most important features need to be defined and selected for ML model development. Generally, within the vast amounts of radiomic features many spurious correlations, collinearities and noise are present, and ML models tend to overfit and generalize poorly in new data. This effect is critical in medical imaging ML models because of the relatively larger number of predictors (>1000) compared to the number of training cases, especially when considering the advanced imaging applications (<500). To this scope the use of feature selection / dimensionality reduction techniques is highly recommended (7). Besides the reduction of feature number towards training reliable ML models, these techniques have proved valuable for identifying robust imaging biomarkers that also help to enhance clinical interpretation. Subsequently the main task is to correlate the selected feature subset to diagnostic and prognostic outcomes or to the underlying biology. To date the main research focus is on the incremental diagnostic and predictive value that can be obtained from advanced machine learning classifiers, like Logistic Regression (LR), Support Vector Machine (SVM), Random Forests (RF) and boosted trees classifiers. These techniques present huge potential to

improve the understanding of complex pathological conditions, through identifying robust associations between morphological or functional changes in imaging and clinical variants linked to the diseases, in patients' subgroups.

Lately, Deep Learning (DL), a class of machine learning algorithms, that has become the state-of-the-art approach in computer vision, essentially replacing conventional ML algorithms for most applications, are being introduced in medical image analysis (97). DL algorithms excel at learning a hierarchy of increasingly complex imaging features, directly from raw data and are considered as a powerful alternative to the quite demanding and time-consuming conventional ML-based radiomic analysis approaches, that involve manual/semi-automatic tumor delineation, hand-crafted feature extraction and testing of different classifiers (98). Overall, these pattern recognition techniques based on their ability to learn information from the provided training datasets have demonstrated a superior efficiency in the understanding of complex pathological conditions and making accurate classification of disease status, through identifying robust associations between morphological/functional changes in imaging and clinical variants linked to the diseases. More importantly, due to the inherent requirement for accumulated resources (large datasets, increased computational power), for reaching accurate training, DL imaging diagnostic models have better generalization perspectives and can more efficiently adapt to diverse scanning protocols (Figure 14).

To date, quantitative imaging research constitutes a multidisciplinary scientific field that brings together many different specialties (clinicians, biologists, physicists, engineers, IT professionals). However, it is still a very challenging process, including various complicated tasks, (e.g., clinical, and histological examinations, multi-modality image scanning), facing complex technical difficulties (development of novel computational methods) and methodological challenges (poor study design, data overfitting, and lack of standards for results validating) (99,100).

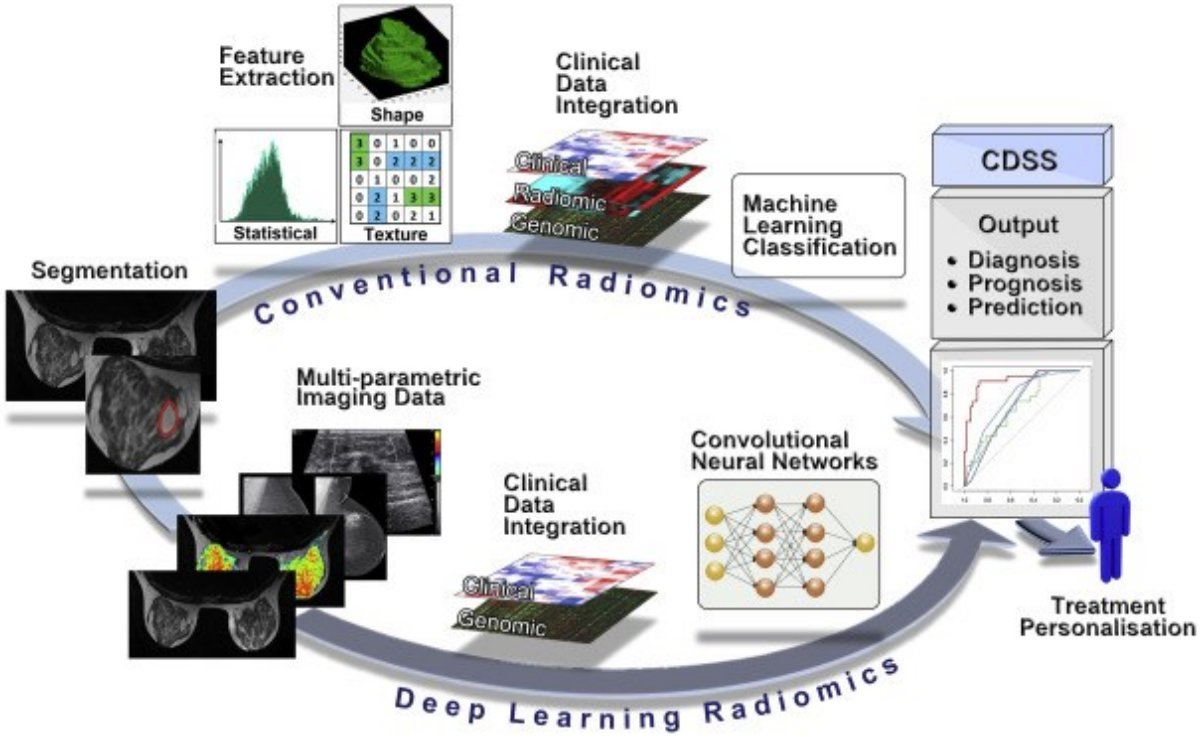

Figure 14: Conventional and Deep Learning Radiomic analysis workflows.

The following studies that were conducted in the framework of the present thesis aim in the exploitation of multiparametric MRI information for addressing brain and breast cancer diagnostic challenges. Towards this direction the respective methodological approaches have made use of robust radiomic analysis pipelines to identify and validate clinically relevant imaging biomarkers and expand previously reported quantitative imaging models.

this page intentionally left blank

Chapter 4

4.1 A Radiomic Analysis Model of Advanced Multiparametric MRI for Glioma Grading

4.1.1 Aims and Objectives

Gliomas are the most aggressive primary brain tumors presenting poor survival rates grades. According to the World Health Organization (WHO), gliomas are subdivided into four categories considering their malignancy status, i.e., grades I, II (low grade gliomas - LGG) and grades III, IV (high grade gliomas - HGG) (101). Therefore, preoperative accurate grade classification is of main clinical importance, related to early prognosis as well as precise selection of the therapeutic approach.

To date, several studies have reported that MRI either with conventional (102,103,104) or more importantly with advanced MRI sequences (105,106,107,108) may contribute to tumor heterogeneity assessment, overcoming sample-biopsy limitations towards glioma grading, providing different perspectives of gliomas pathophysiology. The proposed methods are complemented by advanced image analysis techniques, such as morphological and texture analysis methods, for increasing diagnostic accuracy through the quantitative assessment of the specific information provided by structural and functional MR images (109). Even though the specific findings seem promising, the increased methodological variability of the current MRI unilateral evaluation approaches, resulting into conflicting sensitivity and specificity reports,

could lead to a misinterpretation and hence underestimation of gliomas' biological heterogeneity mechanisms.

As it has been mentioned from certain research studies exploiting mp-MRI data (110,111,112,113,114), the combination of several MRI parameters, evaluating underlying pathophysiology, may lead to a better understanding of tumor characteristics, and a more accurate classification of LGGs and HGGs. Furthermore, the recent advent of Radiomics i.e., the inclusion of novel approaches incorporating advanced quantification and classification methodologies, which facilitate the manipulation and evaluation of multidimensional imaging feature data, may serve as a sophisticated analysis framework (79,115). In addition, the potential applicability of radiomic analysis in performing various clinical data associations (e.g., imaging, genomics) (116,117), has been already exploited by some glioma grading studies (118,119), in consent with the 2016 WHO guidelines (120) in which molecular genomic factors (e.g. Isocitrate dehydrogenase (IDH) mutation status, 6-methylguanine-DNA methyltransferase (MGMT) promoter methylation) have been added to histological factors for glioma characterization.

Hence, it is evident that in the precision medicine era, a plethora of quantitative parameters should be taken into consideration for an accurate tumor characterization. In this direction, a radiomic approach with mp-MRI data, can demonstrate a superior contribution towards glioma classification, because of its advantages in describing the detailed microarchitectural and functional tumor processes. However, there is still a demand for further investigation on the validation and utility of combining such techniques, to establish a powerful non-invasive tool in clinical practice (121).

The aim of this study was to create and utilize a radiomic analysis pipeline, to comprehensively evaluate a full 3T multiparametric MRI approach, including all the available advanced techniques, i.e., DWI, DTI, 1H-MRS and DSCE imaging, to produce valid imaging biomarkers for the distinction between high- and low- grade gliomas. The specific

implementation utilizes a DTI semi-automated clustering segmentation technique for delineating tumor core VOIs in all the available MRI parametric images. Radiomic feature extraction included first and second order textural features, and additional advanced MR quantitative parameters (1H-MRS metabolite ratios, relative Cerebral Blood Volume). Feature selection and classification modelling are based on Support Vector Machine classifiers (SVMs), while the discrimination accuracy is evaluated with Receiver Operator Characteristic (ROC) analysis.

To the best of our knowledge, there are only a few studies (122,123) that incorporate conventional MR data accompanied by all the available advanced MR neuroimaging techniques used in brain tumor evaluation. Our approach produced a robust analysis pipeline which shows that radiomic features derived from mp-MRI, supports accurate low vs high grade glioma classification, by exploiting the underlying pathophysiology as expressed by the advanced neuroimaging techniques.

4.1.2 Material and Methods

Multiparametric MRI acquisition protocol

Forty patients initially diagnosed with Low- or High-Grade Gliomas (20 LGG & 20 HGG) underwent an MRI exam on a 3-Tesla MR wholebody scanner (SignaHDx; General Electric (GE) Healthcare, Waukesha, WI, USA), applying an advanced imaging examination protocol including, conventional MRI sequences, 1H-MRS, DWI, DTI and DSCE, using a 4-channel birdcage and an 8-channel phased-array head coil (Figure 15). Prior to this retrospective study, local Institutional Review Board approval and patient consent was obtained.

The conventional MRI protocol included pre-contrast sagittal and transverse T1-w FSE (Repetition Time (TR) / Echo Time (TE) 700 ms/9.3 ms), transverse T2-w FSE (TR/TE 2640

ms/102 ms), coronal T2-w FSE (TR/TE 2920 ms/102 ms), and T2-w Fluid Attenuation Inversion Recovery (FLAIR) (TR/TE 8500 ms/130 ms) scans, with 512 × 512 matrix size, 24 × 24 cm^2 Field of View (FOV), 0.5 mm in-plane resolution and slice thickness of 5 mm with gap 1 mm. Post-contrast isotropic 3-dimensional Spoiled Gradient Echo (3D-SPGR, TR/TE 6.9 ms/2.1 ms, 12° flip angle, 24 × 24 cm^2 FOV, 136 slices of 1 mm thickness and 1 mm^3 voxel size) and T1-w post contrast axial images were also obtained.

1H-MRS imaging was performed using the automated PROton Brain Exam (PROBE; GE Healthcare, Waukesha, WI, USA) spectroscopy package before contrast administration to avoid signal disturbance. MRS was performed both as Single Voxel (SV) and multivoxel (Chemical Shift Imaging, CSI) when this was feasible. It actually depended on the size of the lesion and the anatomical site. We avoided areas of known susceptibility differences leading to poor field homogeneity, including the mesial anterior temporal and inferior frontal lobes because of their proximity to air-cavities, or proximity to the skull due to lipid contamination. The measurement parameters used in single voxel scans were 1500/35 ms (TR/TE), 128 signal acquisitions and voxel size was chosen to be not less than 3.375 cm^3 for adequate SNR with a duration of 3 min and 48 sec. The typical SV used was of the order of 8 cm3 (2 × 2 × 2 cm) for increased SNR. The measurement parameters used in 2D-MRSI were 1000/144 ms (TR/TE), 16x16 phase encoding steps, section thickness ≥ 10 mm and the FOV size was adjusted to each patient's brain anatomy. The duration was of the order of 4 min and 20 sec. Typical spectra of the corresponding tumor groups are shown in Figure 15.

The use of multivoxel (CSI) technique is a very valuable technique to evaluate simultaneously the retrospective area of the tumor site (when applicable, taking into account areas of heterogeneity and lipids contamination), and was acquired at a higher echo time of 144 ms hence we had a better evaluation of lipids and lactate. The differentiation of lipids and lactate when in doubt was done using the flipping of lactate at long TE (144 ms) and analysis using the TARQUIN software (http://tarquin.sourceforge.net/) (124).

We generally used the auto shimming method based on the vendor's software, but manual shimming was implemented in difficult cases by adjusting receiver/transmitter gains. There were a few times that despite all this effort, complete elimination of small local deviations from the B0 field uniformity was very difficult and these cases were omitted. In general, our linewidth was kept below 10 Hz for SV and below 20 Hz for CSI.

Diffusion-weighted MR imaging was performed prior to contrast media injection, via a single-shot, spin-echo, echo planar sequence with b-values of 0 s/mm^2 and 1000 s/mm^2 performed in 50 sec. DTI was performed in the axial plane with single-shot spin-echo echo planar: TR/TE 8000 ms/89.8 ms, gradients applied in 32 non-linear directions, b = 0 s/mm^2 and 1000 s/mm^2, FOV = 24 cm^2, 1 mm in-plane resolution, slice thickness = 4 mm with gap = 1 mm and NEX = 1, with a duration of 4 min and 32sec.

The DSCE MR images were acquired with a single-shot gradient echo planar imaging sequence (TR/TE 2000 ms /20.7 ms, flip angle 60°, FOV = 24×24cm^2, slice thickness = 5 mm with gap = 1 mm, NEX = 1) during the first pass of bolus of gadolinium contrast material (DOTAREM) at a dose of 0.1 mmol/kg body weight with a duration of 1 min and 08 sec. The location of the perfusion-weighted MR data set was determined by using the axial T1-w images after contrast injection to locate the lesion and axial T2-w images to locate the peritumoral T2 signal abnormality.

At this point, it must be mentioned that gadolinium-containing contrast agents are normally excluded by the blood-brain barrier (BBB) and cannot enter the extracellular spaces of the brain and spinal cord. The disruption of the BBB caused by diseases like enhancing tumors, subacute infarcts etc., results in leakage of the contrast agent into the extravascular space. This leakage should be corrected for, because it can lead to systematic errors due to the additional pronounced T1- and T2*-relaxation effects that violate the fundamental assumption of tracer kinetic modelling on which DSCE is based, that no recirculation of the contrast agent occurs.

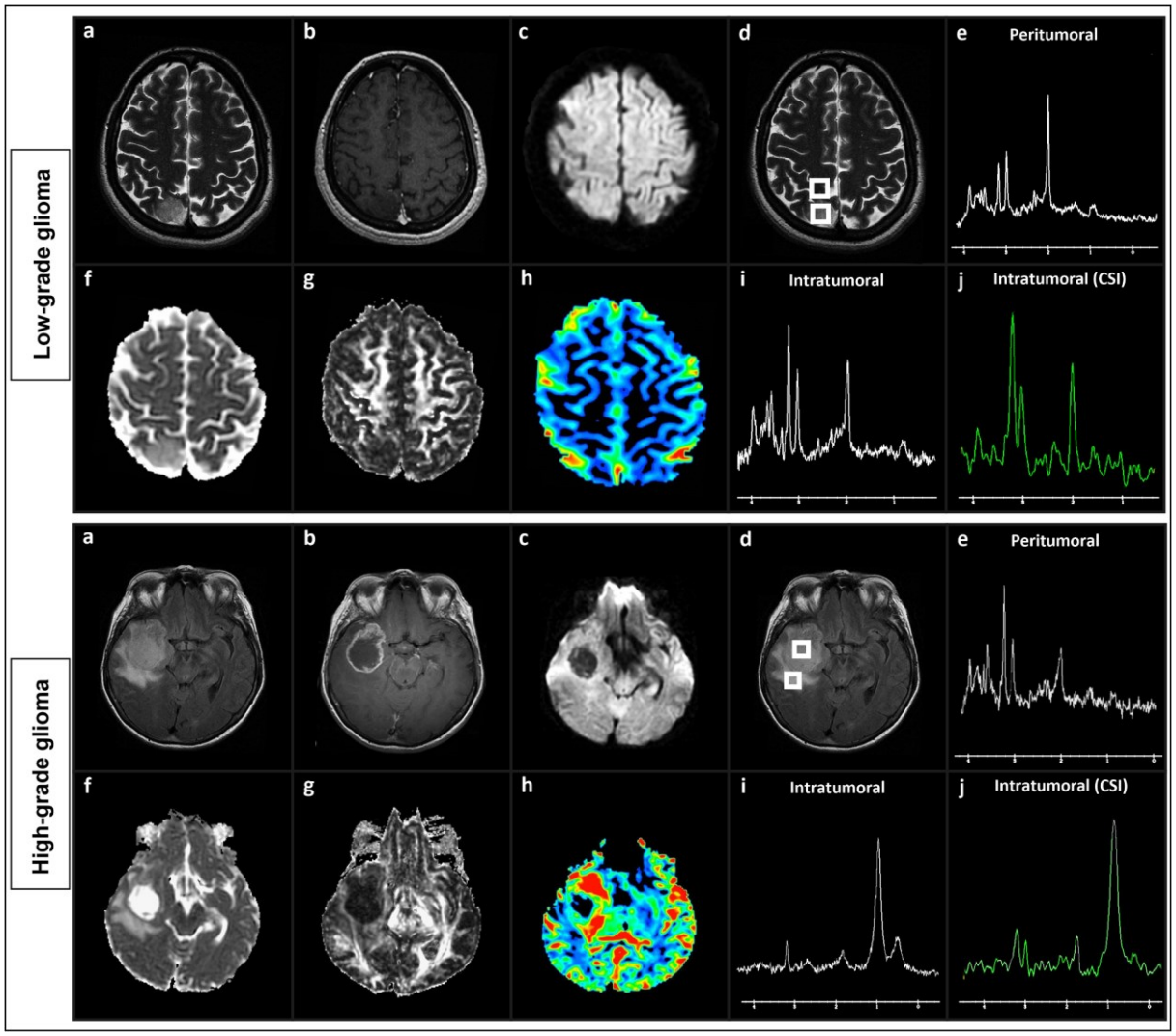

Figure 15: Upper image; A case of a low-grade glioma, presenting high signal intensity on a T2-weighted image (a), no contrast enhancement on a T1 3D-SPGR image (b) and an isointense signal on a diffusion-weighted image (c). The lesion shows increased MD (f), lower FA (g) and no significant perfusion (h) on the corresponding parametric maps. The peritumoral (e) and intratumoral (i and j) spectra are also depicted. Lower image; A case of a high-grade glioma (glioblastoma multiforme), presenting high signal intensity on a T2-weighted image (a) and ring-shaped enhancement on a T1-weighted post contrast image (b). On the DW-image the lesion presents low signal intensity (c) resulting in higher intratumoral MD (f), lower intratumoral FA (g) and high peritumoral rCBV (h) reflecting tumor infiltration in the surrounding parenchyma. The corresponding peritumoral (e) and intratumoral (i and j) spectra are also depicted.

Hence T1 shortening from extravascular gadolinium can lead to increased signal and may blunt the desired T2* shortening on which DSCE is based on. Several strategies exist to minimize this effect, from simple techniques to more sophisticated models of the first pass kinetics

(125,126). One simple and popular method that we have used in our work is called 'preloading'. A one-fourth to one-third of the total dose was administered about 5–10 min before the dynamic imaging, and a T1-w to guide the perfusion section positioning was run in between. This 'preloading' of gadolinium reduces contaminating T1 effects by shortening the pre-bolus intravoxel T1, raising the baseline signal so that T2* changes can then be better appreciated (127).

Data post-processing

Initially, all available MRI raw data were converted from Digital Imaging and Communications in Medicine (DICOM) to Neuroimaging Informatics Technology Initiative (NIFTI) 1.1 format with the 'dicom2nii' tool provided by MRIcron software (https://www.nitrc.org/projects/mricron). Subsequently, FSL software of FMRIB Software Library v5.0 (https://fsl.fmrib.ox.ac.uk/) (128,129,130), was utilized for parametric MR volumes co-registering and re-slicing into an isotropic voxel size of 1 mm^3, as well as applying bias field corrections. DTI data post-processing was performed with FSL, including motion artifacts and eddy current distortions corrections (131), brain tissue extraction, Diffusion Tensor estimation and Mean Diffusivity (MD), Fractional Anisotropy (FA), Pure Isotropy (p) and Pure Anisotropy (q) parametric maps calculation (132). In-vivo SV and multivoxel spectroscopic data analysis and calculation of metabolite ratios were performed on an Advanced Linux workstation using the Functool software (GE Healthcare). Postprocessing of the raw spectral data included baseline correction, frequency inversion and phase shift. Gaussian curves were fitted to NAcetyl Aspartate (NAA), Choline (Cho), Creatine (Cr), lipid and lactate metabolites' peaks for determination of peak area. Finally, metabolite ratios of NAA/Cr, Cho/Cr, mI/Cr and Lipids/Cr were calculated from the area under each metabolite peak. The Functool software was utilized for processing DSCE data and analyzing the perfusion imaging time curves for extracting the Cerebral Blood Volume (CBV) parametric maps. In addition, the gadolinium uptake time

curves were also utilized for identifying the volume of contrast agent maximum uptake for every patient, which was used in the subsequent radiomic analysis process for textural features extraction.

Volume of interest (VOI) extraction

In the framework of radiomic-based quantification of tissue heterogeneity, the accurate and reproducible segmentation of regions and volumes of interest is critical. To this scope, a clustering segmentation method reported in a previous study by Vamvakas et al. (133), was utilized for the identification of different tumor subregions (habitat imaging (79)), providing the radiologist with the appropriate information for manually performing whole tumor delineation. However, the quantification of tumor imaging characteristics may easily be biased from the presence of peritumoral edema and hemorrhagic tumor components, which do not have a contiguous occurrence in the two tumor groups. Probably, they would be offered as semantic annotations (79), however semantic features were not considered in this study.

In the literature both intra and peritumoral regions are usually evaluated (6,134,135). The hypothesis is that high grade gliomas are infiltrative lesions, thus pathological tissues may be present in the surrounding white matter, while low grade gliomas are not. Therefore, the surrounding edema of LGGs is considered to be pure vasogenic whereas around HGGs there should be a combination of vasogenic edema and infiltrating tumor cells along the perivascular spaces. Hence all techniques would yield some kind of differentiation based on that. On the other hand, a great deal of evidence in the literature supports that there can be great discrepancies regarding the peritumoral region especially regarding MRS and DTI (113,136,137). Moreover, LGGs often appear without any significant peritumoral parenchyma alteration, hence a reproducible estimation would be to compare the actual tumors and evaluate whether radiomic techniques such as texture or morphological features may provide extra

information. Therefore, we opted to evaluate only the intratumoral area, aiming to identify differences regarding diffusive and solid growth patterns of LGGs and HGGs respectively, for two reasons: a) The radiomic analysis regarding textural features should be performed on a directly comparable and reproducible evaluation area for both tumor types. Hence, in order to ensure lack of bias and reproducibility we chose to use the tumor core of both lesions, and b) there can be difficult cases where peritumoral evaluation might not be possible, either due to areas of poor homogeneity (e.g., air filled cavities like the sinuses or proximity to the skull) or maybe even to the lack of cooperation of the patient for the whole duration of the exam (especially for MRS). In such cases, the radiologist is left with the evaluation of the intratumoral area which is obtained first. So, the hypothesis is that an evaluation of the intratumoral region only, should be able to discriminate between tumor grades.

The proposed clustering segmentation method is based on DTI parametric maps for classifying the brain voxels of each patient into groups with similar isotropic and anisotropic diffusion properties, accounting for normal and tumorous brain tissue diffusivities. Specifically, k-medians clustering (k = 16) is applied on a 2D histogram of p (isotropic) and q (anisotropic) components of the diffusion tensor, derived from all patient cohort. Subsequently, Red-Green-Blue (RGB) color mapping of clusters according to the relative magnitudes of p, q and T2-w (from b = 0 s/mm^2 DTI volumes) values of the cluster centroids and subsequent colour assigning to each individual patient's brain voxels according to their position in the p-q space, results in whole brain segmented maps (Figure 16). These color-coded maps are based on the contouring provided by diffusion properties, being robust in displaying tissue microarchitecture, thus healthy and tumorous brain tissues present distinctive boundaries.

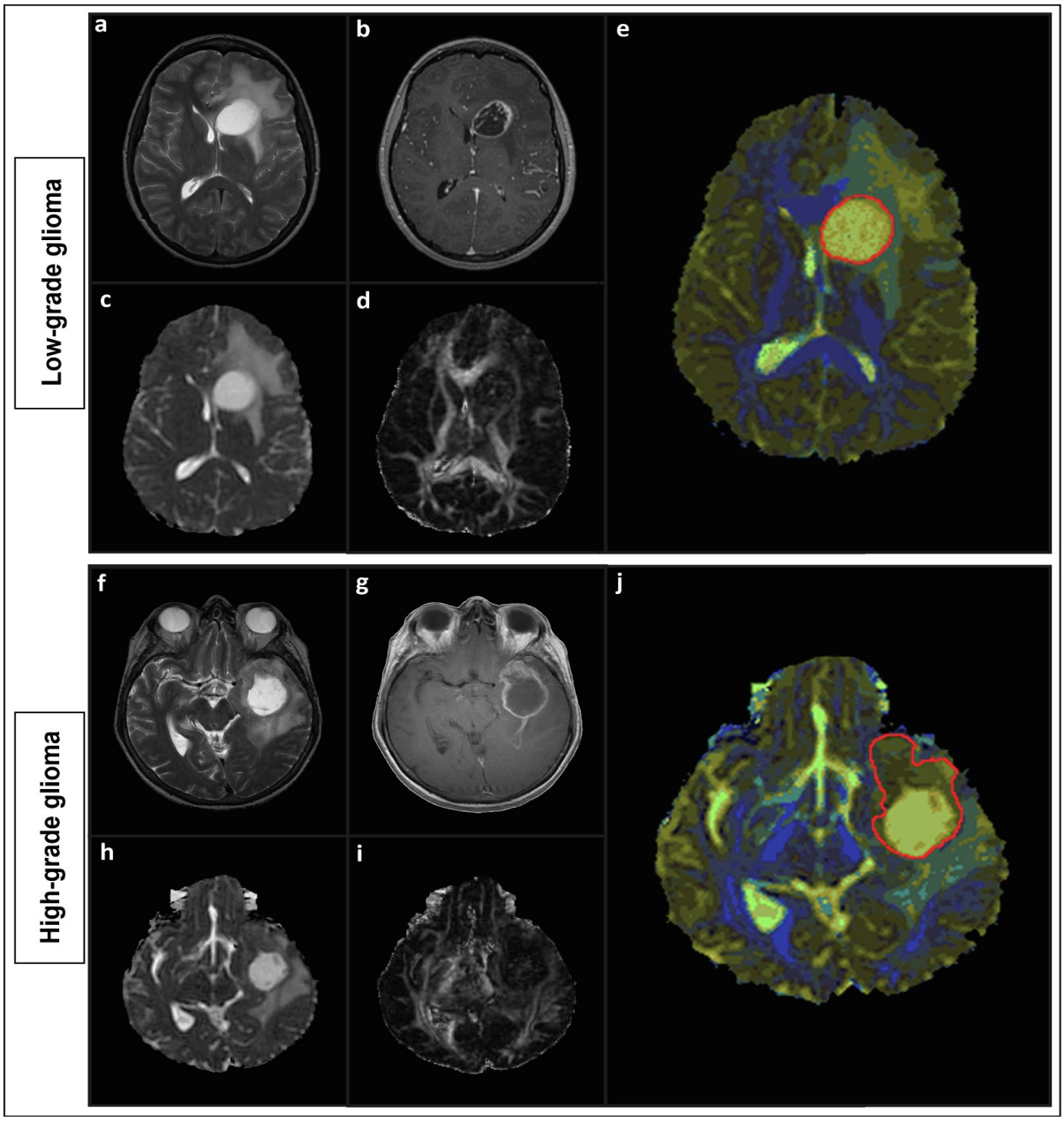

Figure 16: Whole brain segmented maps of a LGG (e) and a HGG (j) case, resulting from the k-medians clustering of the DTI isotropic (c, h), anisotropic (d, i) and T2-wheighted components feature space (a, f). The different colors presented (k=16) correspond to distinct brain tissue diffusion properties, which facilitate the precise definition of healthy tissue, tumor core and peritumoral edema. The final delineation of tumor core (red outline) is the outcome of the further combination with T1- wheighted post-contrast imaging (b, g).

Finally, tumor core segments highlighted by the clustering technique, were delineated on colormaps by an experienced radiologist, and stacked up to form tumor VOI masks. Subsequently, these VOI masks were applied on the various co-registered multiparametric

images of our dataset (Figure 17), resulting in a set of 3D parametric representations of the gliomas.

Each patient's VOIs taken into account were exactly the same on every tumor core region for all the imaging series (i.e., T1-w, T2-w, FLAIR, DTI and DSCE raw) except for CBV and spectroscopy. Specifically, the rCBV measurements were calculated from ROIs which were placed in regions of the highest perfusion as seen on the CBV color overlay maps, referred as the 'hot spot' method. The placement of ROIs was carefully performed to avoid large vessels based on the combined information from T1-w image after contrast enhancement, and T2-w FSE images. The mean rCBV was used for the subsequent analysis.

For both spectroscopic techniques, a rectangular ROI was localized by using the transverse T2-w FLAIR or T2-w FSE, sagittal T1-w FSE and coronal T2-w FSE imaging sequences. Spectra for each patient were acquired from the intratumoral, peritumoral and contralateral regions of interest. The contralateral normal area was used as the control spectrum. Within the tumor, the size and location of the voxel were carefully adjusted to include as much of the solid tumor portion as possible, avoiding the inclusion of obvious cyst, hemorrhage, edema, calcification, and normal-appearing brain. For each patient, the SV scan was first applied in the intratumoral region of interest followed by peritumoral and contralateral normal area. The 2D-MRSI scan was then performed, including the region as the one previously chosen for the SV scan, in order to have a direct metabolite comparison between the two 1H-MRS techniques.

Radiomic feature extraction

Histogram analysis have considered 12 statistical features acquired from normalized data histograms with an in-house MATLAB 2015b (https://www.mathworks.com/) code. Texture analysis was implemented in MaZda ver.5 software (http://www.eletel.p.lodz.pl/programy/mazda/) (138,139,140), considering 11 GLCM in 5-

pixel distances and 5 GLRLM features, both calculated on 8-bit quantized images. After the acquisition, textural features were averaged over the 13 directions of the 3D image, to obtain directionality independence measurements. In summary, the quantitative radiomic features extracted from the eight tumor parametric VOIs, regarding p, q, MD, FA, T1w-C, T2w-FSE, T2w-FLAIR and volumes of maximum gadolinium uptake of DSCE MRI, along with the four metabolic ratios of 1H-MRS (Ch/Cr, NAA/Cr, mI/Cr, Lipids/Cr) and mean rCBV values (Figure 17), resulted in a total of 581 distinct attributes for each subject.

Feature selection and classification

In a recently reported study, Zhang et al. (141) have made comparisons between several feature selection and classification algorithms implemented in Weka software (https://www.cs.waikato.ac.nz/ml/weka/) (142), regarding a mp-MRI dataset for glioma grade classification. According to their results, the combination of Support Vector Machine – Recursive Feature Elimination (SVM-RFE) and SVM classification demonstrated superior performance regarding the specific task, in comparison with other feature selection and classification models.

Adopting the indices and the basic methodological concepts of the abovementioned study, machine learning feature selection and classification were implemented in Weka 3.8 software, following four major steps, as they are described below (Figure 17):

In the beginning, radiomic features were imported in the SVM-RFE algorithm ('SVMattributeEval' with the 'Ranker' search method), which is a wrapping feature selection method introduced by Guyon et al. (143). More specifically, SVM-RFE iteratively eliminates a set of features by removing the less important one, according to the weighting vectors of an SVM classifier. Consequently, feature ranking in a descending order of discriminative importance is obtained, according to the elimination sequence.

Afterwards, the performances of different well established SVM packages ('LibLinear', 'LibSVM', 'SMO') were evaluated with ROC analysis, on consecutively SVM-RFE feature subsets, to identify the SVM model presenting the best fitting to our dataset. Each classifier was repeatedly trained, starting with the 10 higher-ranked features with a stepwise of adding up 10 features at each iteration, and tested with leave-one-out cross-validation (LOOCV) to avoid overfitting by increasing the number of folds. As it was observed, the 'SMO' package with linear kernel (default), that is an SVM classifier implementing Platt et al. Sequential Minimal Optimization (SMO) algorithm (144), achieved the best performance, compared to 'LibLinear' and 'LibSVM'. At this step, all the above-mentioned SVM classification packages were implemented utilizing Weka 3.8 default hyperparameters.

Subsequently, the task of determining the optimal feature subset was driven by the classification performance of 'SMO' classifier through a detailed investigation between different numbers of SVM-RFE top ranked features, with a stepwise of adding 1 feature at each iteration. As soon as the optimal features where determined, according to the subset presenting the highest accuracy values, further investigation through a grid search method ('GridSearch') aiming in accuracy maximization was utilized for optimizing the hyperparameters of the classification model.

At this point, it should be noted that all data post-processing and analysis steps were implemented in state-of-the-art software which have been utilized by many studies (145). In addition, the results of our work have been based on the pre-validations of the used software, as these were analytically described in their original studies (124,128,129,130,131,132,138,139,140,142).

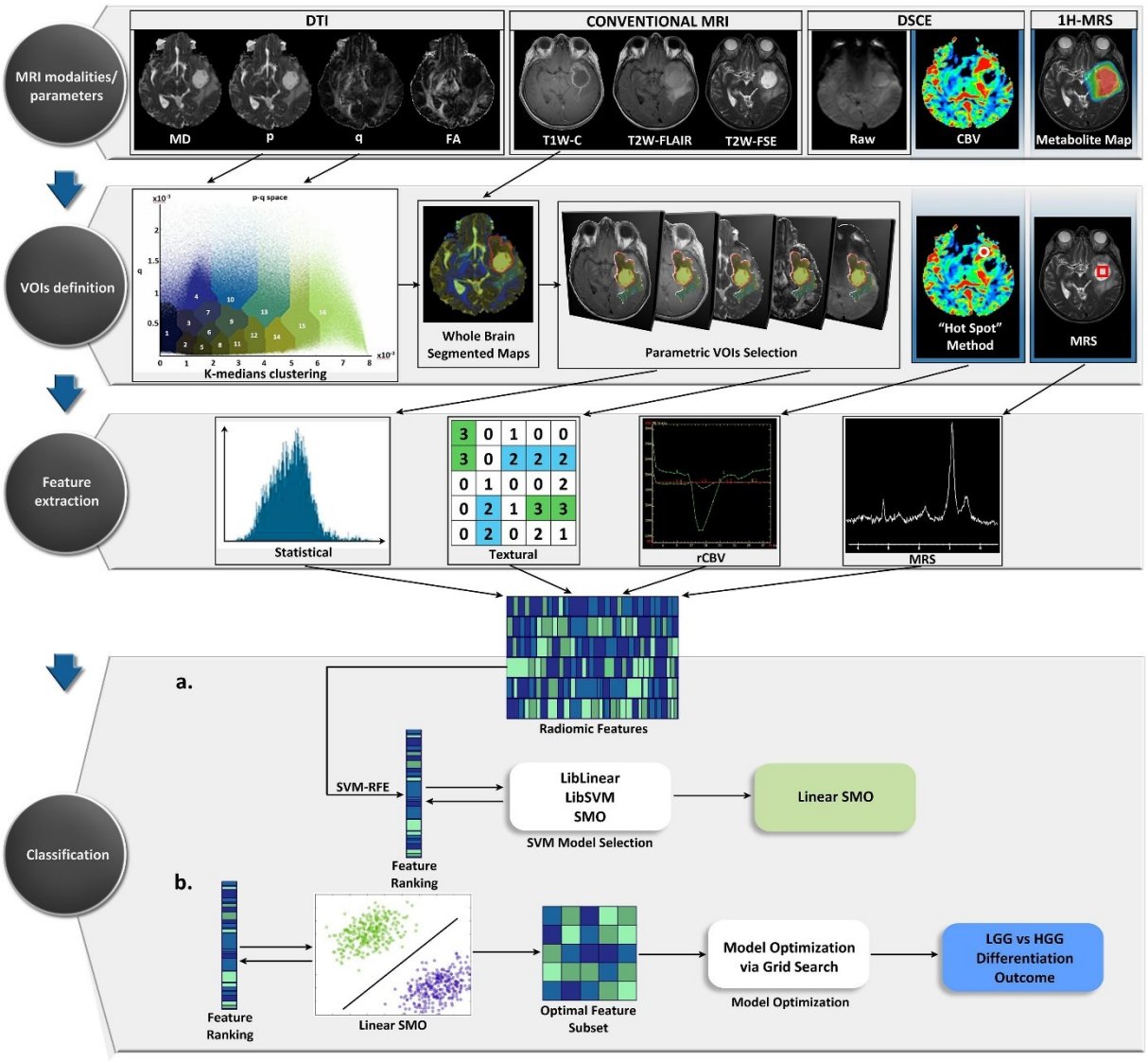

Figure 17: The Radiomic Analysis pipeline of the study. In the first two sub-panels a complete sample of a patient's multiparametric MR images and the respective VOIs placement methodologies are depicted. Subsequently, the figure presents feature extraction (third sub-panel) and the two steps of classification (fourth sub-panel), including (a) the optimal SVM classifier selection and (b) the optimal feature subset definition, along with the final differentiation outcome.

4.1.3 Results

The initial classification trials performed in the study have shown that linear kernel 'SMO' algorithm demonstrated better classification performance (Acc = 90% / AUC = 0.899) in comparison with 'LibLinear' (Acc = 55% / AUC = 0.500) and 'LibSVM' (Acc = 75% / AUC = 0.732). The subsequent evaluation of different feature subsets with linear 'SMO', has nominated the adaptation of 21 SVM-RFE top ranked features, shown in Table 3, which provide the highest discriminating ability between LGGs and HGGs (Acc = 95% / Se = 93.9% / Sp = 94.4% / AUC = 94.4%). Also, Lipids/Cr metabolic ratio was the highest ranked feature. As shown in Table 4, all MRI modalities/parameters have contributed to the final feature set, except for DTI's Fractional Anisotropy (FA). In addition, 8 features where histogram-based and 12 features where textural-based, while GLCM features were much more statistically significant than GLRLM (11vs1).

Finally, the classification model refinement performed by 'Grid Search' method, have determined a complexity parameter c = 103 for the linear kernel 'SMO', demonstrating a total performance of 95.5% Accuracy (Acc), 95% Sensitivity (Se), 96% Specificity (Sp) and 95.5% Area Under the ROC Curve (AUC).

Table 3: SVM-RFE top-ranked feature subset selected for classification

Rank	MRI modality / parameter	Quantification Method	Radiomic Feature	LGG mean ± sd	HGG mean ± sd
1	1H-MRS	-	Lipids/Cr	0.90 ± 0.38	3.34 ± 1.17
2	T1W-C	Histogram	Skewness	0.17 ± 0.79	0.56 ± 0.21
3	q	Histogram	Mean	0.32 ± 0.07 *	0.24 ± 0.05 *
4	T1W-C	Histogram	Variance	211.91 ± 38.59	402.46 ± 64.09
5	MD	GLCM	Inverse Diff. Moment	0.16 ± 0.05	0.11 ± 0.04
6	q	GLCM	Sum of Squares	115.91 ± 19.98	133.73 ± 15.62
7	DSCE	GLRLM	Run Length Non-Uniformity	904.61 ± 460.26	1901.95 ± 1046.79
8	T1W-C	GLCM	Angular Second Moment	2.48 ± 0.90 **	1.79 ± 0.30 **
9	T2W-FLAIR	GLCM	Difference Variance	47.98 ± 27.73	23.51 ± 11.68
10	q	GLCM	Correlation	0.24 ± 0.10	0.17 ± 0.16
11	q	Histogram	Median	0.29 ± 0.06 *	0.22 ± 0.04 *
12	MD	GLCM	Difference Entropy	1.23 ± 0.11	1.35 ± 0.10
13	T2W-FLAIR	Histogram	Variance	174.33 ± 33.33	140.05 ± 36.21
14	rCBV	-	Mean	1.68±0.59	7.80±5.13
15	p	GLCM	Contrast	94.79 ± 51.75	156.34 ± 63.78
16	T2W-FLAIR	GLCM	Sum Variance	171.32 ± 76.73	102.79 ± 37.33
17	DSCE	Histogram	Minimum	2406.75 ± 1105	1391.63 ± 852.41
18	T2W-FLAIR	GLCM	Difference Entropy	1.25 ± 0.11	1.19 ± 0.10
19	T2W-FSE	Histogram	Entropy	5.15 ± 0.39	4.94 ± 0.36
20	DSCE	GLCM	Angular Second Moment	4.97 ± 2.89 **	2.40 ± 1.38 **
21	q	GLCM	GLCM Sum Entropy	1.79 ± 0.05	1.76 ± 0.05

Mean and Standard error in the units x10^{-3} mm^2/s

****Mean and Standard error in the units x10^{-3}***

Abbreviations: DCSE, Dynamic Susceptibility Contrast Enhanced; GLCM, Gray-level co-occurrence matrix; GLRLM, Gray-level run-length matrix; MD, Mean Diffusivity; MRS, MR Spectroscopy; p, pure isotropy; q, pure anisotropy;

Table 4: Summarized results showing the distribution of the significant radiomic features among MR modality/parameter and feature extraction method

MRI modality / parameter / Features		Conventional MRI			DTI				DSCE		MRS
		T1W-C	T2W-FSE	T2W-Flair	MD	FA	p	q	Raw	rCBV	Lipids/Cr
Histogram		2	1	1	0	0	0	2	1		
Textural	GLCM	1	0	3	2	0	1	3	1	-	-
	GLRLM	0	0	0	0	0	0	0	1		
Total Radiomic Features		**3**	**1**	**4**	**2**	**0**	**1**	**5**	**3**	**1**	**1**

Abbreviations: Cr, Creatine; DCSE, Dynamic Susceptibility Contrast Enhanced; DTI, Diffusion Tensor Imaging; FA, Fractional Anisotropy; GLCM, Gray-level co-occurrence matrix; GLRLM, Gray-level run-length matrix; MD, Mean Diffusivity; rCBV, relative Cerebral Blood Volume; p, pure isotropy; q, pure anisotropy;

4.1.4 Discussion

In the present study, radiomic analysis on a 3T mp-MRI dataset was performed for the classification between low- and high-grade gliomas. The specific implementation utilized a semi-automated clustering segmentation technique for delineating tumor core VOIs in all available MR parametric volumes, derived from structural MRI sequences (T1w-C, T2w-FSE, T2w-FLAIR), DTI (p, q, MD, FA,) and DSCE MRI raw data (maximum gadolinium uptake volumes). Subsequently, several quantitative histogram and textural features were calculated on each patient's parametric VOIs. Additional MRS metabolic ratios (NAA/Cr, Cho/Cr, mI/Cr and Lipids/Cr) and mean rCBV values, extracted from corresponding tumor VOIs, were considered, finally forming a set of 581 quantitative parameters (features) for each individual patient, which were inserted into the SVM-RFE in order to acquire feature ranking in a descending order of discriminative importance. Subsequently, comparisons performed between different SVM classifier implementations resulted in the adoption of linear kernel SMO classifier as the more efficient classification performance on our data set. The classification

model utilizing 21 mp-MRI radiomic features, demonstrated 95.5% Accuracy, 95% Sensitivity, 96% Specificity and 95.5% Area Under ROC Curve in differentiating LGG vs HGG.

The justification for implementing the specific SVM feature selection and classification methods on our mp-MRI dataset, is based on the predictive robustness indicated by similar studies regarding glioma grading in the past. In a computer-aided-diagnostic approach, Chen et al. (146) utilized SVM-RFE for selecting textural features, derived from CNN-based segments which were based on conventional MRI data only, and XGBoost classification, presenting a 91.27% accuracy. On the other hand, Citak-Er et al. (122) have proposed a sophisticated SVM-RFE implementation, in which different tumor ROIs mean values were analyzed with the addition of advanced techniques (1H-MRS, DSCE) but without a texture analysis approach as in our work. Their results utilizing the SVM-RFE outcome for training a linear SVM classifier yielded 93% classification accuracy. More importantly, Tian et al. (123) in a very recent study (2018), following their initial approach (141), proposed a multi parametric, MRI glioma grading classification scheme including advanced techniques such as ASL perfusion imaging, which was based on SVM-RFE and RBF kernelized SVM. Contrary to Citak-Er et al. (122), they have utilized a texture analysis approach similar to ours, showing 96% accuracy and 98% AUC values. Hence, it is evident that the addition of advanced MRI techniques and multiparametric texture analysis data, substantially improves the classification performance. In fact, when applying the same classification procedure in this data set, excluding the advanced quantitative parameters the performance dropped to 90% Accuracy, 90% Sensitivity, 97% Specificity and 89% AUC.

Even though Tian's et al. (123) study presents slightly better performance outcomes compared to our study, our model utilizes a significantly smaller number of radiomic features imported into the SVM classifier (21 vs. 28), increasing its relative efficiency. Since the two studies follow similar feature extraction, selection, and classification methodologies, it is obvious that our study's good performance should be attributed to the addition of the micro-

architectural and metabolic neuroimaging data utilized, i.e., Diffusion Tensor and Spectroscopic imaging, not included in Tian's et al. study. As it is depicted in Table 3, in our study an important number of features extracted from these techniques, have shown high discriminative ability, as this is already investigated and confirmed in previous studies (113,147).

More specifically DTI and MRS as additional quantitative parameters have already proven their ability in conventional analysis techniques. Regarding diffusion imaging, several previous studies have reported the value of textural features of Apparent Diffusion Coefficient (ADC) maps as potential biomarkers for glioma grade differentiation (105,106,148,149). In a more recent study, Raja et al. (150) investigated the contribution of Diffusion Tensor and Diffusion Kurtosis Imaging (DKI) in grading of gliomas. Their texture-based features have shown significant differences regarding several DTI parametric maps, except for FA, which comes in agreement with the results of our study. However, we have found that the anisotropic diffusion tensor component, as expressed by the pure anisotropy parameter (q) has proven to be of great importance (5 out of the 21 features were derived for q maps) and could play an essential role in glioma heterogeneity assessment.

In addition to DTI, MR spectroscopy is a powerful technique for evaluating brain tumor metabolic processes with an increased diagnostic impact. Many studies support the potential of MRS metabolic ratios in glioma grade differentiation (108,110,111,151), especially when combined with other advanced techniques. Even though a statistically significant difference for the specific ratios was not observed in our study, which might be expected since we are comparing HGGs vs LGGs (152), however the MRS derived Lipids/Cr ratio was the highest ranked feature compared to the total number of the radiomic features utilized. Consequently, the lipids concentration in glioma's tumor core, which is proportional to the extent of tumor's necrotic component, may serve as a robust imaging biomarker in differentiating between Low- and High-grade gliomas.

Perfusion imaging has evolved to a clinical tool of high importance in characterizing tumor malignancy status due to its increased correlation with cancer proliferation and progression. As shown in Table 3 a significant number of features imported to the classification model (7 out 21), are derived from perfusion MR techniques. These results come in agreement with previously reported studies (107,140), which insist that perfusion MRI may efficiently capture the intratumor heterogeneity, regarding angiogenesis and vascularity of gliomas. Also, according to the literature an additive value is obtained when radiomic analysis is employed on either conventional or advanced contrast enhancement techniques (102,103,104,153). However, as it has been previously reported (107) the 'hot spot' segmentation method that we utilized in CBV maps along with the subsequent inability for radiomic quantification, might have restricted the further contribution of the advanced DSCE imaging technique to the classification task. The recent technological advancements in the field of medical imaging have given rise to the incorporation of innovative methodologies regarding tumor phenotypic characteristics quantification and multiparametric data analysis which as shown by our results may aid in improving the clinical decision support process. Besides the current technical complexity challenges of radiomic analysis, further attention should be paid in utilizing the diagnostic outcome in a reliable manner (79). To this scope, it is evident that all methods of high-throughput analysis must consider well-established imaging techniques, which have been strongly validated upon various clinical hypotheses and underlying pathophysiology to guarantee their measurement accuracy and valid contribution. An equally important methodological step in such an analysis is to ensure that the involved medical personnel can ensure MR image quality, consistency, and accuracy by providing minimum quality standards in the inclusion or exclusion of the evaluated radiomic parameters.

The main limitation of this study regards to the small patient sample size utilized, which possibly would have implied bias to the advanced analysis that was conducted. In addition, the sample size limitation was the main reason for the exclusion of the gliomas sub-grades

differentiation task. In a future study of evaluating multiparametric MRI for glioma grade differentiation, it would be interesting to consider the inclusion of additional MR techniques with promising results (e.g., DKI, ASL). Also, except for MR modalities, an investigation of additional shape and textural radiomic features and genomic data (i.e., IDH mutation, etc) should be performed, to further assess their utility.

4.1.5 Conclusion

In conclusion, the current study presents a comprehensive methodological perspective for evaluating MRI derived phenotypic characteristics for LGG vs HGG characterization, based on multiparametric MR neuroimaging data and radiomic analysis methods. It shows that radiomic features derived from mp-MRI can be an important tool in an accurate LGG vs HGG differentiation even in this limited patient population.

this page intentionally left blank

Chapter 5

5.1 Evaluation of 3T multiparametric MRI with radiomic analysis for differentiating benign and malignant breast lesions

5.1.1 Aims and Objectives

Female breast cancer was the leading cause of global cancer incidence in 2020 and the fifth in cancer mortality rates among both sexes worldwide (154). Over the past decades effective breast cancer prognosis and patients' survival rates have increased due to the improvements and availability of innovative screening technologies (155). MRI of the breast has emerged as an exceptionally powerful technique, with increased sensitivity in breast cancer detection, even compared to mammography and ultrasonography (156). Additionally, the simultaneous evaluation of different MRI sequences, such as Dynamic Contrast Enhance (DCE) and DWI, referred here as mpMRI, can be used to assess a multitude of morphological and functional cancer-related processes, related to breast tumor development, progression, and response to treatment (157). Currently, mpMRI has a pivotal role in differentiating benign and malignant breast lesions that present highly overlapping enhancement patterns, non-invasively (156). However, despite the potential to obviate unnecessary biopsies and follow-up examinations of benign tumors, mpMRI-based breast tumor differentiation still has increased false positive findings (158).

Breast MRI diagnosis has been further enriched by computer-aided image analysis, to assist the radiologists in leveraging the substantial quantitative imaging information and assessing tumor profile (159). The spread of "-omics" strategies has provided a novel conceptual framework, termed Radiomics, aiming at the extraction of immense numbers of imaging features, that can serve as imaging biomarkers. Especially, when coupled with sophisticated supervised ML algorithms, these data can be used to construct clinically significant diagnostic and predictive models for assisting personalized care of oncologic patients (160,161).

In this context, a few previous studies have developed radiomic models with SVM for classifying breast tumors in mpMRI datasets, demonstrating high predictive efficiencies in terms of AUC, ranging from 0.85 to 0.92 (162,163,164,165). In another study (166), four different classification algorithms, i.e., SVM, Naïve Bayes, k-Nearest Neighbours, and Logistic Regression, were evaluated, demonstrating comparable performances with an average AUC=0.93. Recently, a newly designed classification model, the difference-weighted local hyperplane has been proposed (167), that have shown a performance of AUC=0.90 in differentiating benign vs malignant lesions. Although very promising, the difficulty in collecting mpMRI datasets of adequate size, as well as the inherent complexity of mpMRI biomarkers, are hampering the capabilities of the proposed models, in terms of performance and generalizability.

Recently, Ensemble Learning methods that combine the predictions of multiple classifiers to reach better performance than a single estimator does, have gained interest in radiomics research (168). These strategies have proven very useful in modelling heterogeneous datasets of any size and complexity (160), while also excel at trading off the approximation and estimation errors compared to the more conventional ML approaches (169). Particularly, Boosting Ensemble Classifiers have shown to outperform other classification techniques within breast mpMRI radiomics, for molecular subtypes recognition (170,171), prediction of sentinel lymph node metastasis (172), and early prediction of treatment response and survival outcomes

(173). Additionally, their predictive efficiency for differentiating benign from malignant breast lesions has shown promise within DCE MRI radiomics alone in a recent study (AUC=0.96) (174), but this have not yet been evaluated within mpMRI datasets.

The current study sought to investigate the optimization of the aforementioned radiomics approaches in terms of evaluating the performance of four popular implementations of Decision Trees (DT) Boosting classifiers, namely Adaptive Boosting (AdaBoost) (175), Gradient Boosting (GB) (176), Extreme Gradient Boosting (XGBoost) (177) and Light Gradient Boosting Machine (LightGBM) (178), for breast cancer classification with mp-MRI radiomic features. A feature selection process based on the Boruta algorithm, Hierarchical Clustering (HC) on Spearman's rank correlation coefficients between features and RF classification was adopted, for determining all relevant and non-redundant feature subset, to improve the diagnostic efficiency of the classification models. For reference, an SVM classifier was also trained and evaluated on the same feature subset to allow performance comparisons, since this algorithm represents the current state-of-the-art ML method in breast mpMRI diagnostic radiomic models. To our knowledge this is the first study presenting the value of Ensemble Learning methods within multiparametric MRI radiomics for breast cancer classification.

5.1.2 Material and Methods

Patient Cohort and MRI acquisition

The reporting of this study conforms to the STROBE checklist (179), according to the relevant Equator Network reporting guidelines (https://www.equator-network.org/reporting-guidelines/). This retrospective study was granted approval by the Internal Ethics Committee of the Department of Medicine of the University of Thessaly (approval number: 195). A sample of breast MRI data was obtained from a cohort of 293 female patients that have been

consecutively examined in our institution the past five years and gave written informed consent for their participation in the study. The inclusion criteria were mass-like lesions detected on mammography and/or ultrasonography prior to any type of biopsy, with histological status verification from core needle biopsy or surgical excision, that was considered as the gold-standard of diagnosis. The exclusion criteria for this study were receiving of neoadjuvant chemotherapy or radiation therapy, pregnancy/breastfeeding, presence of any implants or metallic clips from previous surgical procedures and general contraindications to MRI scanning or to the administration of contrast agents. Breast lesions with a maximum diameter less than 1.0 cm in any direction were also excluded to reduce potential bias in radiomic feature measurements.

MR images were acquired on a 3.0 T MRI scanner (GE Healthcare, Signa HDx, Milwaukee, WI, USA) with patients placed in the prone position, using a dedicated phased array 8-channel breast coil. All patients underwent the same imaging protocol including conventional breast MRI with DCE and DWI. Each conventional MRI examination included scanning of the two breasts. Breast DCE-MRI protocol consisted of an axial T2-w FSE sequence (T2-FSE), ((TR/TE) = 3600/100 ms, flip angle=90°, matrix size = 512x512, slice thickness=4.0 mm), an axial Short Tau Inversion Recovery sequence (STIR), (TR/TE=3900/90 ms, flip angle=90°, matrix size = 512x512, slice thickness=4.0 mm), and a 3D T1-w VIBRANT dynamic sequence with fat-suppression (TR/TE = 4.94/2.1 ms, flip angle = 10°, matrix size = 512x512, isotropic voxel size of 1 mm^3) which was applied before and five times after the intravenous (IV) injection of a Gadolinium-based contrast agent with a 10 second timing delay, using an automatic injector system. The DWI protocol consisted of a DWI sequence which was acquired before injection of the contrast medium (TR/TE = 6000 ms/90 ms, flip angle = 90°, matrix size = 256x256, slice thickness = 4.0 mm, and b-values of 0 and 850 s/mm^2).

Image post-acquisition processing and Feature Extraction

The DCE-MRI volumes that were acquired 2-3 minutes after contrast agent administration and present the maximum enhancement between the different post-contrast time frames, were included in the analysis. ADC maps were calculated the from DWI images with two b-values (0 and 850 s/mm^2) using the mono-exponential model fitting. Tumor contours in all consecutive slices in the three parametric datasets (DCE, T2-w, ADC), were manually drawn by a radiologist (20 years of experience), and the corresponding 3D volume masks of tumor masses were generated. Since the precision in tumor contouring may crucially affect the radiomic analysis, a second radiologist (23 years of experience) was recruited to provide independent segments for validation. The Dice coefficient implemented with an in-house python code was used to assess overlapping between segments. In case of segments with poor overlapping (Dice<0.85) a consensus between the two radiologists was reached for standardizing the delineation.

Radiomic feature extraction was implemented in Python 3.6 with the Pyradiomics library (100) which complies with the Imaging Biomarkers Standardization Initiative guidelines (IBSI) (180). Prior to feature extraction, outliers from pixel values distributions, as determined by the μ±3σ criterion, were excluded. Radiomic feature extraction was applied on the original parametric images without any filtering and 19 3D Shape-based, 16 First Order Statistics, 10 GLCM, 24 GLRLM, 16 Gray Level Size Zone Matrix (GLSZM), 5 Neighbouring Gray Tone Difference Matrix (NGTDM) and 14 Gray Level Dependence Matrix (GLDM) features were calculated, resulting in a total of 293 features for the whole imaging set of each subject. Since shape features' calculation relies solely on imaging information of tumor margins and are independent of the whole tumor voxel intensity histogram, the extraction of shape features was applied only in DCE-MRI sequence, that presents an isotropic pixel spacing acquisition. In this way, we avoided to include redundant and misleading information regarding the tumor shape in the analysis. Additionally, the calculation of texture features utilized histogram binning with

a fixed bin count of 64 bits-per-pixel for GLCM, GLDM, GLRLM and GLSZM features, and 32 bits-per-pixel for NGTDM features according to the Pyradiomics guidelines.

Statistical Analyses

A filter-based method was utilized to identify and exclude the non-informative features by assessing their individual discriminatory power. Specifically, univariate parametric (Student's t-test) or non-parametric (Mann-Whitney U-test) statistical tests (a=0.05) were applied on each feature separately to assess statistically significantly differences between the corresponding distributions of benign and malignant cases. The selection of the appropriate statistical test was made according to the outcome of the Shapiro-Wilk test for normality (a=0.05). With this filter-based approach we achieved to reduce the dimensionality of the initial feature space to increase the efficiency of the subsequent selection algorithm. A z-score transformation was applied to the remaining features, to standardize their values on the same scale.

Feature Selection

Feature selection processes were implemented in Python 3.6 using numpy [https://numpy.org], scipy [https://scipy.org], and scikit-learn [https://scikit-learn.org] libraries, and the Boruta_py package obtained from [https://github.com/scikit-learn-contrib/boruta_py]. The graphics were generated with the matplotlib library (181).

The Boruta algorithm which is a wrapper method around a RF classifier was implemented for the feature selection process (182). In principle, the Boruta method, generates artificial features by shuffling the original feature values across subjects. The original and artificial features are combined and evaluated with the RF classifier. Finally, the importance of artificial features is used as reference for selecting original features according to the RF permutation importance measure. By default, the Boruta algorithm generates two subsets of relevant

features, one presenting high and the other intermediate importance, respectively. Here, only the subset of highly important features was kept for further analysis. However, as is the case with the most wrapper feature selection techniques, Boruta does not handle feature multicollinearity, thus redundant information tends to be present in the final subset, and this might compromise the subsequent classification performance. Two previous studies have utilized additional steps of collinearity analysis to identify and exclude redundant features (183,184). In the specific implementation adopted here, HC with Ward's linkage method was applied to a cross-correlation matrix of Spearman's rank correlation coefficients, between the highly important features selected with Boruta. In each cluster of features with high dependency, defined as those having Spearman rho values above 0.6, a new RF classifier was applied to rank the within-cluster feature importance, according to the RF Gini's Index. The most important feature per cluster was retained to form the final feature subset.

Classification Modelling and Evaluation

Python implementations for XGBoost and LightGBM were obtained from their original sources [https://github.com/dmlc/xgboost], [https://github.com/microsoft/LightGBM] and used through the scikit-learn Application Programming Interface (API), which is a common framework for ML applications (185).

The final feature subset was used to train the GB, AdaBoost, XGBoost, LightGBM and SVM classifiers in differentiating benign from malignant breast lesions. All four boosting classification algorithms have shared the same hyperparameters, i.e., number of trees = 1000, max depth = 3, learning rate = 0.1 and the 'early stopping' option enabled. SVM classifier was built with scikit-learn library default hyperparameters, i.e., Radial Basis Kernel, 'scale' option for kernel coefficient gamma, and regularization parameter C=1. The '.632+ bootstrap' validation method (186) as implemented in mlxtend python package (http://rasbt.github.io/mlxtend/) and ROC analysis were employed to validate the models'

performance and obtain the AUC evaluation metric. The resulting classification scores of Acc, Se, Sp and AUC were averaged across 300 bootstraps. Additionally, the DeLong's test was utilized to identify pairwise statistically significant differences between the AUC values of the models (187). The complete workflow of the radiomic analysis implemented in this study is presented in Figure 18.

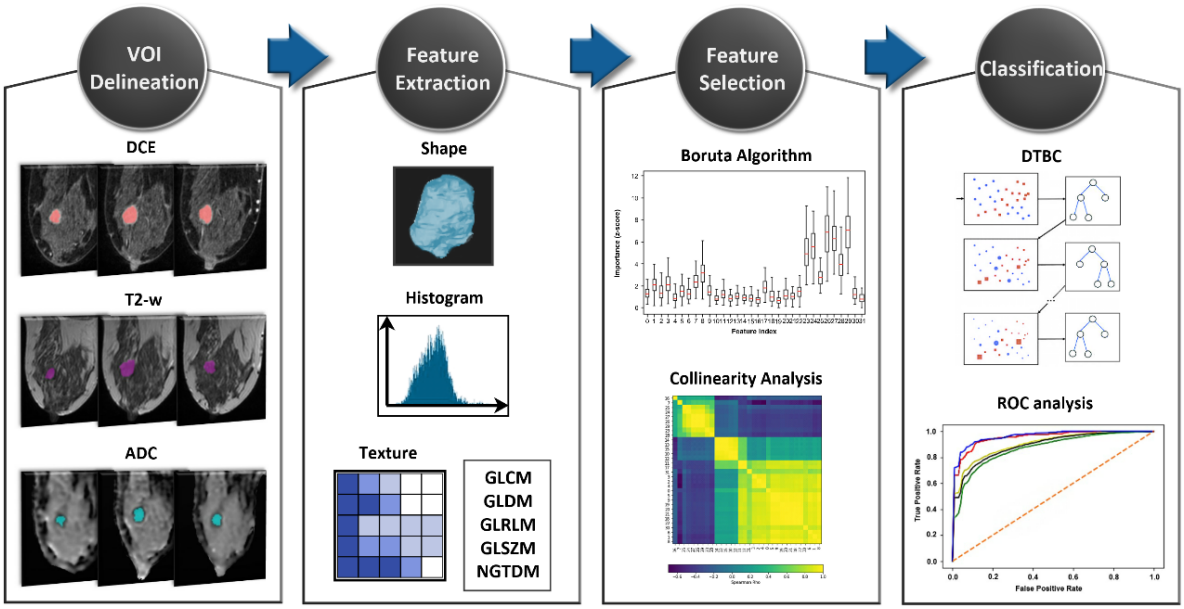

Figure 18: The radiomic analysis workflow.

5.1.3 Results

From the initially available patient cohort, a sample of 140 patients with all required data available that also met the inclusion criteria, was included, as shown in the flow diagram (Figure 19). In case where multiple lesions were present in the same or the opposite breast, only a single lesion per subject was selected, finally conforming a balanced dataset of 70 benign and 70 malignant lesions that was considered for the analysis.

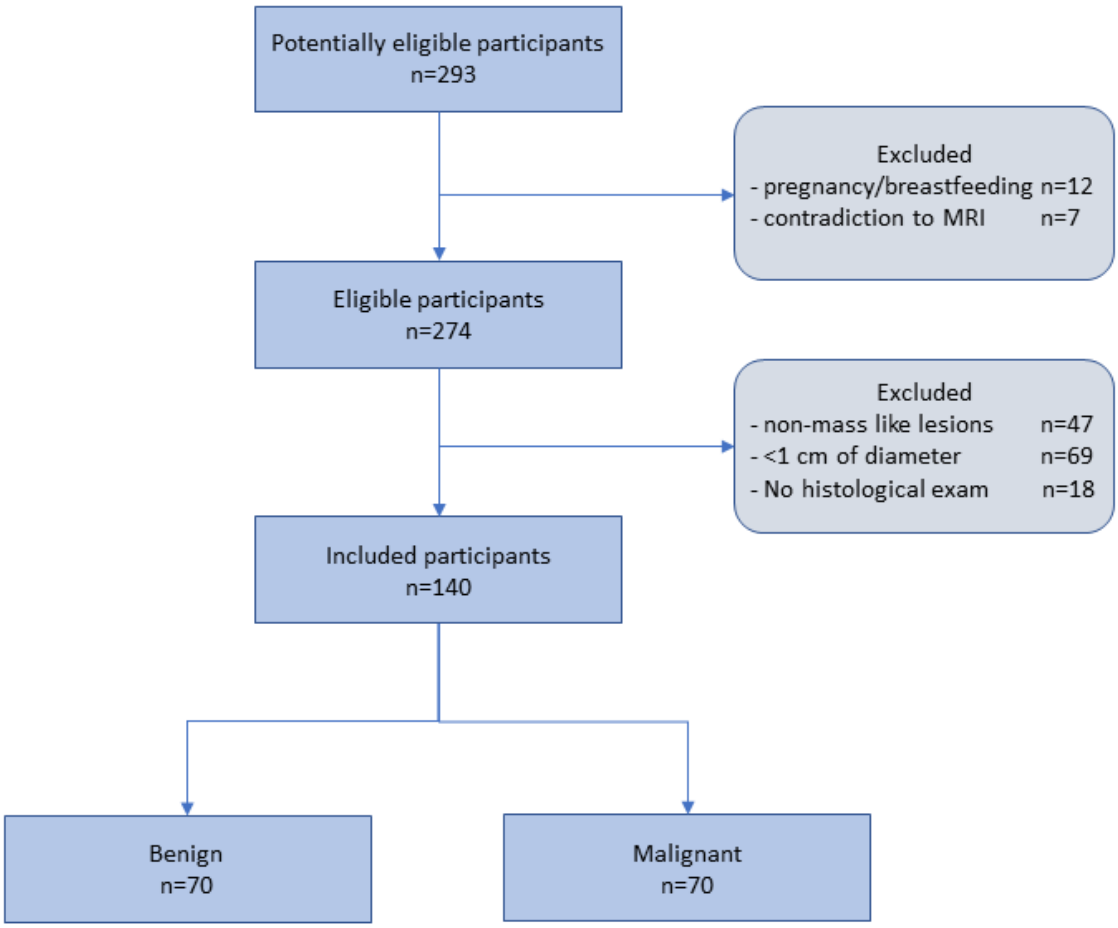

Figure 19: Flow diagram of the study participants selection.

Demographic and clinical characteristics of the sample utilized are presented in Table 5. Specifically, the mean age was 44.6 ± 11.8 for the benign and 57.4 ± 12.5 for the malignant cases. The mean volume size was 1.8 ± 1.6 cm3 and 4.0 ± 2.4 cm3 for benign and malignant lesions, respectively. Benign lesions were of type Fibroadenomas according to the histopathology examination. The radiologic assessment had assigned 48/70 lesions to type 2, 19/70 to type 3 and 3/70 to type 4 according to BI-RADS categorization of the American College of Radiology (ACR) (188). The malignant lesion sample consisted of 53 Invasive Ductal Carcinomas (IDCs,) 12 Invasive Lobular Carcinomas (ILCs), 4 Ductal Carcinoma In-Situ (DCIS) and 1 Lobular Carcinoma In-Situ (LCIS), while 10/70 were found to be of histological grade I, 39/70 of histological grade II and 21/70 of histological grade III.

Table 5: Demographic and clinical characteristics of the patient sample

	Benign	Malignant
Patients (N)	70 females (50%)	70 females (50%)
Lesions (N)	70 (50%)	70 (50%)
Age (mean ± std)	44.6 ± 11.8	57.4 ± 12.5
Volume in cm^3 (mean ± std)	1.8 ± 1.6	4.0 ± 2.4
Histological type (N)		
FA	70 (100%)	
IDC		53 (76%)
ILC		12 (17%)
DCIS		4 (6%)
LCIS		1 (1%)
Histological grade		
I		10 (14%)
II		39 (56%)
III		21 (30%)
MRI BI-RADS categories		
2	48 (69%)	
3	19 (27%)	
4	3 (4%)	14 (20%)
5		56 (80%)

Abbreviations: FA, Fibroadenoma; IDC, Invasive Ductal Carcinoma; ILC, Invasive Lobular Carcinoma; DCIS, Ductal Carcinoma In-Situ; LCIS, Lobular Carcinoma In-Situ

The radiologic assessment had assigned 14/70 and 56/70 to MRI BI-RADS categories 4 and 5, respectively.

Manual segmentations of the lesions had presented a high overlapping among the two radiologists (raters), denoted by an average Dice coefficient of 0.88±0.09.

The parametric and non-parametric statistical tests have revealed 82 out of 293 total features to be non-informative ($p>0.05$) and these were excluded from the analysis. Out of the remaining 211 features, the Boruta algorithm have nominated 32 highly important features, i.e., 10 from shape, 8 from DCE histogram, 5 from DCE texture, 8 from ADC histogram and 1 from ADC texture presented in Table 6.

Interestingly, we observed that T2-w based features were totally absent from this highly important feature subset, while ADC histogram features were the most important among the

remaining features (z-scores = 1.3±0.60 – 7.0±2.00). Figure 20 presents boxplots of each feature's importance (z-score) distribution obtained from the RF permutations.

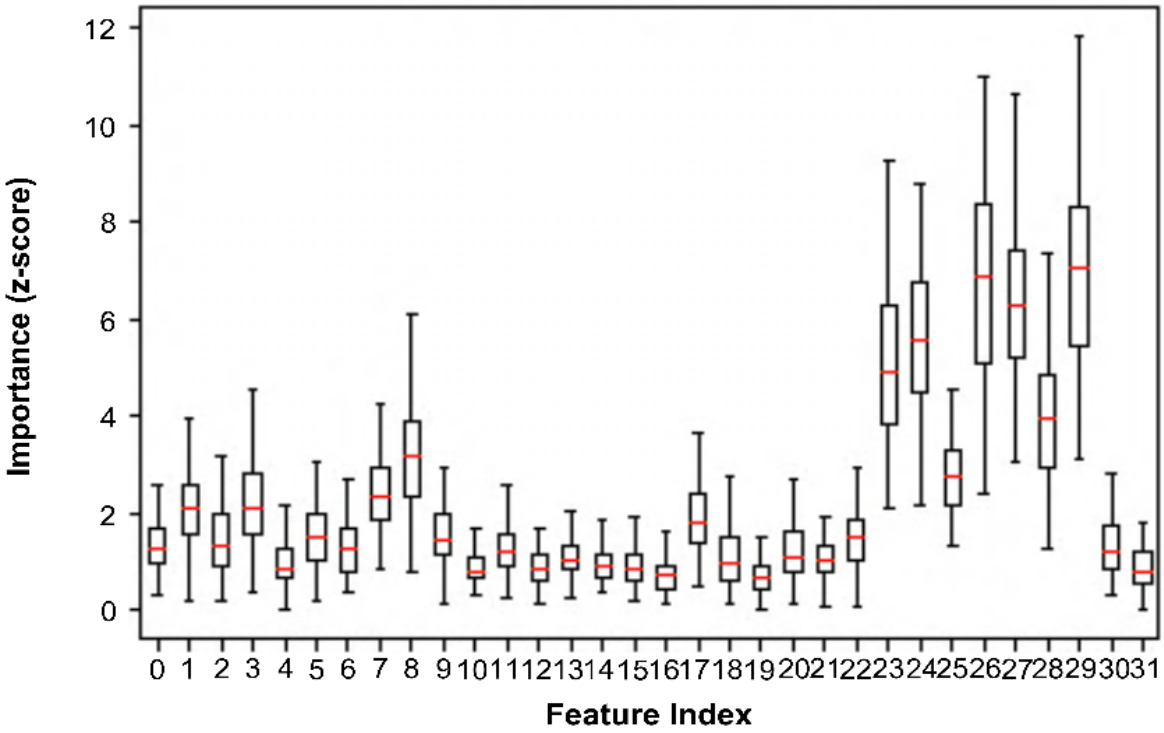

Figure 20: Feature importance in terms of z-score distributions of RF permutations for the highly important feature subset nominated by Boruta.

Table 6: Boruta selected features

Index	Feature name	Importance (mean±std)
0	original_shape_LeastAxisLength	1.43±0.76
1	original_shape_Maximum2DDiameterColumn	2.14±0.80
2	original_shape_Maximum2DDiameterRow	1.52±0.82
3	original_shape_Maximum2DDiameterSlice	2.22±1.10
4	original_shape_Maximum3DDiameter	0.94±0.54
5	original_shape_MeshVolume	1.65±0.63
6	original_shape_MinorAxisLength	1.38±0.58
7	original_shape_Sphericity	2.46±0.72
8	original_shape_SurfaceArea	3.51±1.37
9	original_shape_VoxelVolume	1.50±0.58
10	DCE_original_firstorder_90Percentile	0.82±0.36
11	DCE_original_firstorder_Energy	1.33±0.61
12	DCE_original_firstorder_Maximum	0.89±0.40
13	DCE_original_firstorder_Mean	0.94±0.44
14	DCE_original_firstorder_Median	0.90±0.37
15	DCE_original_firstorder_RootMeanSquared	0.87±0.43
16	DCE_original_firstorder_Skewness	0.72±0.35
17	DCE_original_firstorder_TotalEnergy	1.81±0.70
18	DCE_original_gldm_DependenceNonUniformity	1.06±0.58
19	DCE_original_glrlm_GrayLevelNonUniformity	0.70±0.44
20	DCE_original_glrlm_RunLengthNonUniformity	1.35±0.60
21	DCE_original_glszm_GrayLevelNonUniformity	1.12±0.48
22	DCE_original_glszm_SizeZoneNonUniformity	1.55±0.49
23	ADC_original_firstorder_10Percentile	4.91±1.75
24	ADC_original_firstorder_90Percentile	5.36±1.58
25	ADC_original_firstorder_Maximum	2.74±0.87
26	ADC_original_firstorder_Mean	6.65±2.18
27	ADC_original_firstorder_Median	6.22±1.59
28	ADC_original_firstorder_Minimum	3.86±1.41
29	ADC_original_firstorder_RootMeanSquared	7.10±1.98
30	ADC_original_firstorder_TotalEnergy	1.26±0.59
31	ADC_original_ngtdm_Busyness	0.67±0.45

Abbreviations: DCE, Dynamic Contrast Enhanced; ADC, Apparent Diffusion Coefficient; std, standard deviation

The pairwise Spearman's rank correlation coefficients have revealed several statistical dependencies (rho=0.60 to 0.98), especially between shape and texture features of DCE and DWI (Figure 21). Histogram features have shown smaller correlation values with either shape or textural features. The second step of Boruta selected subsets elimination with HC and RF importance resulted in the determination of a minimum subset, consisting of 5 features, namely Sphericity, Surface Area, DCE_median, DCE_skewness, ADC_mean.

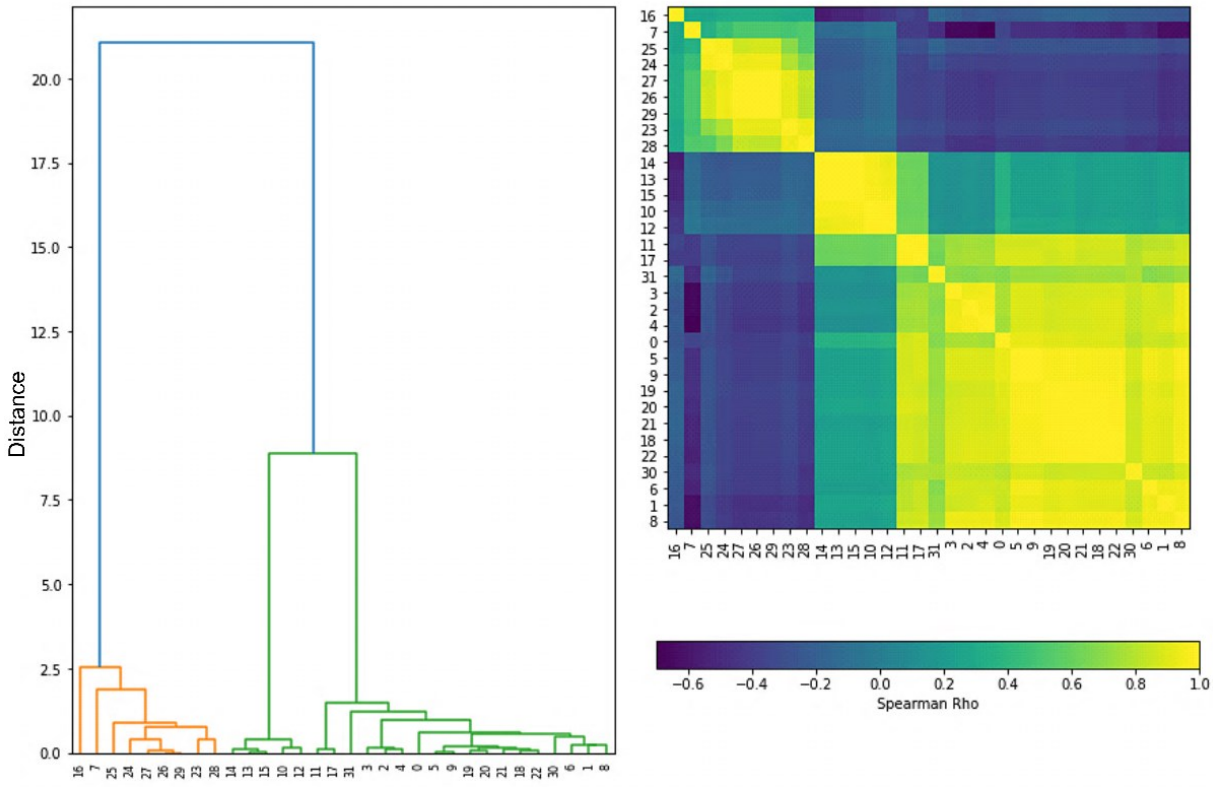

Figure 21: The Hierarchical Clustering dendrogram (a) illustrating clusters arrangement as informed by the correlation plot (b) of Boruta selected features.

Average classification metrics of the different models, in terms of mean and 95% Confidence Intervals (CI) across the bootstrap validation subsamples, are presented in Table 7. Regarding Boosting Ensemble methods, it was observed that XGboost achieved the highest accuracy (Acc=0.88 [95% CI 0.84-0.92]) and overall performance (AUC=0.95 [95% CI 0.91-0.99]) followed by LGBM (Acc=0.87 [95% CI 0.83-0.91]/ AUC=0.94 [95% CI 0.90-0.98]), Adaboost (Acc=0.83 [95% CI 0.80-0.86] / AUC=0.90 [95% CI 0.87-0.93]), and GB (Acc=0.83 [95% CI 0.80-0.86] / AUC=0.89 [95% CI 0.86-0.92]). According to the pairwise statistical comparisons that were performed between the AUC values (Table 8), the observed interindividual differences in overall performances of XGBoost and LGBM were statistically significantly higher than AdaBoost and GB. The SVM classification model has yielded statistically significantly lower performance (Acc=0.84 [95% CI 0.80-0.88] / AUC=0.88 [95% CI 0.84-0.92]) than XGBoost and LGBM, but this was found statistically comparable with the performances demonstrated by AdaBoost and GB (Table 8). XGBoost has also achieved the highest sensitivity (Se=0.91 [95% CI 0.85-0.97]) and specificity (Sp=0.90 [95% CI 0.82-0.98]). Sensitivity and specificity metrics for the rest of the classification models were: LGBM Se=0.90 [95% CI 0.84-0.96] / Sp=0.89 [95% CI 0.81-0.97], AdaBoost Se=0.83 [95% CI 0.78-0.88] / Sp=0.82 [95% CI 0.75-0.89], GB Se=0.82 [95% CI 0.77-0.87] / Sp=0.80 [95% CI 0.73-0.87], SVM Se=0.80 [95% CI 0.77-0.88] / Sp=79 [95% CI 0.70-0.88]. Figure 22 presents the ROC curves plots of the classification models.

Table 7: Classification model results (mean [95% CI])

	XGBoost	LGBM	AdaBoost	GB	SVM
Acc	0.88 [0.84-0.92]	0.87 [0.83-0.91]	0.83 [0.80-0.86]	0.83 [0.80-0.86]	0.84 [0.80-0.88]
Se	0.91 [0.85-0.97]	0.90 [0.84-0.96]	0.83 [0.78-0.88]	0.82 [0.77-0.87]	0.80 [0.77-0.88]
Sp	0.90 [0.82-0.98]	0.89 [0.81-0.97]	0.82 [0.75-0.89]	0.80 [0.73-0.87]	0.79 [0.70-0.88]
AUC	0.95 [0.91-0.99]	0.94 [0.90-0.98]	0.90 [0.87-0.93]	0.89 [0.86-0.92]	0.88 [0.84-0.92]

Abbreviations: Acc, Accuracy; AUC, Area Under Curve; Se, Sensitivity, Sp, Specificity

Table 8: p-values of the pairwise statistical comparisons of the classification models AUC values derived from DeLong's test.

	XGBoost	LGBM	AdaBoost	GB	SVM
XGBoost		0.77	0.029	0.022	0.017
LGBM			0.032	0.026	0.020
AdaBoost				0.93	0.71
GB					0.81
SVM					

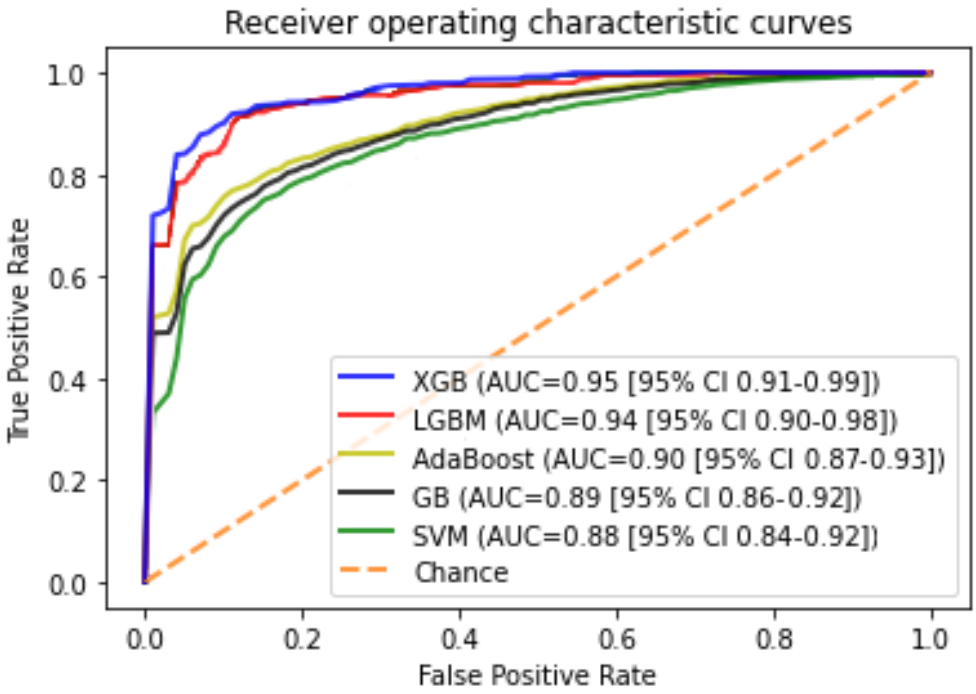

Figure 22: Receiver operating characteristic (ROC) curves of the classification models.

5.1.4 Discussion

In this study we investigate the utility of a novel radiomic analysis pipeline, based on Ensemble Learning, for increasing the mpMRI predictive capability towards differentiation of benign and malignant breast lesions. A feature selection process, based on Random Forest classification with the Boruta wrapper and hierarchical clustering on Spearman's rank correlation coefficients has nominated 5 radiomic features from shape, DCE and DWI as being the most important for breast cancer differentiation. Four DT Boosting Ensembles were evaluated with bootstrapping validation and their performances were compared with an SVM classification model. XGBoost and LGBM achieved statistically significantly higher AUC values, compared to the performances of the rest of the methods. Overall, this study provides novel evidence regarding the robustness of the newer implementations of Boosting ensemble classification methods, which hold potential to enhance breast cancer precision medicine with minimum invasive approaches.

Differentiation of benign and malignant breast lesions is an important step for breast cancer management, since it determines the therapeutic plan that the clinicians will follow, ranging from active surveillance to chemotherapy/radiotherapy and tumor excision (155). MRI of the breast has been increasingly recognized as a powerful diagnostic tool. The American College of Radiology has established the BI-RADS MRI lexicon that provides standardized assessment and reporting of MRI findings and a classification system to determine the probability of malignancy and biopsy recommendations. Currently, MRI BI-RADS incorporates morphological and functional descriptors for DCE-MRI and T2-w, which constitute the typical MRI protocol (156). However, due to an overlap in imaging descriptors between benign and malignant tumors the standard MRI protocol presents moderate specificity, thus many BI-RADS 4 and 5 biopsies might be misdiagnosed (158). Notably, the incorporation of DWI ADC mapping has been shown to significantly improve specificity which may reduce unnecessary biopsies and invasive diagnostic procedures (189). In a recent meta-analysis of 22 studies, it was shown that the pooled specificity increased to 0.85 with the inclusion of DWI parameters compared to the pooled specificity of 0.71 for the DCE-MRI alone (190).

Previous studies have demonstrated that breast mpMRI radiomic features, representing a quantitative description of a specific geometrical or physical property of the image, hold great potential for overcoming the caveats of the subjective qualitative radiologic assessment (191). Indeed, these features derived from tumor shape, texture, kinetics, etc, encode both simple patterns within medical images but also many higher order patterns not apparent to the human eye (192). More importantly, radiomic features can be input to supervised machine learning models that hold diagnostic and predictive power for automating the quantitative evaluation towards further reduction of the false positive findings (165,193). However, not all of the extracted features are important, therefore a feature selection technique is needed within radiomics analysis to determine the most tumor subtype discriminative and biologically relevant features to construct robust classification models (161).

In this study we have used Boruta, which is a wrapper algorithm around a Random Forest classifier. The highly important feature subset nominated by Boruta consisted of shape, histogram and textural features from DCE and ADC. Notably, ADC features were the most important for the specific classification task, while none of T2-w features were found to participate in the selected subset. We consider this an important finding, in line with previous evidence expanding the findings of conventional evaluation to radiomic analysis, where quantitative measurements of ADC maps were reported to have more impact on classification performance than those of T2-w (165,194). Generally, Boruta has proven to be the most robust all-relevant feature selection strategy in gene selection (195), while very recently this algorithm has been successfully used in radiomics studies (183,184), but not yet in breast MRI diagnosis. Additionally, in a recent radiogenomics study (196) it was shown to outperform other robust feature selection ensemble methods, such as the Minimum Redundancy Maximum Relevance (MRMR) algorithm.

Since Boruta is an all-relevant feature selection method, we additionally implemented steps of Hierarchical Clustering on Spearman's rank correlation coefficients and Random Forest classification as published elsewhere (183,184), to exclude redundant features and form the final feature subset for classification. Interestingly, shape features were found highly correlated with texture features and outperformed them, thus, only shape and 1st order histogram features were included in the final subset.

Boosting models' training with the specific radiomic signature have demonstrated high performances of XGBoost (AUC=0.95) and LGBM (AUC=0.94) algorithms in benign vs malignant breast lesions differentiation. Of note, the AUC values between the two models were not found statistically different, however, despite the apparent algorithmic similarities, these models may present substantial variations in classification accuracy, as well as processing time, in larger datasets (178). Adaboost and GB were found to have significantly lower AUC values of 0.90 and 0.89, respectively. Generally, these findings come in agreement with a growing

body of recent literature, suggesting the unique efficiency of Boosting ensembles either for classifying conventional radiomic features (190,191), imaging features extracted from Convolutional Neural Networks (CNN) (173,197), or both (198). Additionally, they are adding more credence to the existing reports within various breast MRI radiomics paradigms (170,171,172,173). Regarding breast MRI diagnosis, in a previously proposed CADx based on ensemble methods for feature selection and classification, AdaBoost has achieved a high performance (AUC=0.96) in differentiating malignant and benign lesions by means of DCE MRI radiomic features (174). Beyond the exploitation of ensemble learning methods, the authors have also made use of wavelet features. As it was previously demonstrated, the wavelet transformation of medical images holds potential for capturing various spatial frequency texture patterns within heterogeneous breast lesion regions (199). This might partially explain the high performance observed in their study, although the model was evaluated on DCE-MRI alone and utilized the AdaBoost algorithm which has achieved a significantly lower performance in our study. Besides, the additional use of the DWI sequence in our study has resulted in the adoption of a minimum set of clinically perceivable radiomic features which facilitates the enhanced interpretability of the specific diagnostic model.

Additionally, XGBoost and LGBM models were found to outperform the SVM classifier (AUC=0.88), which has been a commonly utilized ML classification strategy in breast MRI radiomics. Specifically, in the studies of Damiel Naranjo et al. (162), Parekh et al. (163) and Hu et al. (164), SVM classifiers were utilized to differentiate breast lesions over mpMRI datasets consisting of DCE, DWI and T2-w images, with all models achieving similar performances of AUC=0.85, AUC=0.87 and AUC=0.87, respectively. Cai et al. (166) have compared four different classification algorithms, i.e., SVM, Naïve Bayes, k-Nearest Neighbours, and Logistic Regression. SVM has demonstrated a high performance (AUC = 0.91), although this was not found significantly different from the other classifiers utilized in their study. Further evidence regarding SVM capability for breast cancer diagnosis has been

presented by Zhang et al. (165), where their model achieved a performance of 0.92. However, it is worth to mention that the authors have utilized advanced pharmacokinetic parameters of DCE MRI and Diffusion Kurtosis Imaging (DKI) in their radiomic signature, while in the present study a more conventional mpMRI protocol was available, and thus we might didn't observed such a high performance for the SVM model. Considering the above-mentioned findings and with respect to any particular methodological differences between the studies, it is evident that ensemble learning classification holds great potential for overcoming the limited efficacy of conventional ML models towards increasing the breast mpMRI diagnostic accuracy.

Our study has some limitations. Specifically, only one mpMRI dataset of restricted size was available to train and test our classification models, while an additional external independent validation dataset would allow to evaluate their generalization on new 'unseen' data. Additionally, no power calculation for estimating the sample size selected for the study was done. Since this was an exploratory analysis investigating the utility of Boosting algorithms in breast cancer classification, reproducibility analysis of segmentation and feature extraction procedures was not performed. Furthermore, due to the abbreviated nature of the mpMRI protocol in our institution, the inclusion of DCE kinetic features or other MRI sequences (e.g., Diffusion Tensor Imaging, Diffusion Kurtosis Imaging, MR Spectroscopy, etc), previously demonstrated to have a significant impact in breast cancer diagnosis (8,200,201), was not feasible.

5.1.5 Conclusion

In conclusion, mpMRI of the breast holds potential for accurate differentiation of benign and malignant breast lesions, to reduce invasive diagnostic procedures. The integration of Ensemble Learning methods within mpMRI radiomics could provide valuable precise quantification of the diagnostic information and identify while reducing the subjective reader interpretation errors.

PART C

General Discussion

this page intentionally left blank

Chapter 6

6.1 Discussion of studies' findings, challenges, and future considerations

The present doctoral research investigates the clinical benefit arising from the exploitation of multiparametric imaging, through studying several MRI applications of neurologic and oncologic interest. In this context, particular focus been given on the evaluation of novel analytic methodologies that aim to enhance the data-driven interpretation regarding the clinical associations of the quantitative imaging parameters, towards supporting the non-invasive and personalized characterization of pathological conditions.

The first study aimed to evaluate the utility of a spatial correlation approach for enhancing the molecular information obtained from fMRI signals, in terms of assessing the spatial correlation between the observed hemodynamic responses and various neurotransmitters receptor systems. The methodology benefits from the use of normative PET and/or mRNA expression data obtained from independent studies that inform receptor distribution, overcoming the constrains of on-site PET implementation for directly monitoring neurotransmitter dynamics. The proposed methodology has been efficiently used to map hemodynamic changes induced by compounds onto their target receptor cites. Although providing very important evidence, these proof-of-concept correlations are facilitated by the fact that the corresponding pharmacological interventions studies, minimize the range of the neurotransmitters engaged into the study, while the dosage incretion can induce very distinct fMRI signals. However, until recently the methodology's value to inform molecular substrates

of fMRI signal in the context of endogenous neurotransmitter release remained unexplored. To this scope the ongoing pain paradigm was selected, as this is of great clinical interest, while it is a partially studied field, by means of BOLD fMRI/PET, with sufficient previous evidence.

Specifically, previous studies have showed the potential of ASL in advancing our understanding regarding brain function alterations in ongoing pain. However, the link between the observed hemodynamic changes and the underlying neurobiological processes remains unclear. The present study presents important evidence regarding the link between pain-related, ASL-derived CBF signals with two crucial components of pain processing, the opioidergic and dopaminergic systems. These biologically validated findings highlight the significant utility of the current approach as a low-risk low-cost hypothesis generating tool that benefits from existing PET and transcriptomic datasets to bridge the translational gap between the advancing knowledge gained from MRI and the neurotransmitters systems that underlying painful experiences.

Multimodal imaging and transcriptomics spatial correlation analysis help inform future investigation of the molecular mechanisms which may show functionally relevant disruption in acute and chronic pain conditions, as well as modulation by treatment. However, it should be noted that the applicability of such approaches is generally limited by the availability of PET normative maps, thus more efforts should be made in a multi-institutional level to study appropriate radioligands and produce more maps covering a wide range of neurotransmitter receptors. Our study has also shown the significant utility of ABA in utilizing transcriptomics to inform receptor distribution. In this context novel data e.g., next-generation RNA sequencing is expected to form a more concrete database of mRNA expressions, as well as to improve statistical power currently compromised by ABA small sample size of donors (5). Additionally, novel statistical frameworks for overcoming current limitations of the spatial correlation analysis of multimodal signals are needed. Of note, more advanced statistical analyses are being used with BOLD fMRI signals, e.g., the REACT method (18), however such techniques are not

suitable for ASL MRI signals. The point of novel methods developed should be the strengthening of more fine grain spatial sampling of the imaging data, i.e., to include more regions of interest, or even to perform analysis in a voxel-wise level. The spatial autocorrelation issue should also gain attention of future studies, in the direction of utilizing both cortical and subcortical areas in the analysis.

The second study aimed to develop a radiomic analysis model for exploiting multiparametric MRI in the differential diagnosis between low- and high-grade gliomas. Inspired by the emerging analytic applications in data-driven oncologic imaging inference, the present study has provided significant evidence regarding the superiority of advanced imaging modalities to provide imaging biomarkers for tumor profile characterization. Specifically, the parameter of lipids/Cr derived from MR spectroscopic imaging was the most important biomarker, essentially describing the difference in the necrotic component between the two grades statuses. Dynamic perfusion and diffusion sequences can provide additional robust biomarkers that complete the non-invasive parameters regarding the tumor extend, structure, and biologic processes which are uniquely associated with the tumor profile. Furthermore, the specific study has showcased the utility of advanced machine learning pipelines for revealing and modelling important associations of the imaging and biologic data and may be used to support the conventional human-based diagnostic evaluation in the clinical practise, featuring high stability and precision in the decision making.

The third study of the present thesis aimed to exploit radiomic analysis for identifying robust imaging biomarkers from breast mpMRI for differentiating benign from malignant lesions. Additional aim was to evaluate the utility of advanced ensemble learning algorithms, towards extending the capabilities of respective previously published ML models. The results have provided important evidence regarding the superiority of DWI compared to T2-weighted MRI for complementing DCE MRI in the characterization of breast malignancy. Evaluation of

Ensemble Learning algorithms have shown increased performance compared to the more conventional ML approaches, such as SVMs.

Overall, both studies have highlighted the substantial improvement in oncologic diagnosis when this incorporates advanced multiparametric imaging techniques that exploit the unique advantages of each single method, along with overcoming their individual limitations. However, various practical considerations arise, either related to the ease and applicability of advanced imaging in the clinical practise, as well as the incorporation of state-of-the-art machine learning evaluation techniques. These considerations are currently in the centre of interest of many research teams and will be discussed below.

Initially, it should be realized that the availability of advanced scanning protocols is relatively low due to the associated high costs for the equipment acquisition and operation. To date it is estimated that over 50000 MRI units are in use across the globe, however the vast majority are 1.5 Tesla units, that do not feature advanced imaging protocols, not to mention that access to MRI scanning in many underdeveloped countries is extremely limited. Of note, even in countries with high units-per-million-population rates of MRI facilities, the time needed for the acquisition and evaluation of advanced multiparametric imaging protocols may constitute more of a problem rather than a solution for health care systems. This is particular evident in cancer screening when considering the small proportion of clinically significant cancers compared to the total number of suspicious cases examined in daily basis. For instance, considering the high rates of incoming patients, and the duration of a complete mpMRI scanning protocol (~50 min) it is evident that radiologic departments are currently pushed to their limits. Thus, there is an unmet need for introducing fast scanning protocols, that despite their lower diagnostic efficiency compared to the complete protocols, they could be utilized to provide a coarse evaluation of the pathology and stratify patients according to the estimated risk of malignancy. In turn the mpMRI protocol could be offered only to those patients with a

strong suspicion for high-risk, to complement characterization procedures, also reducing the associated burden and costs of the health providers.

Following the afore mentioned constraints, today many research departments in academia and beyond focus on the development and evaluation of various solutions, such as low-cost, portable MRI scanners of low magnetic field that can be used to cover the increased demands in decentralized hospitals, or low-income countries, and fast scanning protocols for reducing the duration of MRI examination. Of note, these solutions certainly trade-off the quality and benefits of advanced imaging protocols. To compensate for the loss of clinically important imaging information, a significant stream of research focuses on exploiting machine learning methodologies for addressing these challenges. Some important examples include the development of novel AI-based reconstruction algorithms that generate high-resolution images from sparse sampled (compressed sensing) (202) and parallel image acquisition (203), and the use of ML methods to augment the capabilities of conventional imaging protocols not including advanced techniques (204), and abbreviated or even ultra-fast advanced protocols (205) that are based on the acquisition of only a sample of the images of a complete multiparametric protocol. Nevertheless, these approaches have still to go through intensive validation, however the value of ML algorithms in boosting the capabilities of abbreviated protocols in various clinical questions is already evident.

Despite the new levels of knowledge obtained from the emerging statistical learning frameworks, their application is challenged by numerous factors that are universally present in almost all corresponding medical imaging paradigms. First and foremost, the success of AI models is critically related to the training sample size utilized. In principle, sufficient amount of training data, and data of different origins bringing along the unique intrinsic features of their acquisition procedures, are required to ensure that models will have high reliability and capability of generalizing in new unseen data. However, this is a key challenge when considering advanced MRI techniques, since there are only few decades that these have been

incorporated into the clinical practise, while there are even fewer years that data for research affairs are being collected in a systematic manner. Towards this direction the important contribution of extended multi-institutional research consortia, aiming in large scale data collection, analysis, and standardization of clinically specific radiomic signatures, should be acknowledged (206). Besides big data, these efforts also benefit from the augmented computational power for analysis and pursuing the different scientific aspects into a collaborative manner (e.g., study design, results interpretation, etc).

Lately, the further considerations regarding the incorporation of AI algorithms in medical image applications and the key principles that should be adopted for promoting best practice in this technology application, have let to the development of novel frameworks for protected data sharing between research consortia. In this context, the emerging framework of Federated Learning is currently the state-of-art approach. Federated Learning aims in decentralized ML algorithm training for accurate and robust models, where only the training parameters of the models are shared but not the original image inputs (207). This approach has demonstrated unique efficiency in a recent study for brain tumor segmentation that exploited data from 71 research departments worldwide (208).

In conclusion, the past decade research has provided strong evidence regarding the value of incorporating advanced computational methods to leverage the enriched information provided from the advanced imaging protocols. However, due to the several limitations, including reproducibility/repeatability issues, lacks standards for outcomes validation, low level of technical experience from the clinical personnel, etc, the field has not yet reached the required maturity and credibility needed for the translation and exploitation of the methodologies into the daily clinical practice. Fortunately, overcoming the initial proof-of-concept nature, novel studies currently aim to shrink the gap between research and practice by designing extended clinical trials towards the standardization and acceptance of the AI protocols. Finally, it is evident that we are in front of an epoch-making moment, where the

incorporation of computational intelligence approaches is gradually transforming the clinical practice into a more efficient and preventive healthcare.

this page intentionally left blank

1. Morin O, Vallières M, Jochems A, al. e. A Deep Look Into the Future of Quantitative Imaging in Oncology: A Statement of Working Principles and Proposal for Change. International journal of radiation oncology, biology, physics. 2018; 102(4): 1074–1082.

2. Sander C CY, Hansen HD, Wey HY. Advances in simultaneous PET/MR for imaging neuroreceptor function. J Cereb Blood Flow Metab. 2020; 40: 1148-1166.

3. Khalili-Mahani N, Rombouts SA, van Osch MJ, et a. Biomarkers, designs, and interpretations of resting-state fMRI in translational pharmacological research: A review of state-of-the-Art, challenges, and opportunities for studying brain chemistry. Hum Brain Mapp. 2017; 38: 2276-2325.

4. Bi WL, Hosny A, Schabath M. Artificial intelligence in cancer imaging: Clinical challenges and applications. CA: a cancer journal for clinicians. CA: a cancer journal for clinicians. 2019; 69(2): 127–157.

5. Lawn T, Howard M, Turkheimer F, al e. From Neurotransmitters to Networks: Transcending Organisational Hierarchies with Molecular-informed Functional Imaging. 2022.

6. Tsougos I. Advanced MR Neuroimaging: From Theory to Clinical Practice. 1st ed. Boca Raton, FL, USA: CRC Press; 2018.

7. Rogers W, Thulasi Seetha S, Refaee TAG. Radiomics: from qualitative to quantitative imaging. The British journal of radiology. 2020; 93(1108): 20190948.

8. Tsougos I, Vamvakas A, Kappas C, al. e. Application of Radiomics and Decision Support Systems for Breast MR Differential Diagnosis. Comput Math Methods Med. 2018; 2018: 7417126.

9. Huneau C, BH, Chabriat H. Investigating Human Neurovascular Coupling Using Functional Neuroimaging: A Critical Review of Dynamic Models. Front. Neurosci. 2015; 9: 467.

10. Jafarian A, Litvak V, Cagnan H. Comparing dynamic causal models of neurovascular coupling with fMRI and EEG/MEG. NeuroImage. 2020; 216: 116734.

11. Pattinson KT. Functional magnetic resonance imaging in anaesthesia research. British journal of anaesthesia. 2013; 111(6): 872–876.

12. Sander CY, Hesse S. News and views on in vivo imaging of neurotransmission using PET and MRI. Q J Nucl Med Mol Imaging. 2017; 61: 414-428.

13. Harvey AK,TAM, Wise RG. Imaging pain in arthritis: advances in structural and functional neuroimaging. Curr Pain Headache Rep. 2012; 16: 492-501.

14. Schmidt-Wilcke T. Neuroimaging of chronic pain. Best Pract Res Clin Rheumatol. 2015; 29: 29-41.

15. Loggia ML, Segerdahl AR, Howard MA, et a. Imaging clinically relevant pain states using arterial spin labeling. Pain rep. 2019; 4: e750.

16. Jenkins BG. Pharmacologic Magnetic Resonance Imaging (phMRI): Imaging Drug Action in the Brain. Neuroimage. 2012.

17. Logothetis NK. The neural basis of the blood-oxygen-level-dependent functional magnetic resonance imaging signal. Phil. Trans. R. Soc. Lond. B. 2002.

18. Dipasquale O, Selvaggi P, Veronese M, et a. Receptor-Enriched Analysis of functional connectivity by targets (REACT): A novel, multimodal analytical approach informed by PET to study the pharmacodynamic response of the brain under MDMA. NeuroImage. 2019; 195: 252-260.

19. Dukart J, Holiga S, Chatham C, et a. Cerebral blood flow predicts differential neurotransmitter activity. Sci Rep. 2018; 8: 4074.

20. Sander CY, Hooker JM, Catana C. Neurovascular coupling to D2/D3 dopamine receptor occupancy using simultaneous PET/functional MRI. Proceedings of the National Academy of Sciences of the United States of America. 2013; 110(27): 11169–11174.

21. Selvaggi P, Hawkins PCT, Dipasquale O, et a. Increased cerebral blood flow after single dose of antipsychotics in healthy volunteers depends on dopamine D2 receptor density profiles. Neuroimage. 2019; 188: 774-784.

22. Lawn T, Dipasquale O, Vamvakas A. Differential contributions of serotonergic and dopaminergic functional connectivity to the phenomenology of LSD. Psychopharmacology. 2022.

23. Dipasquale , O. CAD, Martins DF. Molecular-enriched functional connectivity in the human brain using multiband multi-echo simultaneous ASL/BOLD fMRI. bioRxiv. 2022.

24. Dukart J, Holiga S, Rullmann M. JuSpace: A tool for spatial correlation analyses of magnetic resonance imaging data with nuclear imaging derived neurotransmitter maps. Human brain mapping. 2021; 42(3): 555–566.

25. Palomero-Gallagher N, Amunts K, Zilles K. Transmitter Receptor Distribution in the Human Brain. Brain Mapping: An Encyclopedic Reference. 2015; 2: 261–275.

26. Murgaš M, Michenthaler P, Reed MB. Correlation of receptor density and mRNA expression patterns in the human cerebral cortex. NeuroImage. 2022; 256: 119-214.

27. Hawrylycz M, Lein E, Guillozet-Bongaarts A, et a. An anatomically comprehensive atlas of the adult human transcriptome. Nature. 2012; 489: 391-399.

28. Woolf CJ. Overcoming obstacles to developing new analgesics. Nat Med. 2020; 16: 1241-1247.

29. Walsh DA, Stocks J. New Therapeutic Targets for Osteoarthritis Pain. SLAS Discov. 2017; 22: 931-949.

30. Howard MA, Sanders D, Krause K, et a. Alterations in resting-state regional cerebral blood flow demonstrate ongoing pain in osteoarthritis: An arterial spin-labeled magnetic resonance imaging study. Arthritis Rheum. 2012; 64: 3936-3946.

31. Ossipov MH, Dussor GO, and Porreca F. Central modulation of pain. J Clin Invest. 2010; 120: 3779-3787.

32. Steen Pettersen P, Neogi T, Magnusson K, et a. Peripheral and Central Sensitization of Pain in Individuals With Hand Osteoarthritis and Associations With Self-Reported Pain Severity. Arthritis Rheumatol. 2019; 71: 1070-1077.

33. Coghill RC, G MJ, Yen YF. Neural correlates of interindividual differences in the subjective experience of pain. Proc Natl Acad Sci U S A. 2003; 100: 8538-8542.

34. Martucci KT, Mackey SC. Imaging Pain. Anesthesiol Clin. 2016; 34: 255-269.

35. Necka EA, Lee IS, Kucyi A, et a. Applications of dynamic functional connectivity to pain and its modulation. Pain Rep. 2019; 4: e752.

36. Youssef AM, Gustin SM, Nash PG, Reeves JM, Petersen ET, Peck CC, et al. Differential brain activity in subjects with painful trigeminal neuropathy and painful temporomandibular disorder. Pain. 2014; 155(3): 467–475.

37. Wasan AD, Loggia ML, Chen LQ, al. e. Neural correlates of chronic low back pain measured by arterial spin labeling. Anesthesiology. 2011; 115(2): 364–374.

38. DaSilva AF, Zubieta J, DosSantos M. Positron emission tomography imaging of endogenous mu-opioid mechanisms during pain and migraine. PAIN Rep. 2019; 4: e769.

39. Wey HY, Catana C, Hooker JM, et. a. Simultaneous fMRI–PET of the opioidergic pain system in human brain. Neuroimage. 2014; 102: 275-282.

40. Karjalainen T, Karlsson HK, Lahnakoski JM, et a. Dissociable Roles of Cerebral μ-Opioid and Type 2 Dopamine Receptors in Vicarious Pain: A Combined PET–fMRI Study. Cerebral Cortex. 2017; 27: 4257-4266.

41. Howard MA, Krause K, Khawaja N, et a. Beyond patient reported pain: perfusion magnetic resonance imaging demonstrates reproducible cerebral representation of ongoing post-surgical pain. PLoS One. 2011; 6: e17096.

42. Teepker M, M P, H V, et a. Menstrual variation in experimental pain: correlation with gonadal hormones. Neuropsychobiology. 2010; 61: 131-140.

43. O'Muircheartaigh J, Marquand A, Hodkinson DJ. Multivariate decoding of cerebral blood flow measures in a clinical model of on-going postsurgical pain. Human brain mapping. 2015; 36(2): 633–642.

44. Desikan RS, Segonne F, Fischl B, et a. An automated labeling system for subdividing the human cerebral cortex on MRI scans into gyral based regions of interest. Neuroimage. 2006; 31: 968-980.

45. Worsley K. CHAPTER 18 - Random Field Theory. In Friston KJ, Ashburner JT, Kiebel SJ, Nichols TE, William PD. Statistical Parametric Mapping: The Analysis of Functional Brain Images.: Academic Press; 2007. p. 232-236.

46. Tuominen L, Nummenmaa L, Keltikangas-Jarvinen L, et a. Mapping neurotransmitter networks with PET: an example on serotonin and opioid systems. Human Brain Mapp. 2014; 35: 1875-1884.

47. Dunn JT, Stone j, Cleij M, et a. Differential occupancy of striatal versus extrastriatal dopamine D2/D3 receptors by the typical antipsychotic Haloperidol in man measured using [18F]-Fallypride PET. Neuroimage. 2009; 47: S176.

48. Beliveau V, Ganz M, Feng L, et a. A high-resolution in vivo atlas of the human brain's serotonin system. J. Neurosci. 2017; 37: 120-128.

49. Molet J, Pohl M. Gene-based approaches in pain research and exploration of new therapeutic targets and strategies. Eur J Pharmacol. 2013; 716: 129-141.

50. Rizzo G, Veronese M, Expert P, et a. MENGA: a new comprehensive tool for the integration of neuroimaging data and the allen human brain transcriptome atlas. PLoS One. 2016; 11: e0148744.

51. Hair J, Black W, Babin B, et a. Advanced diagnostics for multiple regression: A supplement to multivariate data analysis P P, editor.: Hall Publishing; 2010.

52. May A. Chronic pain may change the structure of the brain. Pain. 2008; 137(1): 7–15.

53. Kupers R, Kehlet H. Brain imaging of clinical pain states: a critical review and strategies for future studies. The Lancet. Neurology. 2006; 5(12): 1033–1044.

54. Markello RD, Misic B. Comparing spatial null models for brain maps. Neuroimage. 2021; 236: 118052.

55. Zubieta JK, Smith YR, Bueller JA, et a. Regional mu opioid receptor regulation of sensory and affective dimensions of pain. Science. 2001; 293: 311-315.

56. Skyt I, Lunde SJ, Baastrup C, et a. Neurotransmitter systems involved in placebo and nocebo effects in healthy participants and patients with chronic pain: a systematic review. Pain. 2020; 161: 11-23.

57. Lueptow LM, Fakira A, Bobeck E. The Contribution of the Descending Pain Modulatory Pathway in Opioid Tolerance. Front Neurosci. 2018; 12: 886.

58. Shih YYI, Chiang YC, Shyu BC, et a. Endogenous opioid–dopamine neurotransmission underlie negative CBV fMRI signals. Experimental Neurology. 2012; 234: 382-388.

59. Gwilym S, Keltner J, Warnaby C, et a. Psychophysical and functional imaging evidence supporting the presence of central sensitization in a cohort of osteoarthritis patients. Arthritis Rheum. 2009; 61: 1226-1234.

60. Crawford LS, Mills EP, Hanson T. Brainstem Mechanisms of Pain Modulation: A within-Subjects 7T fMRI Study of Placebo Analgesic and Nocebo Hyperalgesic Responses. The Journal of neuroscience : the official journal of the Society for Neuroscience. 2021; 41(47): 9794–9806.

61. Harte SE, Harris RE, Clauw DJ. The neurobiology of central sensitization. Journal of Applied Biobehavioral Research. 2018; 23: e12137.

62. Bannister K, Dickenson A. What do monoamines do in pain modulation. Curr Opin Support Palliat Care. 2016; 10: 143-148.

63. Bravo L, Llorca-Torralba M, Berrocoso E, et a. Monoamines as Drug Targets in Chronic Pain: Focusing on Neuropathic Pain. Front. Neurosci. 2019; 13: 1268.

64. Kloppenburg M, Kroon F, Blanco F, et a. 2018 update of the EULAR recommendations for the management of hand osteoarthritis. Annals of the Rheumatic Diseases. 2019; 78: 16-24.

65. Scott DJ, Heitzeg M, Koeppe R, et a. Variations in the human pain stress experience mediated by ventral and dorsal basal ganglia dopamine activity. J Neurosci. 2006; 26: 10789-10795.

66. Ledermann K, Jenewein J, Sprott H, et a. Relation of dopamine receptor 2 binding to pain perception in female fibromyalgia patients with and with out depression – A [11C] raclopride PET-study. Eur Neuropsychopharmacol. 2016; 26: 320-330.

67. Bannister K, Bee L, Dickenson A. Preclinical and early clinical investigations related to monoaminergic pain modulation. Neurotherapeutics. 2009; 6: 703-712.

68. Viguier F, Michot B, Hamon M, et a. Multiple roles of serotonin in pain control mechanisms--implications of 5-HT_7 and other 5-HT receptor types. Eur J Pharmacol. 2013; 716: 8-16.

69. Martikainen IK, Hagelberg N, Jääskeläinen S, et a. Dopaminergic and serotonergic mechanisms in the modulation of pain: In vivo studies in human brain. Eur J Pharmacol. 2018; 834: 337-345.

70. Kupers R, Frokjaer V, Naert A, et a. A PET [18F]altanserin study of 5-HT2A receptor binding in the human brain and responses to painful heat stimulation. NeuroImage. 2009; 44: 1001-1007.

71. Martikainen IK, Hirvonen J, Kajander J, et a. Correlation of human cold pressor pain responses with 5-HT1A receptor binding in the brain. Brain Res. 2007; 1172: 21-31.

72. Martikainen IK, Hirvonen J, Pesonen U, et a. Differential associations between brain 5-HT1A receptor binding and response to pain versus touch. J Neural Transm (Vienna). 2009; 116: 821-830.

73. Tao ZY, Wang P, Wei S, et a. The Role of Descending Pain Modulation in Chronic Primary Pain: Potential Application of Drugs Targeting Serotonergic System. Neural Plast. 2019; 2019: 1389296.

74. Valentino RJ, Volkow N. Untangling the complexity of opioid receptor function. Neuropsychopharmacology. 2018; 43: 2514-2520.

75. Wang YJ, Zuo Z, Wu C, et a. Cingulate Alpha-2A Adrenoceptors Mediate the Effects of Clonidine on Spontaneous Pain Induced by Peripheral Nerve Injury. Front Mol Neurosci. 2017; 10: 289.

76. Wu CL, Raja S. Treatment of acute postoperative pain. Lancet. 2011; 377: 2215-2225.

77. Denk F, McMahon S. Neurobiological basis for pain vulnerability: why me? Pain. 2017; 158: S108-S114.

78. O'Connor JP, Rose CJ, Waterton JC, al. e. Imaging intratumor heterogeneity: role in therapy response, resistance, and clinical outcome. Clinical cancer research : an official journal of the American Association for Cancer Research. 2015; 21(2): 249–257.

79. Napel S, Mu W, Jardim-Perassi B, al. e. Quantitative imaging of cancer in the postgenomic era: Radio(geno)mics, deep learning, and habitats. Cancer. 2018.

80. Alizadeh AA, Aranda V, Bardelli A, al. e. Toward understanding and exploiting tumor heterogeneity. Nature medicine. 2015; 21(8): 846–853.

81. Yip SS, Aerts HJ. Applications and limitations of radiomics. Physics in medicine and biology. 2016; 61(13): R150–R166.

82. Clarke GM, Peressotti C, Constantinou P, al. e. Increasing specimen coverage using digital whole-mount breast pathology: implementation, clinical feasibility and application in research. Computerized medical imaging and graphics : the official journal of the Computerized Medical Imaging Society. 2011; 35(7-8): 531–541.

83. Neri E, Del Re M, Paiar F, al. e. Radiomics and liquid biopsy in oncology: the holons of systems medicine. Insights into imaging. 2018; 9(6): 915–924.

84. Abrol S, Kotrotsou A, Salem A, al. e. Radiomic Phenotyping in Brain Cancer to Unravel Hidden Information in Medical Images. Topics in magnetic resonance imaging : TMRI. 2017; 26(1): 43–53.

85. García-Figueiras R, Baleato-González S, Padhani AR. How clinical imaging can assess cancer biology. Insights into imaging. 2019; 10(1): 28.

86. Varghese B, Chen F, Hwang D, al. e. Objective risk stratification of prostate cancer using machine learning and radiomics applied to multiparametric magnetic resonance images. Sci Rep. 2019; 9: 1570.

87. Nahid AA, Kong Y. Involvement of Machine Learning for Breast Cancer Image Classification: A Survey. Computational and Mathematical Methods in Medicine. 2017; 2017: 3781951.

88. Verma V, Simone CB, Krishnan S. The Rise of Radiomics and Implications for Oncologic Management. Journal of the National Cancer Institute. 2017; 109(7).

89. Avanzo M, Stancanello J, El Naqa I. Beyond imaging: the promise of radiomics. Phys. Med. 2017; 38: 122-39.

90. Avanzo M, Wei L, Stancanello J, al. e. Machine and deep learning methods for radiomics. Medical physics. 2020; 47(5): e185–e202.

91. Larue R, Defraene G, De Ruysscher D, al. e. Quantitative radiomics studies for tissue characterization: a review of technology and methodological procedures. Br. J. Radiol. 2017; 90(1070): 20160665.

92. Limkin E, Sun R, Dercle L, al. e. Promises and challenges for the implementation of computational medical imaging (radiomics) in oncology. Ann. Oncol. 2017; 28(6): 1191e206.

93. Weaver O, Leung JWT. Biomarkers and imaging of breast cancer. American Journal of Roentgenology. 2018; 210(2): 271–278.

94. Haralick R. Statistical and structural approaches to texture. Proceedings of the IEEE. 1979; 67(5): 786–804.

95. Sutton EJ, Huang EP, Drukker K. Breast MRI radiomics: comparison of computer- and human-extracted imaging phenotypes. European Radiology Experimental. 2017; 1(1): 22.

96. Galloway MM. Texture analysis using gray level run lenghts. Computer Graphics and Image Processing. 1975; 4(2): 172-179.

97. Shen D, Wu G, Suk HI. Deep learning in medical image analysis. Annual Review of Biomedical Engineering. 2017; 19(1): 221-248.

98. Forghani R, Savadjiev P, Chatterjee A. Radiomics and Artificial Intelligence for Biomarker and Prediction Model Development in Oncology. Comput Struct Biotechnol J. 2019; 17: 995–1008.

99. Gillies R, Kinahan P, Hricak H. Radiomics: images are more than pictures, they are data. Radiology. 2016 February; 278(2): 563-77.

100. van Griethuysen J, Fedorov A, Parmar C, al. e. Computational Radiomics System to Decode the Radiographic Phenotype. Cancer Res. 2017; 77(21): e104-e107.

101. Louis D, Ohgaki H, Wiestler O, al e. The 2007 WHO classification of tumours of the central nervous system. Acta Neuropathologica. 2007; 114: 97-109.

102. Skogen K, Schulz A, Dormagen J. Diagnostic performance of texture analysis on MRI in grading cerebral gliomas. Eur J Radiol. 2016; 85(4): 824-9.

103. Hsieh KLC, Chena CY, Lod CM. Quantitative glioma grading using transformed gray-scale invariant textures of MRI. Comput Biol Med. 2017; 83: 102-108.

104. Hsieh KLC, Lo CM, Hsiao CJ. Computer-aided grading of gliomas based on local and global MRI features. Computer methods and programs in biomedicine. 2017; 139: 31-8.

105. Ryu Y, Choi S, Park S, al e. Glioma: application of whole-tumor texture analysis of diffusion-weighted imaging for the evaluation of tumor heterogeneity. PLoS One. 2014; 9(9): e108335.

106. Lee J, Choi S, Kim J, al e. Glioma grading using apparent diffusion coefficient map: application of histogram analysis based on automatic segmentation. NMR Biomed. 2014; 27(9): 1046-52.

107. Katsaros V, Nikiforaki K, Manikis G, al. e. Whole tumor MR Perfusion histogram analysis in the preoperative assessment of patients with gliomas: Differentiation between high-and low-grade tumors. Hellenic Journal of Radiology. 2017; 2(1).

108. Wang Q, Zhang H, Zhang J, al. e. The diagnostic performance of magnetic resonance spectroscopy in differentiating high-from low-grade gliomas: A systematic review and meta-analysis. Eur Radiol. 2016; 26(8): 2670-84.

109. Mohan G, Subashini MM. MRI based medical image analysis: Survey on brain tumor grade classification. Biomedical Signal Processing and Control. 2018; 39: 139-61.

110. Roy B, Gupta RK, Maudsley AA, et. a. Utility of Multiparametric 3T MRI for Glioma Characterization. Neuroradiology. 2013; 55(5): 603–13.

111. Van Cauter S, De Keyzer F, Sima D, et. a. Integrating diffusion kurtosis imaging, dynamic susceptibility-weighted contrast-enhanced MRI, and short echo time chemical shift imaging for grading gliomas. Neuro Oncol. 2014; 16(7): 1010-21.

112. Zacharaki E, Wang S, Chawla S, et. a. Classification of brain tumor type and grade using MRI texture and shape in a machine learning scheme. Magn Reson Med. 2009; 62(6): 1609-18.

113. Svolos P, Tsolaki E, Kapsalaki E, et. a. Investigating brain tumor differentiation with diffusion and perfusion metrics at 3T MRI using pattern recognition techniques. Magnetic resonance imaging. 2013; 31(9): 1567-77.

114. Qin Jb, Liu Z, Zhang H, et. a. Grading of Gliomas by Using Radiomic Features on Multiple Magnetic Resonance Imaging (MRI) Sequences. Med Sci Monit. 2017; 23: 2168–78.

115. Cho HH., Lee SH, Kim J, al. e. Classification of the glioma grading using radiomics analysis. PeerJ. 2018;: e5982.

116. Zinn P, Mahmood Z, Elbanan M, et. a. Imaging Genomics in Gliomas. Cancer J. 2015; 21(3): 225-34.

117. Kickingereder P, Andronesi O. Radiomics, Metabolic, and Molecular MRI for Brain Tumors. Semin Neurol. 2018; 38(1): 32-40.

118. Bisdas S, Shen H, Thust S, et. a. Texture analysis-and support vector machine-assisted diffusional kurtosis imaging may allow in vivo gliomas grading and IDH-mutation status prediction: a preliminary study. Scientific reports. 2018; 8(1): 6108.

119. De Looze C, Beausang A, Cryan J, al e. Machine learning: a useful radiological adjunct in determination of a newly diagnosed glioma's grade and IDH status. J Neurooncol. 2018.

120. Louis D, Perry A, Reifenberger G, et. a. The 2016 World Health Organization Classification of Tumors of the Central Nervous System: a summary. Acta Neuropathol. 2016; 131(6): 803-20.

121. Parekh V, Jacobs M. Radiomics: a new application from established techniques. Expert Rev Precis Med Drug Dev. 2016; 1(2): 207-26.

122. Citak-Er F, Firatc Z, Kovanlikayad I, et. a. Machine-learning in grading of gliomas based on multi-parametric magnetic resonance imaging at 3T. Comput Biol Med. 2018; 99: 154-60.

123. Tian Q, Yan L, Zhang X, al. e. Radiomics strategy for glioma grading using texture features from multiparametric MRI. J Magn Reson Imaging. 2018; 48(6): 1518-28.

124. Wilson M, Reynolds G, Kauppinen R, al. e. A constrained least-squares approach to the automated quantitation of in vivo ^{1}H magnetic resonance spectroscopy data. Magn Reson Med. 2011; 65(1): 1-12.

125. Boxerman J, Prah D, Paulson E, et. a. The Role of preload and leakage correction in gadolinium-based cerebral blood volume estimation determined by comparison with MION as a criterion standard. AJNR Am J Neuroradiol. 2012; 33(6): 1081-7.

126. Bjornerud A, Sorensen AG, Mouridsen K, et. a. T1- and T*2-Dominant Extravasation Correction in DSC-MRI: Part I—Theoretical Considerations and Implications for Assessment of Tumor Hemodynamic Properties. Journal of Cerebral Blood Flow & Metabolism. 2011; 31(10): 2041-2053.

127. Welker K, Boxerman J, Kalnin A, et. a. ASFNR Recommendations for Clinical Performance of MR Dynamic Susceptibility Contrast Perfusion Imaging of the Brain. American Journal of Neuroradiology. 2015; 36(6).

128. Jenkinson M, Beckmann CF, Behrens TE, et. a. FSL. NeuroImage. 2012; 62: 782-90.

129. Jenkinson M, Smith SM. A global optimisation method for robust affine registration of brain images. Medical Image Analysis. 2001; 5(2): 143-156.

130. Jenkinson M, Bannister PR, Brady JM, et. a. Improved optimisation for the robust and accurate linear registration and motion correction of brain images. NeuroImage. 2002; 17(2): 825-841.

131. Andersson LRJ, Sotiropoulos SN. An integrated approach to correction for off-resonance effects and subject movement in diffusion MR imaging. NeuroImage. 2016; 125: 1063-1078.

132. Smith SM, Jenkinson M, Woolrich MW, et. a. Advances in functional and structural MR image analysis and implementation as FSL. NeuroImage. 2004; 23(S1): 208-19.

133. Vamvakas A, Tsougos I, Arikidis N, al. e. Exploiting morphology and texture of 3D tumor models in DTI for differentiating glioblastoma multiforme from solitary metastasis. Biomedical Signal Processing and Control. 2018; 43: 159-73.

134. Scarabino T, Popolizio T, Trojsi F, a,e. Role of advanced MR imaging modalities in diagnosing cerebral gliomas. Radiol Med. 2009; 114(3): 448-460.

135. Server A, Josefsen R, Kulle B, al. e. Proton magnetic resonance spectroscopy in the distinction of high-grade cerebral gliomas from single metastatic brain tumors. Acta Radiol. 2010; 51(3): 316-325.

136. Weber M, Zoubaa S, Schlieter M, al. e. Diagnostic performance of spectroscopic and perfusion MRI for distinction of brain tumors. Neurology. 2006; 66 (12): 1899-1906.

137. Chawla S, Zhang Y, Wang S, al. e. Proton magnetic resonance spectroscopy in differentiating glioblastomas from primary cerebral lymphomas and brain metastasis. J Comput Assist Tomogr. 2010; 34(6): 836-41.

138. Materka A, Strzelecki M. Texture Analysis Methods – A Review, Technical University of Lodz. Brussels:; 1998.

139. Strzelecki M, Szczypinski P, Materka A, et. a. A software tool for automatic classification and segmentation of 2D/3D medical images. Nuclear Instruments & Methods In Physics Research. 2013; A, 702: 137-140.

140. Szczypinski P, Strzelecki M, Materka A, et. a. MaZda-A software package for image texture analysis. Computer Methods and Programs in Biomedicine. 2009; 94(1): 66-76.

141. Zhang X, Yan L, Hu Y, al. e. Optimizing a machine learning based glioma grading system using multi-parametric MRI histogram and texture features. Oncotarget. 2017; 8(29): 47816-30.

142. Frank E, Hall MA, Witten IH. The WEKA Workbench. Online Appendix for "Data Mining: Practical Machine Learning Tools and Techniques". 4th ed.: Morgan Kaufmann; 2016.

143. Guyon I, Weston J, Barnhill S, et. a. Gene Selection for Cancer Classification using Support Vector Machines. Machine Learning. 2002; 46: 389.

144. Platt JC, Nitschke RV. Sequential minimal optimization: A fast Algorithm for Training Support Vector machines. Microsoft Research Technical Report. 1998.

145. Court LE, Fave X, Mackin D, al. e. Computational resources for radiomics. Transl Cancer Res. 2016; 5(4): 340–8.

146. Chen W, Liu B, Peng S, al. e. Computer-Aided Grading of Gliomas Combining Automatic Segmentation and Radiomics. International Journal of Biomedical Imaging. 2018; Volume 2018.

147. Server A, Kulle B, Gadmar Ø, al. e. Measurements of diagnostic examination performance using quantitative apparent diffusion coefficient and proton MR spectroscopic imaging in the preoperative evaluation of tumor grade in cerebral gliomas. Eur J Radiol. 2011; 80(2): 462-70.

148. Wang S, Meng M, Zhang X, al. e. Texture analysis of diffusion weighted imaging for the evaluation of glioma heterogeneity based on different regions of interest. Oncol Lett. 2018; 15(5): 7297-304.

149. Brynolfsson P, Nilsson D, Henriksson R, al. e. ADC texture--an imaging biomarker for high-grade glioma? Med Phys. 2014; 41(10): 101903.

150. Raja R, Sinha N, Saini J, al. e. Assessment of tissue heterogeneity using diffusion tensor and diffusion kurtosis imaging for grading gliomas. Neuroradiology. 2016; 58(12): 1217-31.

151. Kousi E, Tsougos I, Tsolaki E, al. e. Spectroscopic evaluation of glioma grading at 3T: the combined role of short and long TE. Scientific World Journal. 2012; 2012: 546171.

152. Tsougos I, Svolos P, Kousi E, al. e. Differentiation of glioblastoma multiforme from metastatic brain tumor using proton magnetic resonance spectroscopy, diffusion and perfusion metrics at 3 T. Cancer Imaging. 2012; 12(3).

153. Su CQ, Lu SS, Han QY, al. e. Intergrating conventional MRI, texture analysis of dynamic contrast-enhanced MRI, and susceptibility weighted imaging for glioma grading. Acta radiologica. 2019; 60(6): 777-787.

154. Sung H, Ferlay J, Siegel R, al. e. Global Cancer Statistics 2020: GLOBOCAN Estimates of Incidence and Mortality Worldwide for 36 Cancers in 185 Countries. CA Cancer J Clin. 2021; 71(3): 209-249.

155. Sheth D, Giger M. Artificial intelligence in the interpretation of breast cancer on MRI. J Magn Reson Imaging. 2020; 51(5): 1310-1324.

156. Zhang M, Horvat J, Bernard-Davila B, al. e. Multiparametric MRI model with dynamic contrast-enhanced and diffusion-weighted imaging enables breast cancer diagnosis with high accuracy. J Magn Reson Imaging. 2019; 49(3): 864-874.

157. Marino M, Helbich T, Baltzer P, al. e. Multiparametric MRI of the breast: A review. J Magn Reson Imaging. 2018; 47(2): 301-315.

158. Pötschm N, Dietzel M, Kapetas P, al. e. An A.I. classifier derived from 4D radiomics of dynamic contrast-enhanced breast MRI data: potential to avoid unnecessary breast biopsies. Eur Radiol. 2021; 31(8): 5866-5876.

159. Chitalia R, Rowland J, McDonald E, al. e. Imaging Phenotypes of Breast Cancer Heterogeneity in Preoperative Breast Dynamic Contrast Enhanced Magnetic Resonance Imaging (DCE-MRI) Scans Predict 10-Year Recurrence. Clin Cancer Res. 2020; 26(4): 862-869.

160. Forghani R, Savadjiev P, Chatterjee A, al. e. Radiomics and Artificial Intelligence for Biomarker and Prediction Model Development in Oncology. Comput Struct Biotechnol J. 2019; 17: 995-1008.

161. Castiglioni I, Gallivanone F, Soda P, al. e. AI-based applications in hybrid imaging: how to build smart and truly multi-parametric decision models for radiomics. Eur J Nucl Med Mol Imaging. 2019; 46(13): 2673-2699.

162. Daimiel Naranjo I, Gibbs P, Reiner J, al. e. Radiomics and Machine Learning with Multiparametric Breast MRI for Improved Diagnostic Accuracy in Breast Cancer Diagnosis. Diagnostics. 2021; 11(6): 919.

163. Parekh V, Jacobs M. Multiparametric radiomics methods for breast cancer tissue characterization using radiological imaging. Breast Cancer Res Treat. 2020; 180(2): 407-421.

164. Hu Q, Whitney H, Giger M. Radiomics methodology for breast cancer diagnosis using multiparametric magnetic resonance imaging. J Med Imaging (Bellingham). 2020; 7(4): 044502.

165. Zhang Q, Peng Y, Liu W, al. e. Radiomics Based on Multimodal MRI for the Differential Diagnosis of Benign and Malignant Breast Lesions. J Magn Reson Imaging. 2020; 52(2): 596-607.

166. Cai H, Peng Y, Ou C, al. e. Diagnosis of breast masses from dynamic contrast-enhanced and diffusion-weighted MR: a machine learning approach. PLoS One. 2014; 9(1): e87387.

167. Jiang X, Xie F, Liu L, al. e. Discrimination of malignant and benign breast masses using automatic segmentation and features extracted from dynamic contrast-enhanced and diffusion-weighted MRI. Oncol Lett. 2018; 16(2): 1521-1528.

168. Brunese L, Mercaldo F, Reginelli A, al. e. An ensemble learning approach for brain cancer detection exploiting radiomic features. Comput Methods Programs Biomed. 2020; 105: 105134.

169. Chen W, Liu B, Peng S, al. e. Computer-Aided Grading of Gliomas Combining Automatic Segmentation and Radiomics. Int J Biomed Imaging. 2018; 2018: 2512037.

170. Li W, Yu K, Feng C, al. e. Molecular Subtypes Recognition of Breast Cancer in Dynamic Contrast-Enhanced Breast Magnetic Resonance Imaging Phenotypes from Radiomics Data. Comput Math Methods Med. 2019; 2019: 6978650.

171. Meng W, Sun Y, Qian H, al. e. Computer-Aided Diagnosis Evaluation of the Correlation Between Magnetic Resonance Imaging With Molecular Subtypes in Breast Cancer. Front Oncol. 2021; 11: 693339.

172. Liu J, Sun D, Chen L, al. e. Radiomics Analysis of Dynamic Contrast-Enhanced Magnetic Resonance Imaging for the Prediction of Sentinel Lymph Node Metastasis in Breast Cancer. Front Oncol. 2019; 9: 980.

173. Tahmassebi A, Wengert G, Helbich T, al. e. Impact of Machine Learning With Multiparametric Magnetic Resonance Imaging of the Breast for Early Prediction of Response to Neoadjuvant Chemotherapy and Survival Outcomes in Breast Cancer Patients. Invest Radiol. 2019; 54(2): 110-117.

174. Lu W, Li Z, Chu J. A novel computer-aided diagnosis system for breast MRI based on feature selection and ensemble learning. Comput Biol Med. 2017; 83: 157-165.

175. Freund Y, Schapire R. A Decision-Theoretic Generalization of On-Line Learning and an Application to Boosting. COLT. 1997; 1997.

176. Mason L, Baxter J, Bartlett P, al. e. Boosting algorithms as gradient descent in function space. Proc. NIPS. 1999; 12: 512-518.

177. Chen T, He T, Benesty M, al. e. Xgboost: extreme gradient boosting. R package version. 2015; 0.4-2: 1-4.

178. Ke G, Meng Q, Finley T, al. e. Lightgbm: A highly efficient gradient boosting decision tree. Advances in neural information processing systems. 2017; 30: 3146-3154.

179. von Elm E, Altman D, Egger M, al. e. The Strengthening the Reporting of Observational Studies in Epidemiology (STROBE) statement: guidelines for reporting observational studies. Ann Intern Med. 2007; 147: 573-577.

180. Zwanenburg A, Vallières M, Abdalah M, al. e. The Image Biomarker Standardization Initiative: Standardized Quantitative Radiomics for High-Throughput Image-based Phenotyping. Radiology. 2020; 295(2): 328-338.

181. Hunter JD. Matplotlib: A 2D Graphics Environment. Computing in Science & Engineering. 2007; 9(3): 90-95.

182. Kursa M, Rudnicki W. Feature Selection with the Boruta Package. Journal of Statistical Software. 2010; 36: 1-13.

183. Laukamp K, Shakirin G, Baeßler B, al. e. Accuracy of Radiomics-Based Feature Analysis on Multiparametric Magnetic Resonance Images for Noninvasive Meningioma Grading. World Neurosurg. 2019; 132: e366-e390.

184. Kimura K, Yoshida S, Tsuchiya J, al. e. Usefulness of texture features of apparent diffusion coefficient maps in predicting chemoradiotherapy response in muscle-invasive bladder cancer. European radiology. 2022; 32(1): 671–679.

185. Pedregosa F, Varoquaux G, Gramfort A, al. e. Scikit-learn: Machine learning in Python. The Journal of machine Learning research. 2011; 12(85): 2825-2830.

186. Bradley E, Tibshirani R. Improvements on Cross-Validation: The.632+ Bootstrap Method. Journal of the American Statistical Association 92. 1997; 438: 548.

187. DeLong E, DeLong D, Clarke-Pearson D, al. e. Comparing the areas under two or more correlated receiver operating characteristic curves: a nonparametric approach. Biometrics. 1988; 44(3): 837-845.

188. Morris E, Comstock C, Lee C, al. e. ACR BI-RADS® Magnetic Resonance Imaging. In: ACR BI-RADS® Atlas, Breast Imaging Reporting and Data System Reston, VA: American College of Radiology; 2013.

189. Clauser P, Krug B, Bickel H, al. e. Diffusion-weighted Imaging Allows for Downgrading MR BI-RADS 4 Lesions in Contrast-enhanced MRI of the Breast to Avoid Unnecessary Biopsy. Clin Cancer Res. 2021; 27(7): 1941-1948.

190. Zhu CR, Chen KY, Li P, al. e. Accuracy of multiparametric MRI in distinguishing the breast malignant lesions from benign lesions: a meta-analysis. Acta radiologica. 2021; 62(10): 1290–1297.

191. Tagliafico A, Piana M, Schenone D, al. e. Overview of radiomics in breast cancer diagnosis and prognostication. Breast. 2020; 49: 74-80.

192. Lo Gullo R, Eskreis-Winkler S, Morris E, al. e. Machine learning with multiparametric magnetic resonance imaging of the breast for early prediction of response to neoadjuvant chemotherapy. Breast. 2020; 49: 115-122.

193. Meyer-Base A, Morra L, Tahmassebi A, al. e. AI-Enhanced Diagnosis of Challenging Lesions in Breast MRI: A Methodology and Application Primer. J Magn Reson Imaging. 2021; 54(3): 686-702.

194. Dalmiş M, Gubern-Mérida A, Vreemann S, al. e. Artificial Intelligence-Based Classification of Breast Lesions Imaged With a Multiparametric Breast MRI Protocol With Ultrafast DCE-MRI, T2, and DWI. Invest Radiol. 2019; 54(6): 325-332.

195. Li Z, Zhai G, Zhang J, al. e. Differentiation of clear cell and non-clear cell renal cell carcinomas by all-relevant radiomics features from multiphase CT: a VHL mutation perspective. Eur Radiol. 2019; 29(8): 3996-4007.

196. Sakai Y, Yang C, Kihira S, al. e. MRI Radiomic Features to Predict IDH1 Mutation Status in Gliomas: A Machine Learning Approach using Gradient Tree Boosting. Int J Mol Sci. 2020; 21(21): 8004.

197. Koyasu S, Nishio M, Isoda H, al. e. Usefulness of gradient tree boosting for predicting histological subtype and EGFR mutation status of non-small cell lung cancer on 18F FDG-PET/CT. Ann Nucl Med. 2020; 34(1): 49-57.

198. Fangoh M, Selim S. Using CNN-XGBoost Deep Networks for COVID-19 Detection in Chest X-ray Images. 15th International Conference on Computer Engineering and Systems (ICCES). 2020;: 1-7.

199. Chitalia R, Kontos D. Role of texture analysis in breast MRI as a cancer biomarker: A review. J Magn Reson Imaging. 2019; 49(4): 927-938.

200. Jiang Y, Cao S, Cao S, al. e. Preoperative identification of microvascular invasion in hepatocellular carcinoma by XGBoost and deep learning. J Cancer Res Clin Oncol. 2021; 147(3): 821-833.

201. Vamvakas A, Vassiou K, Tsivaka D, al. e. Decision support systems in breast cancer. In Faintuch , editor. Precision Medicine for Investigators, Practitioners and Providers.: Academic Press; 2020. p. 319-327.

202. Hyun CM, Kim HP, Lee SM, al. e. Deep learning for undersampled MRI reconstruction. Physics in Medicine & Biology. 2017; 63.

203. Knoll F, Hammernik K, Zhang C, al e. Deep-learning methods for parallel magnetic resonance imaging reconstruction: A survey of the current approaches, trends, and issues. IEEE signal processing magazine. 2020; 37(1): 128-140.

204. Bakas S, Shukla G, Akbari H, et. a. Integrative radiomic analysis for pre-surgical prognostic stratification of glioblastoma patients: from advanced to basic MRI protocols. Medical Imaging 2020: Image-Guided Procedures, Robotic Interventions, and Modeling. 2020; 11315 SPIE: 456-461.

205. Drukker K, Anderson R, Edwards A, al e. Radiomics for ultrafast dynamic contrast-enhanced breast MRI in the diagnosis of breast cancer: a pilot study. Medical Imaging 2018: Computer-Aided Diagnosis. 2018; 10575 SPIE : 869-874.

206. Davatzikos C, Barnholtz-Sloan JS, Bakas S, al. e. AI-based prognostic imaging biomarkers for precision neuro-oncology: the ReSPOND consortium. Neuro-oncology. 2020; 22(6): 886-888.

207. Rieke N, Hancox J, Li W, al. e. The future of digital health with federated learning. NPJ digital medicine. 2020; 3(1): 1-7.

208. Pati S, Baid U, Edwards B, al. e. Federated learning enables big data for rare cancer boundary detection. Nature communications. 2022; 13(1): 1-17.

this page intentionally left blank

ABA	Allen Brain Atlas
Acc	Accuracy
ACR	American College of Radiology
AdaBoost	Adaptive Boosting Classifier
ADC	Apparent Diffusion Coefficient
AI	Artificial Intelligence
API	Application Programming Interface
ASL	Arterial Spin Labelling
AUC	Area Under Curve
BBB	Blood Brain Barrier
BI-RADS	Breast Imaging Reporting and Data System
BOLD	Blood Oxygen Level Dependent
BPnd	Binding Potential
CAD	Computer Assisted Diagnosis
Cho	Choline
CI	Confidence Interval
CLBP	Chronic Low Back Pain
CMC	Carpometacarpal
CNN	Convolutional Neural Networks
CNS	Central Nervous System
Cr	Creatine
CSI	Chemical Shift Imaging
CT	Computed Tomography
DCE	Dynamic Contrast Enhanced
DCIS	Ductal Carcinoma In-Situ
DICOM	Digital Imaging and Communications in Medicine
DL	Deep Learning

DK	Desikan-Killiany Atlas
DKI	Diffusion Kurtosis Imaging
DNA	Deoxyribonucleic Acid
DOR	Delta - Opioid Receptor
DSCE	Dynamic Susceptibility Contrast Enhanced
DPSM	Descending Pain Modulatory System
DT	Decision Tree
DTI	Diffusion Tensor Imaging
DWI	Diffusion Weighted Imaging
FA	Fractional Anisotropy
FLAIR	Fluid Attenuation Inversion Recovery
fMRI	Functional Magnetic Resonance Imaging
FSE	Fast Spin-Echo
FOV	Field of View
FEW	Familywise Error
GB	Gradient Boosting
GE	General Electirc
GLCM	Gray Level Cooccurrence Matrix
GLDM	Gray Level Dependence Matrix
GLRLM	Gray Level Run Length Matrix
GLSZM	Gray Level Size Zone Matrix
HC	Hierarchical Clustering
HGG	High Grade Glioma
Hz	Hertz
IBSI	Imaging Biomarkers Standardization Initiative
IDH	Isocitrate Dehydrogenase
IDC	Invasive Ductal Carcinoma
ILC	Invasive Lobular Carcinoma

KOR	Kappa - Opioid Receptor
LCIS	Lobular Carcinoma In-Situ
LGG	Low Grade Glioma
LightGBM	Light Gradient Boosting Machine
LOOCV	Leave-One-Out Cross-Validation
LSD	Lysergic Acid Diethylamide
MD	Mean Diffusivity
MENGA	Multimodal Environment for Neuroimaging and Genomic Analysis Software
ML	Machine Learning
MGMT	6-Methylguanine-Deoxyribonucleic Acid Methyltransferase
MNI	Montreal Neurological Institute
MOR	Mu - Opioid Receptor
mp-MRI	Multiparametric Magnetic resonance imaging
MRMR	Minimum Redundancy Maximum Relevance
mRNA	Messenger Ribonucleic Acid
ms	milliseconds
NAA	N-Acetyl Aspartate
NGTDM	Neighboring Gray Tone Difference Matrix
NIFTI	Neuroimaging Informatics Technology Initiative
NNT	Number Needed to Treat
NRS	Numerical Rating Scale
NSAID	Nonsteroidal Anti-Inflammatory Drug
OA	Osteoarthritis
p	Pure Isotropy
PAG	Periaqueductal Gray
pCASL	Pseudo Continuous Arterial Spin Labelling
PET	Positron Emission Tomography
phMRI	Pharmacological Magnetic Resonance Imaging

PI-RADS	Prostate Imaging Reporting and Data System
PROBE	PROton Brain Exam Software
q	Pure Anisotropy
rCBF	Relative Cerebral Blood Flow
rCBV	Relative Cerebral Blood Volume
REACT	Receptor-Enriched Analysis of Functional Connectivity by Targets
RF	Random Forest
RFE	Recursive Feature Elimination
ROC	Receiver Operator Characteristic
ROI	Region of Interest
SD	Standard Deviation
Se	Sensitivity
SMO	Sequential Minimal Optimization
SNR	Signal to Noise Ratio
Sp	Specificity
STIR	Short Tau Inversion Recovery
SV	Single Voxel
SVM	Support Vector Machine
TE	Echo Time
TME	Third Molar Extraction
TR	Repetition Time
T2-w	T2 Weighted Imaging
VAS	Visual Analogue Scale
VDP	Variance Decomposition Proportion
VIF	Variance Inflation Factor
VOI	Volume of Interest
WHO	World Health Organization
XGBoost	Extreme Gradient Boosting

1H-MRS	1Hydrogen - Magnetic Resonance Spectroscopy
2D	2-Dimensional
3D	3-Dimensional
3D-SPGR	3-Dimensional Spoiled Gradient Echo
3T	3 Tesla
5-HT	5-Hydroxytryptamine

this page intentionally left blank

List of Figures

List of Tables